



NTNU – Trondheim
Norwegian University of
Science and Technology

Ultra Low Power Frequency Synthesizer

Cole Nielsen

Electronic Systems Design, Specialization Project

Submission date: June 2020

Supervisor: Trond Ytterdal, IET

Co-supervisor: Carsten Wulff, IET

Norwegian University of Science and Technology

Department of Electronic Systems

Abstract.

A power and jitter figure of merit ($\text{FOM}_{\text{jitter}}$) state of art integer-N all digital phase locked loop (ADPLL) frequency synthesizer implemented 22nm FD-SOI (Global Foundaries 22FDX) technology is presented in this paper. Achieved was a power consumption of $100 \mu\text{W}$ at 2.448 GHz , a jitter FOM of -226 dB , and an active area of 0.0051 mm^2 . This was obtained through an emphasis on power reducing architectural choices for application to low duty cycle wake up receivers (WUR), utilizing low complexity, bias and reference free circuits. Included is a novel, pseudo-differential voltage controlled ring oscillator utilizing FD-SOI backgates to implement both frequency tuning and differential behavior. This oscillator achieves high oscillator tuning gain with rail-to-rail input range, whilst utilizing no current biasing. Capacitive DACs are used to provide digital control to the oscillator with minimum power draw. A low complexity band-bang phase detector (BBPD) and all digital proportional-integral (PI) loop filter, with divider-free operation implements the remaining portions of the PLL. Calibration of the PLL is implemented utilizing a synchronous counter-based frequency error detection scheme coupled with a coarse bank of tuning capacitors. Furthermore, a phase noise optimization theory is presented for PI loop-filter designs in a BBPD-PLL, and also for DAC resolution determination in such a PLL. Finally, a theoretical limit for achievable PLL $\text{FOM}_{\text{jitter}}$ in the proposed design is derived.

Preface.

Simplicity is the ultimate sophistication.

Leonardo da Vinci

I would like to thank my advisors Trond Ytterdal and Carsten Wulff for providing me the opportunities to further my knowledge and experience in the dark arts of circuit design.

I also thank my family for their continual open support of my life endeavors.

Problem description.

The intent of this project is to develop an ultra low power, integer-N ADPLL frequency synthesizer for applications to wake up receiver (WUR) radio circuits. The target technology is Global Foundries 22FDX fully-depleted silicon on insulator (FD-SOI), a 22nm process node. The implemented PLL is intended for use in duty cycled wake up receiver circuit applications, with on the order of 1% active time. Thus, the design must feature low power consumption in inactive (sleep) states, and rapid wake-up/resume. The required specifications for this PLL design are given in table 1. I am going to alter these requirements to be in terms of radio system performance, i.e. BER + modulation scheme, so no strict CNR listed here.

Parameter	Specification	Unit
Power	≤ 100	μW
CNR ¹	≥ 20	20 dBc
Reference frequency ²	32	MHz
Synthesized frequency	2.448	GHz
Area	≤ 0.01	mm^2
Lock time (cold-start)	≤ 20	μs
Re-lock time (sleep-resume)	≤ 2	μs

Table 1: Design required specifications.

This work is in part a continuation of the author's previous work [1] on the optimization and simulation of integer-N ADPLLs, which focused on automation of loop filter design. The architectural proceeded with in this work are motivated through findings of this work, particularly the usage of bang-bang phase detector with proportional-integral (PI) controller based loop filter. This architecture was found to be advantageous in terms of complexity and optimizability, providing for a known good starting point on this project.

¹Carrier to noise ratio.

²Divided frequencies are also acceptable.

Contents

1	Introduction	14
1.1	Main Contributions	14
2	Theory	16
2.1	Fully Depleted Silicon on Insulator (FD-SOI)	16
2.2	MOSFET Models	16
2.2.1	I-V relations	16
2.2.2	Body Effect	18
2.2.3	Linearization of MOSFET models	19
2.3	Basic PLL	20
2.4	PLL Synthesizer Architecture	21
2.4.1	Phase Detector	22
2.4.2	Bang-bang phase detector	22
2.4.3	BBPD Noise	23
2.4.4	Divider	23
2.4.5	Loop Filter	24
2.4.6	Loop Filter Discretization and Digitization	24
2.4.7	Voltage/Digitally Controlled Oscillator	25
2.4.8	Closed Loop PLL Transfer Function	26
2.5	Phase noise	26
2.5.1	Relation to Power spectral density	27
2.5.2	Leeson's model	28
2.5.3	Phase Noise Figures of Merit	29
2.5.4	Ring Oscillator Phase Noise	30
2.6	PLL Phase Noise	30
2.6.1	PLL Noise Transfer Functions	31
2.6.2	PLL Output-referred Noise	31
3	Redefining Requirements	33
4	Design	34
4.1	Proposed Architecture - ADPLL	34
4.1.1	Block diagram	34
4.1.2	Power Saving Approach	34
4.1.3	PLL Sleep Capability	35
4.1.4	Gear switching	36
4.1.5	Power budget	36
4.1.6	Floorplan	36

4.1.7	Dividerless PLL	37
4.2	Bang-Bang Phase Detector	38
4.2.1	Circuit	40
4.3	Voltage Controlled Ring oscillator	41
4.3.1	22FDX considerations	41
4.3.2	Channel length consideration	43
4.3.3	Ring oscillator frequency derivation	44
4.3.4	Finding $\langle g_{ch} \rangle$ and C	46
4.3.5	Handling unequal NMOS/PMOS	47
4.3.6	Solving for oscillator frequency and power	47
4.3.7	Ring oscillator backgate tuning derivation	48
4.3.8	DCO Gain Uncertainty	49
4.3.9	Backgate-controlled Ring Oscillator Sensitivity Analysis	50
4.3.10	Capacitor-based coarse tuning scheme	51
4.3.11	Pseudodifferential Backgate-Coupled Inverter Delay Cell	52
4.3.12	Optimal Selection of Backgate-Couple Pseudodifferential Inverter Devices	54
4.3.13	Tunable Frequency Backgate-Coupled Pseudodifferential Delay Cell	55
4.3.14	Final Delay Circuit	58
4.3.15	Number of Ring Oscillator Stages	58
4.3.16	Final Ring Oscillator Implementation	59
4.3.17	Layout	61
4.4	Loop Filter	64
4.4.1	Proportional-integral Loop Filter	64
4.4.2	Discretization of Loop Filter	64
4.4.3	Optimal Filter Selection (Noisy BBPD)	65
4.4.4	Emergent Bang-Bang PLL Phase Noise	70
4.4.5	Choice of Optimization Strategy	73
4.4.6	Filter Design for Synchronous counter	73
4.4.7	PI-controller phase margin	75
4.4.8	Loop Filter Implementation	75
4.5	CDAC - Fine Range	76
4.5.1	Circuit	77
4.6	CDAC - Medium Range	78
4.6.1	Circuit	78
4.7	Output buffer	79
4.7.1	Circuit	80
4.8	Synchronous Counter Phase Detector	81
4.8.1	Implementation	82

CONTENTS

4.9	Control and Calibration Logic	84
4.10	Level Shifter	85
4.10.1	Circuit	85
4.10.2	Behavioral Verification of PLL Design	86
5	Results	89
5.1	Power breakdown	89
5.2	Area Breakdown	89
5.3	Phase Noise	90
5.4	Start-up Transient	90
5.5	Voltage Controlled Oscillator	91
5.5.1	Phase Noise	91
5.5.2	Frequency	91
5.5.3	Tuning	92
5.5.4	Waveforms	93
5.6	10b CDAC	94
5.7	3b CDAC	95
5.8	Bang-bang phase detector	95
5.9	Loop filter	96
5.9.1	Optimal Paramters	96
5.9.2	Digital Implementation Parameters	96
5.10	Logic	97
6	Discussion	98
6.1	Performance Limit for Ring Oscillator BBPD PLLs with PI-controllers	98
6.2	State of art	99
6.3	Areas of improvement	102
6.3.1	LC Oscillator	102
6.3.2	Coarse calibration	103
6.3.3	Subharmonic oscillator	103
6.3.4	CDAC switching noise	104
6.3.5	Ignored Flicker Noise	104
7	Conclusion	105
A	Layout	109
A.1	Ring Oscillator	109
A.1.1	Full oscillator layout	109
A.1.2	Pseudodifferential inverter delay cell	110
A.1.3	Capaitor tuning bank	110
A.2	10b CDAC	111

A.2.1	Full CDAC Layout	111
A.2.2	64 unit capacitor sub-bank	112
A.3	CDAC unit switch	112
A.4	3b CDAC	113
A.5	Buffer	114
A.6	BBPD	115
A.7	SPNR Logic	116
B	Estimating PSD with Autoregressive Model	117

List of Figures

1	22FDX cross-sectional construction of active devices [6].	16
2	MOSFET symbols.	17
3	Drain current versus gate-source bias.	17
4	Transconductances as slope localized at operating point of I-V curve.	19
5	Linearized (small-signal) MOSFET model.	20
6	Phase locked loop as elementary feedback system.	20
7	High-level PLL Synthesizer Architecture.	21
8	(a) BBPD schematic, (b) BBPD timing.	22
9	Linearized bang-bang phase detector.	22
10	Digital divider signals.	23
11	Direct form I implementation of IIR filter.	25
12	Effect of phase noise on frequency tone.	27
13	Phase noise regions of Leeson's model.	29
14	FOM_{jitter} of various LC and ring oscillators [20].	30
15	Full PLL additive noise model.	31
16	ADPLL Architecture.	34
17	PLL sleep and resume operation.	35
18	PLL floorplan.	36
19	BBPD-PLL full noise model.	37
20	Bang-bang phase detector with D flip-flop.	38
21	BBPD output expectation and jitter PDF versus input time differential.	39
22	(a) Noisy BBPD nonlinear model (b) Noisy BBPD linearized model	39
23	True single-phase clock (TSPC) D flip-flop, positive edge triggered.	40
24	(a) 22 FDX threshold voltage versus body bias, (b) Rate of change of threshold voltage versus body bias.	42
25	(a) 22 FDX extracted threshold voltage versus channel length, (b) Extracted body effect coefficient.	42
26	22FDX ring oscillator channel length sweep versus (a) FOM, (b) Oscillation frequency.	44
27	22FDX ring oscillator channel length sweep versus (a) Power, (b) Phase noise at 1 MHz carrier offset (SSB).	44
28	Model for ring oscillator.	45
29	Approximate model for ring oscillator inverter delay cell.	45
30	Backgate-tuned ring oscillator with coarse tuning capacitor bank.	51
31	FD-SOI backgate-coupled inverter topology,	52
32	(a) Common backgate inverter, (b) Linearized circuit, (c) Simplified linearized model.	53

33	(a) Pseudodifferential backgate-coupled inverter circuit, (b) Linearized circuit.	53
34	Circuit to extract self-biased common mode level.	55
35	(a) Optimal width PFET/LVTNFET, (b) Optimal width PFET/SLVTNFET.	55
36	Backgate tunable backgate-coupled pseudodifferential delay cell in (a) Parallel, (b) Telescopic implementations.	56
37	Complementary tuning of backgate voltages to achieve frequency tuning.	56
38	Pseudo-differential backgate-coupled inverter delay cell with fine and medium backgate-based tuning.	59
39	Basic differential ring oscillator circuit.	60
40	Third subharmonic to quadrature full rate conversion.	60
41	Ring oscillator delay cell full circuit.	61
42	(a) Ring oscillator delay cell symbol, (b) DCO Reset scheme.	61
43	Ring oscillator full schematic.	62
44	Delay cell slice layout (in microns).	63
45	Delay cell arrangement in layout to result in similar wirelengths between stages.	63
46	Implementation of filter.	65
47	PI-controller PLL pole-zero locations.	66
48	Phase noise power (normalized) versus α .	68
49	Simplified model of BBPD-PLL	70
50	(a) Worst case cyclostationary behavior of BBPD-PLL, (b) Resulting in spurs from worst case cyclostationary behavior.	70
51	(a) Simulated emergent bang bang phase noise component of PLL phase noise, (b) Total output phase noise (normalized) versus α .	72
52	PI-controller PLL phase margin versus damping ratio.	75
53	PI-controller implementation for combination of BBPD and synchronous counter usage.	76
54	10b CDAC.	78
55	3b CDAC.	79
56	Voltage to phase noise conversion.	80
57	Backgate-coupled pseudodifferential buffer.	81
58	Standard synchronous counter circuit.	82
59	Count to phase error decoder with handling of counter wrapping.	82
60	ASM chart for PLL state machine.	85
61	Basic low to high domain level shifter.	86
62	Simulation with 0.5% initial frequency error: (a) Loop filter transient response, (b) PLL output instantaneous frequency.	87
63	Simulation with 12 MHz (0.5%) initial frequency error: (a) BBPD/TDC detector responses, (b) PLL output phase noise power spectrum.	87

LIST OF FIGURES

64	Monte-Carlo simulation with 1000 samples, 20% RMS deviation in KDCO, and 60 MHz (2.5%) RMS deviation in initial frequency error (a) Frequency transient responses, (b) Lock time histogram.	88
65	PLL Power breakdown.	89
66	PLL phase noise SSB spectral density.	90
67	PLL start up transient.	90
68	Ring oscillator phase noise (SSB).	91
69	Variation of oscillator frequency from Monte-Carlo variation/mismatch simulation.	91
70	Supply voltage versus (\pm 10% from 0.8V) (a) Oscillation Frequency, (b) VCO gain.	92
71	Medium tuning range versus (a) Oscillation Frequency, (b) VCO gain.	92
72	Fine tuning range versus (a) Oscillation Frequency, (b) VCO gain.	93
73	Variation of VCO fine tuning gain from Monte-Carlo variation/mismatch simulation.	93
74	(a) Oscillator single-ended waveforms, (b) Oscillator common mode voltage waveform.	93
75	10b CDAC single-ended (a) Integral Nonlinearity, (b) Differential Nonlinearity.	94
76	10b CDAC differential (a) Integral Nonlinearity, (b) Differential Nonlinearity.	94
77	3b CDAC differential (a) Integral Nonlinearity, (b) Differential Nonlinearity.	95
78	BBPD extracted jitter (a) Cumulative Distribution Function, (b) Probability Distribution Function.	95
79	(a) FOM _{jitter} versus power from [35] (JSSC 2019), (b) FOM _{jitter} versus area from [26] (SSCL 2020). Note, "This work" refers to that described in the source papers.	101
80	Noise transients in DAC output during switching.	104
81	Full six stage oscillator layout with capacitor tuning bank, reset switches, and output buffer.	109
82	Unit delay stage pseudodifferential inverter.	110
83	Capaitor tuning bank.	110
84	10 bit CDAC layout.	111
85	64 unit capacitor bank.	112
86	CDAC switch.	112
87	3 bit CDAC layout.	113
88	Pseudodifferential inverter buffer cell.	114
89	Single ended bang-bang phase detector.	115
90	Pseudodifferential input bang-bang phase detector.	115
91	Place and route generated logic for PLL.	116

List of Tables

1	Design required specifications.	3
2	Power budget for design process.	36
3	Schematic simulation of TSPC DFF.	40
4	22FDX core NFET threshold voltage and body effect coefficient extraction.	43
5	22FDX core PFET threshold voltage and body effect coefficient extraction.	43
6	Delay Stage Device Sizes.	62
7	PLL parameters extracted from variance and parameter sweep simulations.	88
8	Power breakdown.	89
9	Area breakdown.	89
10	Ring oscillator performance parameters.	91
11	PLL parameters determined from filter design and optimization process for fast lock speed with TDC feedback.	92
12	PLL parameters determined from filter design and optimization process for fast lock speed with synchronous counter feedback.	96
13	PLL parameters determined from filter design and optimization process for minimum phase noise with BBPD.	96
14	Loop filter digitized coefficients.	97
15	Synthesisized logic counts.	97
16	PLL parameters determined from filter design and optimization process for minimum phase noise with BBPD.	102

Abbreviations.

ADPLL	All digital phase locked loop
BBPD	Bang-bang phase detector
BOX	Burried-oxide
BW	Bandwidth
CDAC	Capacitive digital to analog converter
CDF	Cumulative distribution function
CI	Confidence interval
CLK	Clock
CM	Common mode
CMOS	Complementary metal oxide semiconductor
CMRR	Common mode rejection ratio
CNR	Carrier to noise ratio
DAC	Digital to analog converter
DC	Direct current
DCO	Digitally controlled oscillator
DFF	D flip flop
DIV	Divider
DNL	Differential non-linearity
FDSOI	Fully depleted silicon on insulator
FET	Field effect transistor
FOM	Figure of merit
FSK	Frequency shift keying
FSM	Finite state machine
HVTPFET	High threshold voltage PFET
IIR	Infinite impulse response
INL	Integral nonlinearity
ISF	Impulse sensitivity function
KDCO	DCO Gain
LC	Inductor-capacitor
LF	Loop filter
LO	Local oscillator
LSB	Least significant bit
LVTNFET	Low voltage threshold NFET
MMSE	Minimum mean squared error
MOSFET	Metal oxide semiconductor field effect transistor

MSE	Mean squared error
NFET	N-channel field effect transistor
NMOS	N-channel metal oxide semiconductor
OOK	On-off keying
OTW	Oscillator tuning word
PD	Phase detector
PDF	Probability distribution function
PFET	P-channel FET
PI	Proportional-integral
PID	Proportional-integral-derivative
PLL	Phase locked loop
PMOS	P-channel metal oxide semiconductor
PN	Phase noise
PSD	Power spectral density
PSK	Phase shift keying
PVT	Process
RC	Resistor-capacitor
RMS	Root mean squared
RO	Ring oscillator
RST	Reset
RVT	Regular voltage threshold
SLVTNFET	Super-low voltage threshold NFET
SNR	Signal to noise ratio
SOI	Silicon on insulator
SSB	Single side band
TDC	Time to digital converter
TF	Transfer function
TSPC	True single phase circuit
UTBB	Ultra-thin body BOX
VCO	Voltage controlled oscillator
WUC	Wake up call
WUR	Wake up receiver

1 Introduction

Phase locked loops (PLLs) are the fundamental building block to virtually all wired and wireless communication systems of today. To meet industrial demands of continual and uncompromising improvement of communication system performance, i.e. higher data rates, lower power, it is paramount that PLL performance is continually improved. The advent of battery powered mobile and IoT produces an acute need for power reduction. A recent approach to reducing power consumption of mobile and IoT devices is through usage of wake up receivers (WUR). These are ultra low power, low data rate radio receivers, which listen for requests (i.e. a "wake up call", or WUC) for activity of the aforementioned devices. Upon a WUC, the device powers on and activates a higher powered radio supporting higher data rates for only the time required. In devices which are inactive for large periods of time, waiting for requests for activity (e.g. as sensor networks or wireless headphones), such a scheme can enable great power reduction, achieving 4.5 nW in [2] and 365 nW in [3] for 2.4 GHz reception, compared to utilizing a full data rate receiver to poll the radio spectrum for activity requests, which for a state of art Bluetooth design may draw on the order of 1.9 mW [4].

Thus, in this work, low power PLL design which enables WUR design is to be considered. Ultra low power has been achieved with PLL-less OOK receivers, for example achieving 4.5 nW with 0.3 kbps of data at 2.4GHz [2]. However, this work will be catered to PLL-based designs that maintain backwards-compatibility with FSK and PSK modulation schemes supported by existing standards such as 802.15.4, WiFi and Bluetooth. The PLL design approached in this work will seek methods to reduce overall complexity (minimize current paths), whilst yielding high performance on a given power budget. A brief outline of the paper is as follows. An introduction to PLL and FD-SOI theory is in section 2. The undertaken PLL Design are discussed in section 4. Simulation results obtained of the design are in section 5. Comparisons to states of art and general discussion regarding this work is in section 6. Finally, section 7 concludes.

1.1 Main Contributions

- ① Implementation of an $100 \mu\text{W}$ ultra-low power, 0.0051 mm^2 area CMOS PLL in 22FDX FD-SOI technology, with state of art $\text{FOM}_{\text{jitter}}$ within its power regime, and comparable area to state of art.
- ② Presentation of a novel pseudodifferential ring oscillator circuit topology and theory of operation, utilizing FD-SOI backgates to implement both frequency tuning and differential coupling.
- ③ Realization of linear gain voltage controlled oscillator with rail to rail range.
- ④ Loop filter optimization theory for proportional-integral controller bang-bang phase detector

PLL with a noisy detector.

- (5) Theoretical figure for FOM_{jitter} performance limit of proportional-integral controller bang-bang phase detector PLL.
- (6) DAC resolution and oscillator frequency gain optimization theory.
- (7) A novel pseudodifferential buffer presenting common mode rejection characteristics.
- (8) Implementation of low power CDACs, bang-bang phase detector.
- (9) Implementation of low power digital loop filter.
- (10) Demonstration of bias current and reference free PLL design.

2 Theory

2.1 Fully Depleted Silicon on Insulator (FD-SOI)

FD-SOI is a process technology that implements complementary metal oxide semiconductor (CMOS) transistors with an insulating layer of oxide, referred to as a buried oxide (BOX), between the channel of the transistors and the silicon substrate [5]. The addition of such an oxide reduces capacitances of the fabricated transistors to the silicon substrate, resulting in lower overall capacitance than in bulk CMOS technologies. Thus higher frequency of operating is possible versus similar sized bulk process nodes. A further feature introduced by FD-SOI technology is the ability to form isolated wells beneath fabricated devices [6], which remain electrically isolated from the transistors via the BOX and from the substrate due to PN junctions inherent in well formation. This opens the possibility to achieve biasing across a wide voltage range of the regions below individual transistors (both for PMOS and NMOS devices), which enables tuning of individual transistor threshold voltages by exploitation of the MOS body effect. The well beneath a FD-SOI transistor is referred to as the "backgate". The implementation these features in the Global Foundries 22FDX process is shown in figure 1.

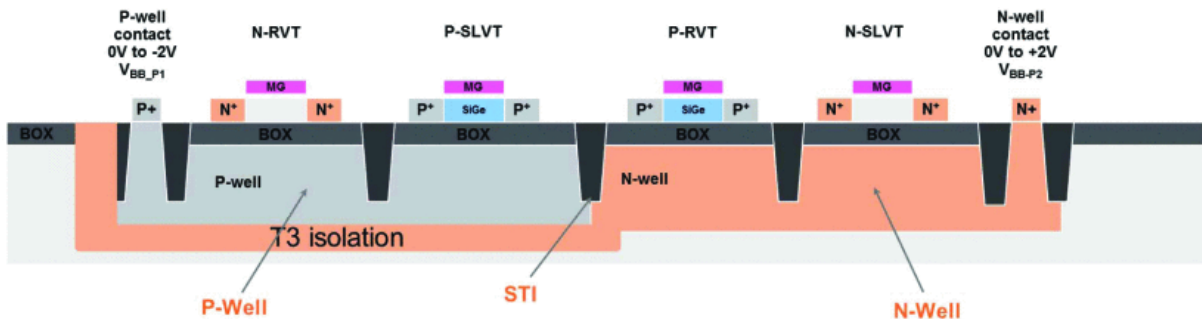


Figure 1: 22FDX cross-sectional construction of active devices [6].

2.2 MOSFET Models

2.2.1 I-V relations

Basic models that describe the large signal current-voltage relations of a Metal Oxide Semiconductor Field Effect Transistor (MOSFET) are introduced here, based wholly from [7]. For the purposes of this work, a MOSFET is schematically represented in the manner of figure 2, with gate (G), drain (D), source (S) and backgate (B) terminals. Several operating regimes occur depending on the relation of the terminal voltages. Relevant to the scope of this work, are the linear, saturated and velocity saturated regions of MOSFET operation. Nominally, it is expected that when configured as in figure 3, sweeping the gate-source voltage (V_{GS}), with the

drain-source voltage (V_{DS}) set greater than 0 in the case of a NFET, that an increasing amount of current will enter the MOSFET drain after crossing a threshold voltage (V_{TH}). V_{TH} is predominantly dependent of physical configuration of a FET (dimensions, doping, material), however is impacted by the backgate bias in what is termed "the body effect". A more detailed description of each operating regime will be given in the following discourse.

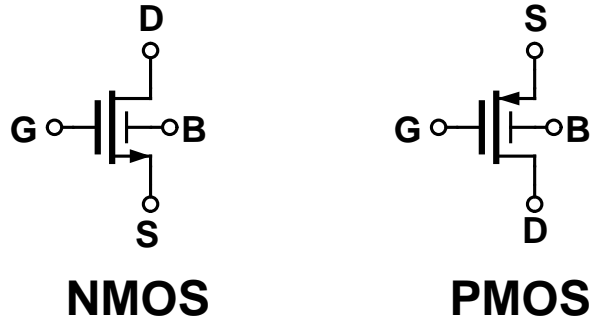


Figure 2: MOSFET symbols.

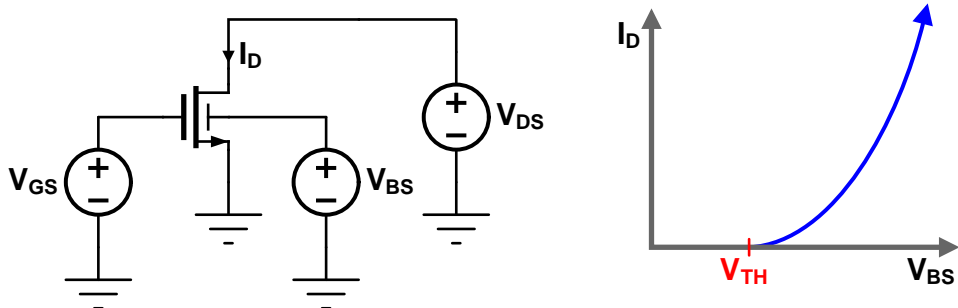


Figure 3: Drain current versus gate-source bias.

Linear Region Linear MOSFET operation occurs under the circumstances where $|V_{GS} - V_{TH}| > |V_{DS}|$. The following equation is the I-V relation in this regime, where μ_n represents the electron mobility of the semiconductor in use (within the FET channel), C_{ox} represents the MOS oxide capacitance.

$$I_D = \mu_n C_{ox} \left(\frac{W}{L} \right) \left[(V_{GS} - V_{TH}) V_{DS} - \frac{1}{2} V_{DS}^2 \right] \quad (1)$$

Saturation Region Saturation region occurs when $|V_{DS}| > |V_{GS} - V_{TH}|$. Notably, dependence of drain current on V_{DS} is reduced, and in the case of the ideal models considered here, the effect of V_{DS} are completely negated.

$$I_D = \frac{1}{2} \mu_n C_{ox} \left(\frac{W}{L} \right) (V_{GS} - V_{TH})^2 \quad (2)$$

Velocity-saturation Region In the scenario of high applied fields which arise in a short MOSFET channels, carrier velocity can saturate to a limited velocity, v_{sat} . The point at which this effect takes place is device dependent. For approximate consideration it can be understood to

2. THEORY

occur when $|V_{DS}/L > E_{crit}|$, where E_{crit} is the electric field which the carrier velocity-electric field relation ($v = \mu E$) of the channel semiconductor becomes sub-linear. Below is the MOSFET model under such circumstances.

$$I_D = WC_{ox}(V_{GS} - V_{TH})v_{sat} \quad (3)$$

2.2.2 Body Effect

Application of a bias to the substrate below a bulk MOSFET, or to the well below a FD-SOI MOSFET, has a direct effect on the threshold voltage of a MOSFET. For a bulk MOSFET, change of body bias affects the width of source-drain and source-body depletions, which consequently can increase or decrease the magnitude of the channel depletion charge as seen by the gate terminal needed to achieve channel inversion. This corresponds to a differential in the threshold voltage. The below equation [7] quantifies this effect for bulk devices. γ is the body effect coefficient, $2\Phi_F$ represents the MOS surface potential. V_{TH} is non-linearly related to the source-body voltage V_{SB} .

$$V_{TH} = V_{TH0} + \gamma \left(\sqrt{2\Phi_F + V_{SB}} - \sqrt{|2\Phi_F|} \right) \quad (4)$$

In the case of FD-SOI transistors, the nature of the body effect is modified due to the presence of the BOX. Thus, an approximate derivation for body effect will be provided here. In FD-SOI, the active channel region is thin, and under strong inversion, the entire channel region is depleted of charge. Supposing a channel height Z and channel doping N_A , the total charge to deplete the channel for inversion to occur is $Q_d = N_A Z$. With oxide capacitance $C_{ox,fg}$ associated with the front gate, the portion of the threshold voltage associated with total depletion of the channel is, from the front gate perspective:

$$V_{d,fg} = \frac{Q_d}{C_{ox,fg}} = \frac{N_A Z}{C_{ox,fg}} \quad (5)$$

Supposing that the back gate has capacitance of $C_{ox,bg}$, with bias applied V_{BS} , the back gate can be seen to "rob" the front gate of $Q_{bg} = C_{ox,bg}V_{BS}$ when in inversion. Thus results in a partial change of the front gate referred voltage required to obtain channel depletion:

$$V'_{d,fg} = \frac{Q_d - Q_{bg}}{C_{ox,fg}} = \frac{Q_d}{C_{ox,fg}} - \frac{C_{ox,bg}}{C_{ox,fg}}V_{BS} = V_{d,fg} - \Delta V_{th,bg} \quad (6)$$

It is noted that this can be written as the nominal value of $V_{d,fg}$ minus a differential. This differential is the resulting change in threshold voltage due to back gate bias, $\Delta V_{th,bg}$:

$$\Delta V_{th,bg} = \frac{C_{ox,bg}}{C_{ox,fg}}V_{BS} \quad (7)$$

This is linear with applied back gate bias, and that the strength of the coupling is tunable by the ratio of front gate and back gate capacitances. Typically this ratio is $\ll 1$. If we define the body effect coefficient γ as:

$$\gamma = \frac{C_{ox,bg}}{C_{ox,fg}} \quad (8)$$

Given a nominal threshold voltage of V_{TH0} , in FD-SOI, the threshold voltage can be represented as:

$$V_{TH} = V_{TH0} - \gamma V_{BS} \quad (9)$$

2.2.3 Linearization of MOSFET models

Under conditions where a MOSFET is held at near constant bias levels, with only minor variations around the DC operating level, simpler linearized models of the transistors can be developed. For the different operating regions of the MOSFET, the I-V relations can be generalized in terms of the function $I_D(V_{GS}, V_{DS}, V_{BS})$. Linearization is then obtained by calculating the slope of I_D with respect to the potentials V_{GS}, V_{DS}, V_{BS} . The resulting parameters (given as equations 10 to 12) are the transconductance g_m , relating gate drive to drain current, transconductance g_{mb} , relating body drive to drain current, and resistance r_o , relating drain voltage to drain current. Due to linearization, the current contributions are superimposed to determine total drain current. The linearized circuit which replaces the four terminal MOSFET symbols of figure 2 is given by the linearized circuit of figure 5.

$$g_m = \frac{\partial}{\partial V_{GS}} I_D(V_{GS}, V_{DS}, V_{BS}) \quad (10)$$

$$g_{mb} = \frac{\partial}{\partial V_{BS}} I_D(V_{GS}, V_{DS}, V_{BS}) \quad (11)$$

$$r_o = \left(\frac{\partial}{\partial V_{DS}} I_D(V_{GS}, V_{DS}, V_{BS}) \right)^{-1} \quad (12)$$

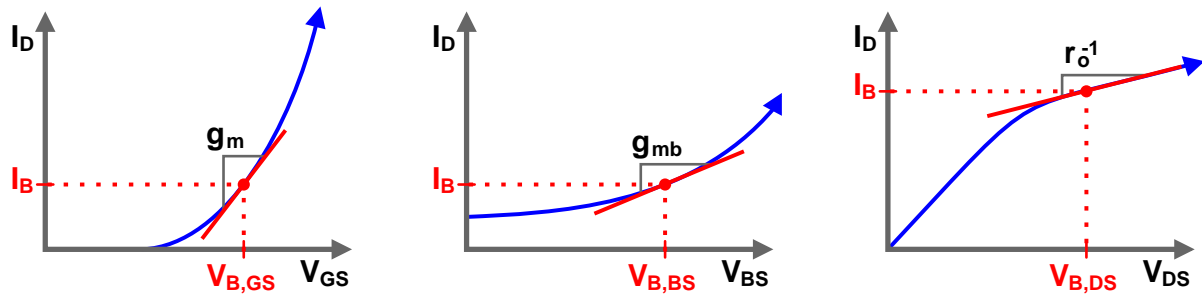


Figure 4: Transconductances as slope localized at operating point of I-V curve.

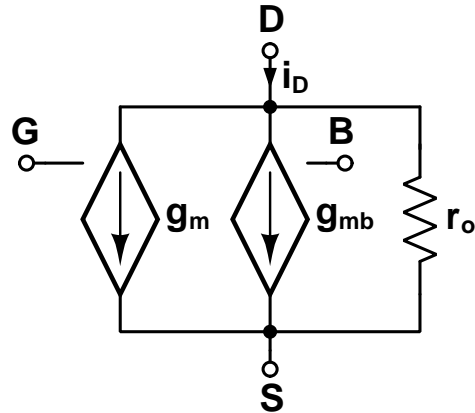


Figure 5: Linearized (small-signal) MOSFET model.

A useful relation based on this linearization can be determined, based on the FD-SOI body effect equation 9, and the I-V relations for the three MOSFET operation regions discussed in section 2.2.1. Computation of g_m and g_{mb} for all three regions with the FD-SOI body effect yields the same result given in equation 13. This is that g_{mb} and g_m are related by the body effect coefficient γ .

$$g_{mb} = \gamma g_m \quad (13)$$

2.3 Basic PLL

A phase locked loop (PLL) is a feedback system whose output tracks or maintains a fixed phase relationship to an input signal. PLLs are well suited for frequency synthesis, which is the process of generating derivative frequencies from some reference frequency. Given a reference signal with phase trajectory Φ_{ref} and output signal with phase Φ_{out} , a PLL can be modeled as in figure 6 using an elementary feedback system, with feedforward and feedback networks $A(s)$ and $B(s)$.

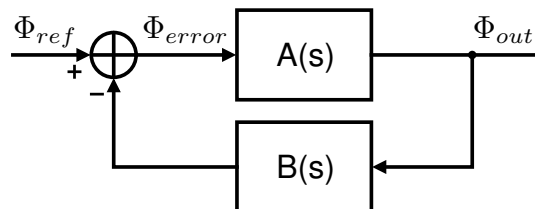


Figure 6: Phase locked loop as elementary feedback system.

The closed loop phase response for Φ_{ref} to Φ_{out} is therefore:

$$\frac{\Phi_{out}(s)}{\Phi_{ref}(s)} = \frac{A(s)}{1 + A(s)B(s)} \quad (14)$$

A case of interest is when $B(s) = 1/N$, where N is a constant, and the loop gain $L(s) = A(s)B(s) \gg 1$. The closed loop response for this case is:

$$\frac{\Phi_{out}(s)}{\Phi_{ref}(s)} \approx \frac{A(s)}{A(s)B(s)} = \frac{1}{B(s)} = N \quad (15)$$

We see that the phase through the PLL is multiplied by a factor of N . If the input phase signal is sinusoidal with frequency ω_{ref} , and likewise the output with ω_{out} , then $\phi_{ref}(t) = \omega_{ref}t$ and $\phi_{out}(t) = \omega_{out}t$. Accordingly:

$$\frac{\Phi_{out}(t)}{\Phi_{ref}(t)} = \frac{\omega_{out}t}{\omega_{ref}t} \approx N \rightarrow \omega_{out} \approx N\omega_{ref} \quad (16)$$

Therefore, it is observed that a PLL allows for the generation of a new frequency from a reference frequency signal, which is termed as "frequency synthesis". With a feedback division ratio of $1/N$, the PLL multiplies the reference frequency by a factor of N . Hereon, the $B(s)$ portion of a PLL feedback network is referred to as a divider, with associated division ratio N .

2.4 PLL Synthesizer Architecture

A typical architecture for implementing a physically realizable PLL frequency synthesizer [8] is shown in figure 7. This PLL is comprised of four components: (1) a phase detector, herein PD, (2) a loop filter, herein $H_{LF}(s)$, (3) a voltage controlled oscillator, herein VCO, and (4) a divider, indicated as " $\div N$ " in figure 7. In control systems parlance, the loop filter corresponds to a controller, the VCO an actuator, and the divider as feedback.

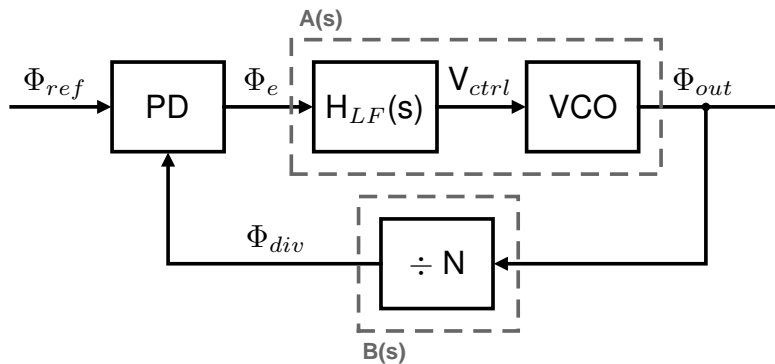


Figure 7: High-level PLL Synthesizer Architecture.

Further explanation of these components will be hereafter made.

2.4.1 Phase Detector

A phase detector acts as the summation point of figure 6, which measures the phase error Φ_e between the reference signal and the output of the PLL. The phase error is then used by the controller, which is implemented as the loop filter, to adjust the PLL's state. Such a phase detector may also have intrinsic gain, given by K_{PD} .

$$\Phi_e(s) = K_{PD}(\Phi_{ref}(s) - \Phi_{div}(s)) \quad (17)$$

2.4.2 Bang-bang phase detector

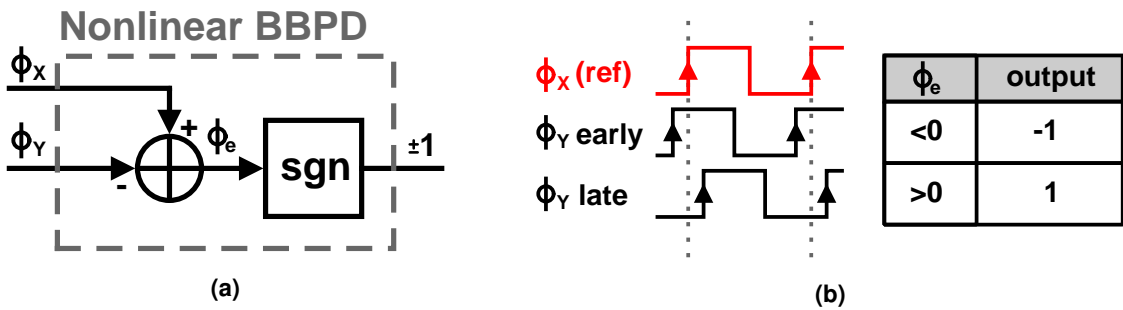


Figure 8: (a) BBPD schematic, (b) BBPD timing.

A simple implementation of a phase detector is a bang-bang phase detector (BBPD) [9]. As exhibited in figure 8, a BBPD outputs a value of 1 if the input Φ_Y is late relative to the reference Φ_X (representing a clock signal), and -1 if it is early. A BBPD shows abrupt nonlinearity in its transfer characteristics. If the error signal variance $\sigma_{\Phi_e}^2$ is constant, which is expected in steady-state PLL operation, a linearized model for phase detector gain can be established [10], given in equation 18.

A linearized version of the BBPD is illustrated in figure 9. The output z valued as ± 1 (its variance $\sigma_y^2=1$).

$$K_{BBPD} = \frac{\mathbb{E}[\Phi_e(t) \cdot z(t)]}{\mathbb{E}[\Phi_e^2(t)]} = \sqrt{\frac{2}{\pi}} \frac{1}{\sigma_{\Phi_e}} \quad (18)$$

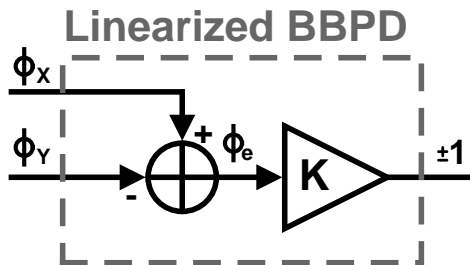


Figure 9: Linearized bang-bang phase detector.

2.4.3 BBPD Noise

Given the output of the BBPD is of fixed power $\sigma_z^2 = 1$, a linearized gain of K_{BBPD} , a phase error power of $\text{Var}[\Phi_e(t)] = \sigma_{\Phi_e}^2$, and $\mathbb{E}[\Phi_e(t)] = 0$, the noise power $\sigma_{n_{BBPD}}^2$ out of the BBPD is in equation 19. $K_{BBPD}^2 \sigma_{\Phi_e}^2$ represents the power of the phase error signal component post-detector, and it is assumed that noise power and signal power are uncorrelated.

$$\sigma_{n_{BBPD}}^2 = \sigma_z^2 - K_{BBPD}^2 \sigma_{\Phi_e}^2 = 1 - \frac{2}{\pi} \quad (19)$$

Observe that the BBPD noise power is constant. If the reference signal is a clock signal with frequency f_{ref} , the BBPD noise spectral density is in equation 20.

$$S_{n_{BBPD}(f)} = \frac{\sigma_{n_{BBPD}}^2}{\Delta f} = \frac{(1 - \frac{2}{\pi})}{f_{ref}} \quad (20)$$

2.4.4 Divider

A divider is used as the feedback path in the PLL, where the division ratio N controls the frequency multiplication of a PLL synthesizer. The transfer function of the divider is:

$$H_{div}(s) = \frac{\Phi_{div}(s)}{\Phi_{out}(s)} = \frac{1}{N} \quad (21)$$

Dividers are commonly realized as digital modulo-N counters that count oscillation cycles [11]. With a division ratio of N, the output of the divider will have an active edge transition (considered to be rising edge as shown in figure 10) every N input cycles. Phase information is inferred from the output edge timing, which occurs with time interval N/f_{osc} , and is equal to the point at which output phase equals a multiple of 2π . Thus a digital divider does not provider continuous phase information, but rather a sampled phase signal with rate f_{osc}/N .

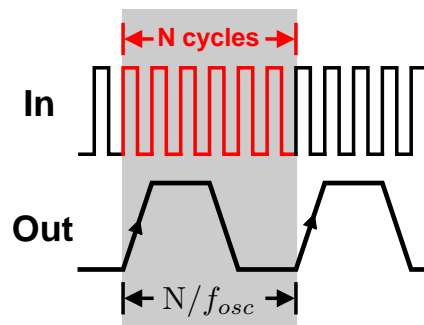


Figure 10: Digital divider signals.

2.4.5 Loop Filter

A loop filter behaves as the controller of a PLL, namely controlling the phase-frequency response of PLL. The choice of loop filter transfer function significantly affects transient PLL behavior, as well as phase noise performance, as is later described. Here, a pole-zero based controller is defined for use in this work. This is designed to have P poles and Z zeros, and can be represented in the canonical form of equation 22 as a rational function of polynomials of s with coefficients given with $\{a_0, \dots, a_P\}$ and $\{b_0, \dots, b_Z\}$.

$$H_{LF}(s) = \frac{\sum_{j=0}^Z b_j s^j}{\sum_{k=0}^P a_k s^k} \quad (22)$$

2.4.6 Loop Filter Discretization and Digitization

In PLLs which sample on a fixed interval defined by a reference clock frequency f_{ref} , derivation of a discrete time controller model is necessary. This is derived from the general form continuous loop filter (equation 22) via application of a continuous s-domain to discrete z-domain transformation. Strictly speaking, $z^{-1} = e^{-s\Delta T_s}$ for values on the unit circle, i.e. $r=1$ [12]. If the PLL sampling rate $f_s=f_{ref}$ is constrained to be sufficiently higher than the implemented filter bandwidth (i.e. PLL loop bandwidth, BW_{loop}), a simpler transformation using a truncated Taylor series approximation is applicable. Given the $1/\Delta T_s=f_s$ as the relation for sampling rate, then:

$$\begin{aligned} z^{-1} &= e^{-s\Delta T_s} && \text{(definition of z on unit circle)} \\ &= \sum_{k=0}^{\infty} \frac{(-s\Delta T_s)^k}{k!} && \text{(exponential Taylor series)} \\ &\approx 1 - s\Delta T_s && \text{(if } |s\Delta T_s| = 2\pi BW_{loop} \cdot \Delta T_s \ll 1) \end{aligned}$$

Thus the s-to-z and z-to-s identities for the approximate transform are:

$$z^{-1} = 1 - s\Delta T_s \quad (23)$$

$$s = \frac{1}{\Delta T_s} (1 - z^{-1}) \quad (24)$$

Applying equation 24 to the general loop filter of equation 22 yields the z-domain loop filter:

$$H_{LF}(z) = H_{LF}(s)|_{s=\frac{1}{\Delta T_s}(1-z^{-1})} = \left. \frac{\sum_{j=0}^Z b_j s^j}{\sum_{k=0}^P a_k s^k} \right|_{s=\frac{1}{\Delta T_s}(1-z^{-1})} \quad (25)$$

$$= \frac{\sum_{j=0}^Z \frac{b_j}{\Delta T_s^j} (1 - z^{-1})^j}{\sum_{k=0}^P \frac{a_k}{\Delta T_s^k} (1 - z^{-1})^k} \quad (26)$$

Equation 26 is transformed into a digitally implementable form by reorganizing into the canonical representation of equation 27, which then determines the tap coefficients for the sampled-time difference equation in equation 28.

$$H_{LF}(z) = \frac{\sum_{j=0}^P b'_j z^{-j}}{1 + \sum_{k=1}^Z a'_k z^{-k}} \quad (27)$$

$$y[n] = - \sum_{k=1}^P a'_k y[n-k] + \sum_{j=0}^Z b'_j x[n-j] \quad (28)$$

The obtained difference equation is directly implementable in digital hardware with a direct form-I IIR filter [13] shown in figure 11. Such a design is a candidate for automatic synthesis of digital logic. The filter coefficients $\{a'_1, \dots, a'_P\}$ and $\{b'_0, \dots, b'_Z\}$ must be quantized into finite resolution fixed point words for a complete digital implementation. The delay elements (z^{-1} blocks) are implementable digitally as registers, the coefficient gains are implementable with array multipliers, and the adders are implementable with digital adders.

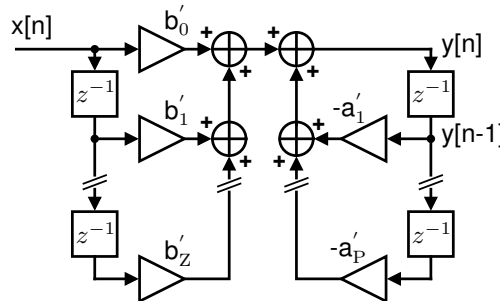


Figure 11: Direct form I implementation of IIR filter.

2.4.7 Voltage/Digitally Controlled Oscillator

A controlled oscillator is an oscillator with frequency controlled by an input signal. When this input signal takes the form of an analog voltage V_{ctrl} , it is referred to as a voltage controlled oscillator (VCO). Otherwise, when controlled digitally with an oscillator tuning word (OTW) $u[n]$, it is referred to as a digitally controlled oscillator (DCO). Nominally, a controlled oscillator is characterized by its gain, in the case of a VCO is $K_{VCO} = \partial f / \partial V_{ctrl}$. With a DCO, the gain is $K_{DCO} = \Delta f / LSB$, that is the change in frequency per least significant bit. Analyzed in terms

2. THEORY

of phase (for the VCO case), an oscillator can be seen as a time-phase integrator, provided a nominal oscillator frequency of f_0 :

$$\Phi_{VCO}(t) = \Phi_{out}(t) = \int 2\pi(K_{VCO}V_{ctrl}(t) + f_0)dt \quad (29)$$

In the s-domain, the transfer function for a VCO is in equation 30 and equation 31 for a DCO.

$$H_{VCO}(s) = \frac{\Phi_{VCO}(s)}{V_{ctrl}(s)} = \frac{2\pi K_{VCO}}{s} \quad (30)$$

$$H_{DCO}(s) = \frac{\Phi_{VCO}(s)}{u(s)} = \frac{2\pi K_{DCO}}{s} \quad (31)$$

By application of discretization and conversion to difference equations, the sampled-time oscillator phase signals are equation 32 for a VCO and equation 33 for a DCO.

$$\Phi_{out}[n] = \Phi_{out}[n - 1] + 2\pi K_{VCO} \Delta T_s V_{ctrl}[n] \quad (32)$$

$$\Phi_{out}[n] = \Phi_{out}[n - 1] + 2\pi K_{DCO} \Delta T_s u[n] \quad (33)$$

2.4.8 Closed Loop PLL Transfer Function

With a PLL described at the component level, the closed loop dynamics of the PLL can be computed. A PLL loop gain $L(s)$ can be first determined (using BBPD definition for phase detector gain).

$$L(s) = K_{PD} H_{LF}(s) H_{DCO}(s) H_{div}(s) = \frac{2\pi K_{PD} K_{DCO}}{N} \frac{1}{s} \frac{\sum_{j=0}^Z b_j s^j}{\sum_{k=0}^P a_k s^k} \quad (34)$$

Closing the loop with the phase detector as the feedback summation point, the response of the PLL from reference to output is in equation 35.

$$T(s) = \frac{\Phi_{out}(s)}{\Phi_{ref}(s)} = \frac{2\pi K_{PD} K_{DCO} \sum_{j=0}^Z b_j s^j}{\sum_{k=0}^P a_k s^{k+1} + \frac{2\pi K_{PD} K_{DCO}}{N} \sum_{j=0}^Z b_j s^j} = N \frac{L(s)}{1 + L(s)} \quad (35)$$

2.5 Phase noise

Phase noise can be described as undesired variation in an oscillator's phase trajectory from ideal. If an oscillator's frequency is ω_{osc} , then with additive phase noise, the phase of an oscillator is in 36.

$$\Phi_{osc}(t) = \omega_{osc} t + \Phi_n(t) \quad (36)$$

This is composed of a linear phase component $\omega_{osc}t$ and a noise component $\Phi_n(t)$. In the frequency domain, the effect of phase noise is that it broadens the tone of the oscillator, as

shown in figure 12. Phase noise can be viewed as instability in terms of oscillator frequency.

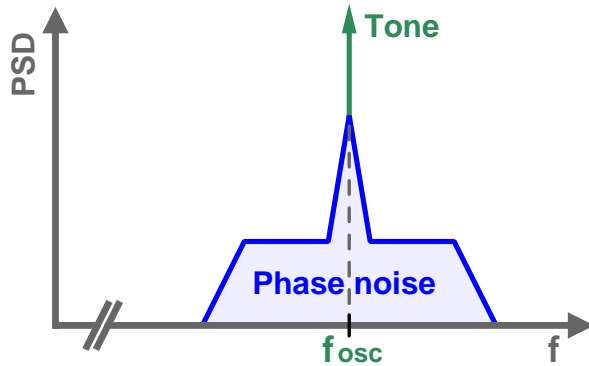


Figure 12: Effect of phase noise on frequency tone.

2.5.1 Relation to Power spectral density

An oscillator's voltage waveform can be described in terms of a phase trajectory function $\Phi_{osc}(t)$ and amplitude A_0 in the following manner (ignoring higher harmonics):

$$V_{osc}(t) = \Re \{ A_0 e^{j\Phi_{osc}(t)} \} \quad (37)$$

In an oscillator, it is desirable for phase noise to be small, and zero mean ($\mathbb{E}[\Phi_n(t)] = 0$). Using a constraint $\text{Var}[\Phi_n(t)] \ll 1$ the following approximations can be applied to determine the oscillators spectral density in terms of the phase noise component $\Phi_n(t)$.

$$V_{osc}(t) = \Re \{ A_0 e^{j\omega_{osc}t} e^{j\Phi_n(t)} \} \quad (\text{oscillator waveform}) \quad (38)$$

$$= \Re \left\{ A_0 e^{j\omega_{osc}t} \sum_{k=0}^{\infty} \frac{(j\Phi_n(t))^k}{k!} \right\} \quad (\text{apply exponential Taylor series}) \quad (39)$$

$$\approx \Re \{ A_0 e^{j\omega_{osc}t} + j\Phi_n(t) A_0 e^{j\omega_{osc}t} \} \quad (\text{truncate series at } k=1 \text{ given } \text{Var}[\Phi_n(t)] \ll 1) \quad (40)$$

$$= A_0 \cos(\omega_{osc}t) - \Phi_n(t) A_0 \sin(\omega_{osc}t) \quad (\text{taking real component}) \quad (41)$$

$$(42)$$

The result is a carrier cosine signal, and an orthogonal sine signal modulated by the phase noise Φ_n . From this, the spectral density of the phase noise relative to the carrier can be estimated. The power spectral density $S_{V_{osc}}$ is computed in equations 43-45. Due to orthogonality of the sine/cosine components of equation 41, the cross terms that appear in the PSD computation are

2. THEORY

zero.

$$S_{V_{out}}(f) = \lim_{\Delta T \rightarrow \infty} \frac{1}{\Delta T} |\mathcal{F}\{V_{out}(t) \cdot \text{rect}(t/\Delta T)\}|^2 \quad (43)$$

$$= \lim_{\Delta T \rightarrow \infty} \frac{A_0^2}{\Delta T} |\mathcal{F}\{\cos(\omega_{osc} t) \cdot \text{rect}(t/\Delta T)\}|^2 \quad (44)$$

$$+ \lim_{\Delta T \rightarrow \infty} \frac{A_0^2}{\Delta T} |\mathcal{F}\{\Phi_n(t) \cdot \text{rect}(t/\Delta T)\} * \mathcal{F}\{\sin(\omega_{osc} t) \cdot \text{rect}(t/\Delta T)\}|^2 \quad (45)$$

$$(46)$$

The noise power spectral density function of the output waveform $\mathcal{L}(\Delta f)$ is defined as the noise PSD at offset Δf from the carrier frequency f_{osc} , normalized to the carrier power. Here the PSD of the carrier component is given by equation 44, and the noise component by equation 45. Shifting equation 45 by $-\omega_{osc}$ and performing normalization for carrier power results in:

$$\mathcal{L}(\Delta f) = \lim_{\Delta T \rightarrow \infty} \frac{1}{\Delta T} |\mathcal{F}\{\Phi_n(t) \cdot \text{rect}(t/\Delta T)\}|^2 \Big|_{f=\Delta f} = S_{\Phi_n}(\Delta f) \quad (47)$$

Thus, the noise PSD $\mathcal{L}(\Delta f)$ of the PLL output waveform relative to the carrier is equal to the PSD of the phase noise signal $\Phi_n(t)$, provided $\text{Var}[\Phi_n(t)] \ll 1$. The PSD of $\Phi_n(t)$ is denoted as $S_{\Phi_n}(\Delta f)$.

2.5.2 Leeson's model

Oscillator noise from thermal and stochastic sources is typically represented mathematically using Leeson's model for oscillator phase noise [14]. Leeson's model considers noise power density at an offset Δf from the oscillator tone (carrier). Noise power density is represented with the function $\mathcal{L}(\Delta f)$, which is the noise power density normalized to the power of the oscillator carrier tone, in other words in units of dBc/Hz. Leeson's model divides phase noise into three regions, illustrated in figure 13: (1) flicker-noise dominated, with a slope of -30 dB/decade, (2) white frequency-noise dominated, with -20 dB per decade, and (3) a flat region, limited by the thermal noise floor or amplitude noise. It is noted that phase noise components are at frequencies different than the carrier, hence are orthogonal, and can be treated as independent components that are added to the main oscillator tone signal for analysis.

The equation for $\mathcal{L}(\Delta f)$ (from [15]) is in equation 48, and is dependent on temperature T, excess noise factor F, DC oscillator power P_{DC} , oscillator Q factor, and the transition frequencies f_1 and f_2 that separate the different noise regions. It is of interest to note that the phase noise relative to the carrier will increase as power decreases, which provides challenge for creating

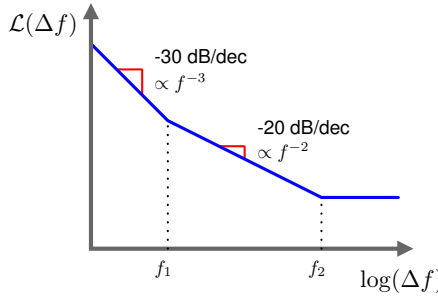


Figure 13: Phase noise regions of Leeson's model.

low power oscillators with acceptable phase noise characteristics.

$$\mathcal{L}(\Delta f) = 10 \log_{10} \left[\frac{2Fk_B T}{P_{DC}} \left(1 + \left(\frac{f_2}{2Q\Delta f} \right)^2 \right) \left(1 + \frac{f_1}{|\Delta f|} \right) \right] = S_{\Phi n_{DCO}}(\Delta f) \quad (48)$$

For notational consistency, the following redefinition is used in the remainder of this paper:
 $S_{\Phi n_{DCO}}(f) = \mathcal{L}(\Delta f)|_{\Delta f=f}$

2.5.3 Phase Noise Figures of Merit

A common method to assign a figure of merit (FOM) to oscillator phase noise performance is to utilize the below relation [16]. Such a model assumes linear tradeoffs between power, frequency, and phase noise, and assumes that the rolloff of phase noise will occur with -20 dB/decade. A Lower FOM here is better.

$$\text{FOM}_{pn} = 10 \log_{10} \left(\frac{P_{DC}}{1 \text{ mW}} \cdot \left(\frac{\Delta f}{f_0} \right)^2 \right) + \mathcal{L}(\Delta f) \quad (49)$$

Another FOM applied to PLLs is provided below, based on the RMS jitter of the PLL [17]. Here, RMS jitter is used as the phase spectrum of a PLL is often more complicated than a simple oscillator, containing spurs, in-band phase noise suppression, and peaking resulting from the PLL loop filter. It should be noted that RMS jitter (in time) is tied directly to total phase noise power, as expected by Parseval's theorem [18]. Lower is better again with this FOM.

$$\text{FOM}_{\text{jitter}} = 10 \log_{10} \left(\frac{\sigma_{t_j}^2}{(1 \text{ s})^2} \cdot \frac{P_{DC}}{1 \text{ mW}} \right) \quad (50)$$

$$\sigma_{t_j}^2 = \frac{\text{Var}[\Phi_n(t)]}{\omega_0^2} \quad (51)$$

In general, a good figure of merit is arrived to be decreasing power and/or minimizing total phase noise power.

2. THEORY

2.5.4 Ring Oscillator Phase Noise

Oscillator phase noise for ring oscillators has a well defined limit as determined by analysis of noise of ideal RC circuits [19], which is provided in equation 52. Note that this model is limited to analyzing the -20 dB/decade part of an oscillator's spectrum as seen by Leeson's model.

$$\mathcal{L}_{min}(\Delta f) = 10 \log 10 \left(\frac{7.33k_B T}{P_{DC}} \left(\frac{f_0}{\Delta f} \right)^2 \right) \quad (52)$$

Applying this to the phase noise FOM equation 49, a limit for ring oscillator phase noise FOM is determined in equation 53.

$$FOM_{pn,min} = 10 \log 10 (7330k_B T) \quad (53)$$

At 300K, it is expected that the jitter FOM for a ring oscillator should approach -165.2 dB. An example state of art comparison figure in 14 shows clustering by oscillator type of jitter FOM calculated in various published works in [20]. It is seen the FOM value calculated from theory is close to that seen implemented hardware.

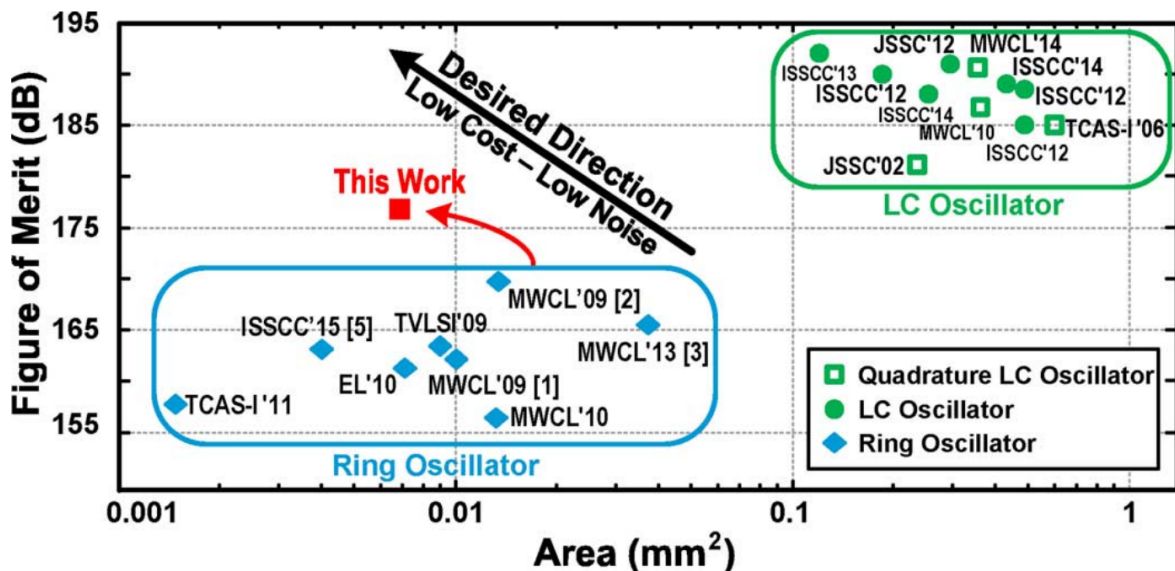


Figure 14: FOM_{jitter} of various LC and ring oscillators [20].

2.6 PLL Phase Noise

Having an understanding of PLL theory, individual PLL component characteristics, and phase noise, a model for PLL phase noise can be constructed. To begin, noise sensitivity transfer functions are defined to refer each noise source to the PLL output. Here, all noise sources have been defined as additive signal components to each PLL component output. The full system noise model is in figure 15.

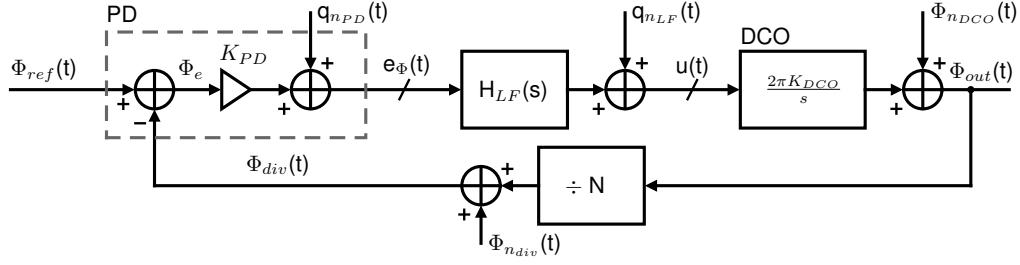


Figure 15: Full PLL additive noise model.

2.6.1 PLL Noise Transfer Functions

Following the approach of [21], a transfer function $\hat{T}(s)$ is defined in equation 54 which characterizes the normalized closed loop phase response from reference input to output of the PLL. $L(s)$ is the PLL loop gain and $T(s)$ is the PLL closed loop transfer function.

$$\hat{T}(s) = \frac{L(s)}{1 + L(s)} \quad \text{s.t.} \quad T(s) = \frac{\Phi_{out}}{\Phi_{ref}} = N\hat{T}(s) \quad (54)$$

Solving for the closed transfer functions between each noise source (q_{nBBPD} , q_{nLF} , Φ_{nDCO} and Φ_{ndiv}) to the output Φ_{out} in the s-domain yields equations 55-58.

$$\frac{\Phi_{out}(s)}{q_{nPD}(s)} = \frac{2\pi \frac{K_{DCO}}{s} H_{LF}(s)}{1 + L(s)} = \frac{N}{K_{PD}} \frac{L(s)}{1 + L(s)} = \frac{N}{K_{PD}} \hat{T}(s) \quad (55)$$

$$\frac{\Phi_{out}(s)}{\Phi_{nDCO}(s)} = \frac{1}{1 + L(s)} = 1 - \hat{T}(s) \quad (56)$$

$$\frac{\Phi_{out}(s)}{q_{nLF}(s)} = \frac{2\pi \frac{K_{DCO}}{s}}{1 + L(s)} = 2\pi \frac{K_{DCO}}{s} (1 - \hat{T}(s)) \quad (57)$$

$$\frac{\Phi_{out}(s)}{\Phi_{ndiv}(s)} = \frac{K_{BBPD} 2\pi \frac{K_{DCO}}{s} H_{LF}(s)}{1 + L(s)} = N \frac{L(s)}{1 + L(s)} = N\hat{T}(s) \quad (58)$$

2.6.2 PLL Output-referred Noise

Using the noise transfer functions, the expressions for noise power spectrum of the BBPD (equation 20) and the noise spectrum of a ring oscillator (equation 52), the PLL output phase noise spectrum of each component is determined by multiplying the magnitude squared of each noise transfer function with the respective noise spectral density. Here it is found that the BBPD noise component out of the PLL is given in equation 59, and the oscillator component is given in equation 60. The loop filter and divider components are here ignored, as they will be shown not be relevant in this work.

2. THEORY

$$S_{\Phi n_{BBPD,out}}(f) = S_{n_{BBPD}}(f) \left| \frac{\Phi_{out}(f)}{q_{n_{BBPD}}(f)} \right|^2 = \frac{(\frac{\pi}{2} - 1)}{f_{ref}} \left| \sigma_{\Phi_e} N \hat{T}(f) \right|^2 \quad (59)$$

$$S_{\Phi n_{DCO,out}}(f) = \mathcal{L}_{min}(f) \left| \frac{\Phi_{out}(f)}{q_{n_{DCO}}(f)} \right|^2 = \frac{7.33k_B T}{P} \left(\frac{f_0}{f} \right)^2 |1 - \hat{T}(f)|^2 \quad (60)$$

The total output noise power spectral density is given as the sum of the components, presuming independence of all noise sources. Following the results of section 2.5.1, which determined that oscillator power spectrum is equivalent to the phase noise power spectrum for zero mean phase noise with low power, the final oscillator power spectrum at Δf from the carrier is in equation 61.

$$S_{n_{PLL}}(f_{osc} + \Delta f) = S_{\Phi n_{BBPD,out}}(\Delta f) + S_{\Phi n_{DCO,out}}(\Delta f) \quad (61)$$

$$= \frac{(\frac{\pi}{2} - 1)}{f_{ref}} \left| \sigma_{\Phi_e} N \hat{T}(\Delta f) \right|^2 + \frac{7.33k_B T}{P} \left(\frac{f_0}{\Delta f} \right)^2 |1 - \hat{T}(\Delta f)|^2 \quad (62)$$

A complexity arises in equation 61 due to the fact that the power spectrum is a function of the root mean squared (RMS) phase error, σ_{Φ_e} . σ_{Φ_e} may be calculated as equation 63. It is seen that the spectrum and σ_{Φ_e} are cyclically defined, so a system of equations formed by the two must be solved to determine the final noise spectrum.

$$\sigma_{\Phi_e} = \sqrt{2 \int_0^\infty S_{n_{PLL}}(f_{osc} + \Delta f) d\Delta f} \quad (63)$$

3 Redefining Requirements

I've decided to have problem description state radio requirements of intended system, and then here I will derive the requirement for CNR of the PLL to meet those radio requirements from a BER vs CNR simulation. The requirements imposed on this PLL are defined in terms of a radio system for which it will be a component of. First, the modulation scheme of this system is described. Gaussian frequency shift keying with bandwidth-time (BT) product of 0.3 is utilized as the basic scheme, With a nominal bit rate of 1 Mbps. Under such circumstances, 1 and 0 are respectively encoded as ± 250 kHz of frequency deviation from the carrier. In order to improve bit error rate, while maintaining compatibility with 1 Mbps transmitters, a modified data rate of 250 ksymbols/s is used where one data symbol WIP... skip this for now.

4 Design

The primary objective in this work is to obtain a very low $100\mu\text{W}$ power consumption for a 2.448 GHz PLL frequency synthesizer, while achieving a carrier-to-noise ratio for the synthesized signal of $> \text{X}$ dB. Consequently, the design philosophy adhered to in this work is pursue simplicity wherever possible, in order to reduce number of sources of power draw and noise. Furthermore, this design is targeted to allow duty cycled operation to further reduce power. Thus, an all-digital architecture has been selected to enable the possibility to save the PLL state, enter an ultra-low-power sleep state, and then resume from the stored state rapidly, without requiring relocking of the PLL, all to enable duty-cycled operation.

4.1 Proposed Architecture - ADPLL

The undertaken PLL architecture is in figure 16. It comprises primarily of five components: (1) a counter-based phase detector for initial calibration and start up, (2) a bang-bang phase detector for steady state feedback, (3) a proportional-integral controller loop filter, (4) a DCO implemented as a VCO plus capacitive DACs, and (5) a control and calibration engine, consisting of digital logic. The rationale for this architecture will be described in the following subsections.

4.1.1 Block diagram

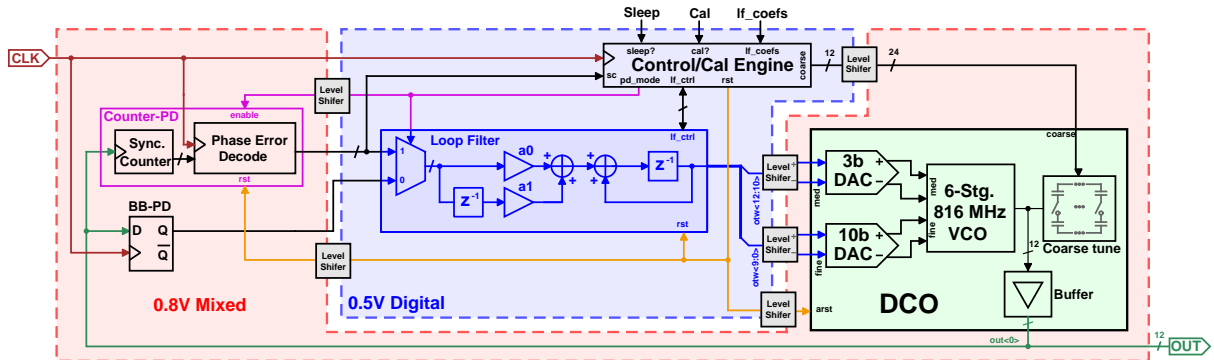


Figure 16: ADPLL Architecture.

4.1.2 Power Saving Approach

Power savings have been attempted by minimization of complexity. First, the need of a divider is removed from the design by the usage of both the counter phase detector and BBPD. For initial cold start up of the PLL from an unknown state, the counter-based phase detector functions

as a low-resolution replacement for a divider and linear phase detector. When near steady state, the counter-PD is disabled and replaced by BBPD feedback, which will maintain the PLL at steady state. The removal of a divider results in lower power consumption, and less noise added in-loop. The usage of only a BBPD in steady state further reduces power, as it is a minimum complexity phase detector. This is expected without significant performance degradation, as with proper optimization, BBPD PLLs can obtain comparable performance to linear charge-pump style PLLs [10]. Additional power improvements are obtained in the usage of digital logic to implement the loop filter, using a simple PI-controller architecture. A divided power domain approach is used here, split between (1) 0.5V for loop filter, calibration and control logic, and (2) 0.8V for the analog portions, which constitute the DCO, in addition to the phase detectors. Multiple power domains allows for reduction of the digital logic power expenditure, while allowing for sufficient voltage for proper oscillator function. The final power saving move is implemented in a DCO based on the combination of several CDACs with a voltage controlled ring oscillator. This reduces to near zero the DC current draw associated with control of the VCO. The overall design is implemented with no static current paths, other than that associated with leakage, achieved by favoring static logic derived components throughout the PLL.

4.1.3 PLL Sleep Capability

A feature gained in the proposed all-digital architecture is the ability to abruptly save the state of the PLL digitally and place all unneeded components into an ultra low power sleep mode, and then later resume the PLL from the saved state. Figure 17 demonstrates such operation, where t_{l1} is the lock time from cold start, and t_{l2} is the time to relock from a resume state. It is expected that slight drift in the oscillator characteristics will occur when resuming, so the relock time will likely be nonzero. However, the relock time is substantially lower than relocking from a cold state, as only a small degree of error must be corrected. This functionality enables the ability to rapidly duty cycle the PLL between active and sleep states. Power consumption of the PLL is reduced by a factor that is the duty cycle which it is operated; for example, 100 μ W nominal power consumption with 1% duty cycle will result in 1 μ W average draw, which is attractive for battery powered wireless devices (particularly with wake up radios).

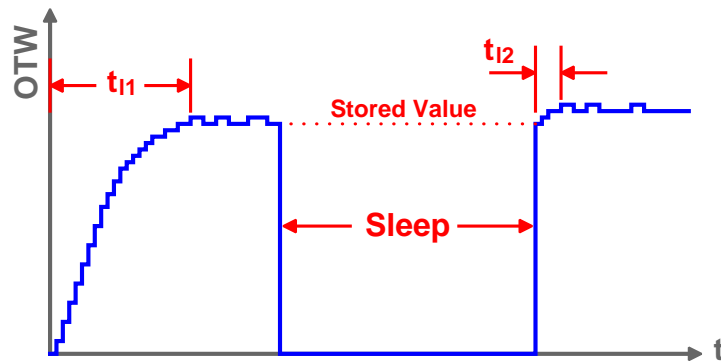


Figure 17: PLL sleep and resume operation.

4.1.4 Gear switching

The proposed digital architecture enables the ability to dynamically alter the loop filter response. This can be used to speed up lock from a cold state by using a lock time optimized filter initially, and then switch to a phase noise optimized filter after achieving initial lock. This approach is called gear switching [22], and is employed in this work by utilizing different loop filters for the start-up synchronous counter phase detector operation and the steady state BBPD operation.

4.1.5 Power budget

The below power budget was used in the design process to divide up the $100 \mu\text{W}$ allotment between the different PLL components. In order to minimize oscillator phase noise, as large of a portion was allotted to the oscillator, being 80%.

DCO	Phase detector	Digital (LF)	Other	SUM
$80 \mu\text{W}$	$10 \mu\text{W}$	$10 \mu\text{W}$	$0 \mu\text{W}$	$\leq 100 \mu\text{W}$

Table 2: Power budget for design process.

4.1.6 Floorplan

The below floor plan (dimensions in microns) has been devised to meet the area requirement of $< 0.01 \text{ mm}^2$. The dimensions are $60\mu\text{m} \times 85\mu\text{m}$, with an area of 0.0051 mm^2 . The yellow path demarcates the PLL loop signal flow. Attention was paid to separate analog (0.8V) and digital power domains (0.5V), whilst maintaining a compact area with convenient signal flow.

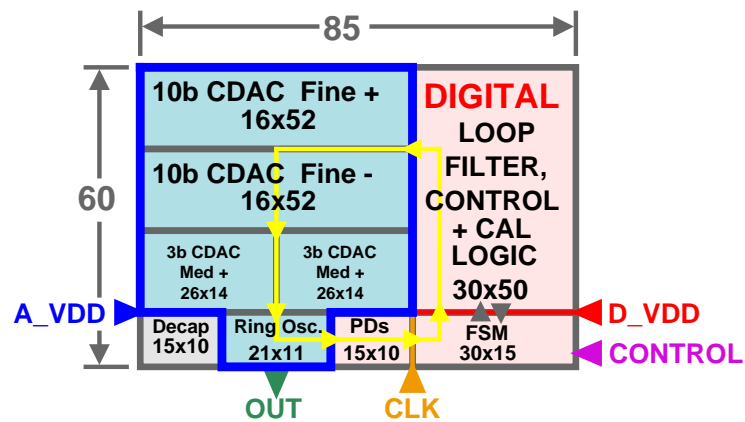


Figure 18: PLL floorplan.

4.1.7 Dividerless PLL

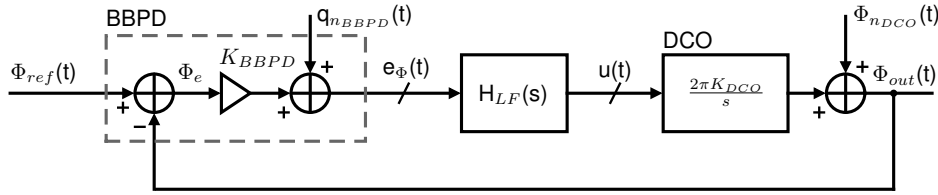


Figure 19: BBPD-PLL full noise model.

In the divider-based PLL theory (section 2.6.2), the derived PLL detector phase noise component (equation 59) contains a term proportional to N^2 , that is the detector noise will grow with the square of the PLL divider ratio. It is, however, possible to remove this N^2 dependency by usage of oscillator sub-sampling within the PLL [23]. This is achieved by directly sampling the PLL output at a rate equivalent to the reference frequency. This is equivalent to removing the divider from the PLL loop and directly connecting the PLL output to the phase detector, which has been employed in this work (see figure 16). The removal of the divider also removes any PLL noise contributions resulting from divider jitter.

In a dividerless PLL, it must be guaranteed that the PLL frequency at the start of sub-sampling operation be within $f_{ref}/2$ of the target frequency (the PLL will lock to the nearest multiple of the reference frequency). In this work, this is achieved through sequencing at startup through two phase detectors. A synchronous counter phase detector (which emulates both a divider and phase detector) initially locks the PLL within $f_{ref}/2$ of the target frequency, after which the PLL is operated in sub-sampling bang-bang phase detector.

In accordance to the change to a dividerless operation, the PLL closed loop transfer function has been rederived in equation 64. Furthermore, new expressions for PLL output phase noise with a BBPD is given in equation 65, and PLL output oscillator noise with a ring oscillator is given in equation 66, for the noise model in figure 19. Noise due to the loop filter here is ignored, as it will be possible to adjust the loop filter datapath resolution to make digital quantization noise effects negligible.

$$T(s) = \frac{\Phi_{out}(s)}{\Phi_{ref}(s)} = \frac{2\pi K_{BBPD} K_{DCO} \sum_{j=0}^Z b_j s^j}{\sum_{k=0}^P a_k s^{k+1} + 2\pi K_{BBPD} K_{DCO} \sum_{j=0}^Z b_j s^j} = \frac{L(s)}{1 + L(s)} \quad (64)$$

$$S_{\Phi n_{BBPD,out}}(f) = S_{n_{BBPD}}(f) \left| \frac{\Phi_{out}(f)}{q_{n_{BBPD}}(f)} \right|^2 = \frac{\left(\frac{\pi}{2} - 1 \right)}{f_{ref}} |\sigma_{\Phi_e} T(f)|^2 \quad (65)$$

$$S_{\Phi n_{DCO,out}}(f) = \mathcal{L}_{min}(f) \left| \frac{\Phi_{out}(f)}{q_{n_{DCO}}(f)} \right|^2 = \frac{7.33 k_B T}{P} \left(\frac{f_0}{f} \right)^2 |1 - T(f)|^2 \quad (66)$$

4.2 Bang-Bang Phase Detector

A bang-bang phase detector, as introduced in section 2.4.2, can be implemented physically with a D flip-flop [24] and logic to map the logical state to a signed ± 1 value that may be passed into a digital loop filter. This is shown in figure 20.

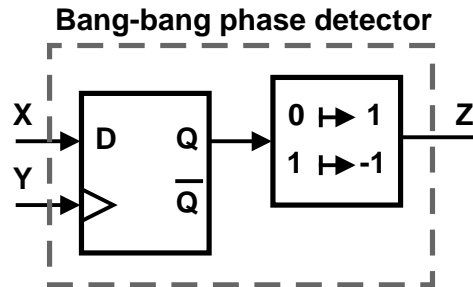


Figure 20: Bang-bang phase detector with D flip-flop.

The realization of a BBPD using a digital flip flop introduces additional noise to the system in the form of jitter. Jitter arises as an artifact of circuit and supply noise. For small time differentials between the BBPD inputs X and Y, the output can be stochastically corrupted due to the presence of noise. Furthermore, physical D flip flop implementations exhibit set-up and hold time requirements for data to be stable (to allow internal nodes to settle), so deterministic corruption of phase detection can be imparted if the inputs violate physical timing requirements. These sources of corruption cause BB-PD transfer characteristics in terms of output expectation, $\mathbb{E}[Z]$, with respect to input timing difference Δt_{XY} to deviate from an ideal step response, demonstrated in figure 21. Analytically, the corruption of the transfer characteristic can be viewed as being caused by an additive phase noise component before the signum operation in the BBPD, as shown in figure 22a. The expectation $\mathbb{E}[Z(\Delta t_{XY})]$ acts as a cumulative distribution function (CDF) for this phase noise component. Thus, differentiation of $\mathbb{E}[Z(\Delta t_{XY})]$ results in a probability distribution function (PDF) $P(T=\Delta t_{xy})$ of this phase noise signal. Statistical analysis of variance of the PDF provides an RMS value for timing jitter of this additive noise source, $\sqrt{\text{Var}[T]} = \sigma_{t,j}$. The RMS timing jitter may be converted to RMS phase error of the noise source as $\sigma_{\Phi_j} = 2\pi f_{osc}\sigma_{t,j}$. This analysis approach is applied in this work to evaluate BBPD performance.

With a model for BBPD noise due to implementation non-idealities, a modified linearized model for the BBPD will be established here. This model will reconcile the ideal BBPD noise introduced in section 2.4.3 with the noise due to the new additive jitter component just described. First, a component representing the non-ideal jitter component, Φ_j , is added into noise model from figure 19. The result is the linearized model of figure 22b. We then define a modified phase error, $\hat{\Phi}_e$, which includes the nominal Φ_e and the jitter corruption:

$$\hat{\Phi}_e = \Phi_e + \Phi_j. \quad (67)$$

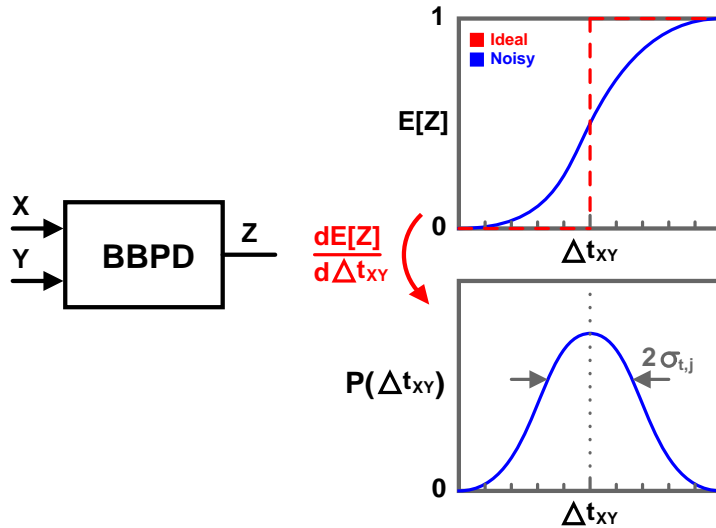


Figure 21: BBPD output expectation and jitter PDF versus input time differential.

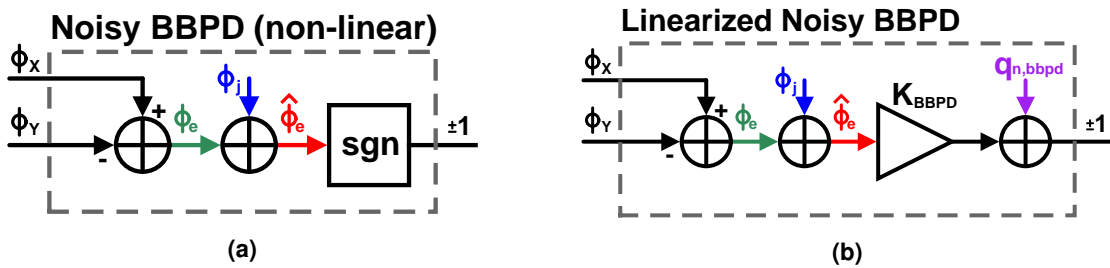


Figure 22: (a) Noisy BBPD nonlinear model (b) Noisy BBPD linearized model

$\hat{\Phi}_e$ has a variance defined as $\sigma_{\hat{\Phi}_e}^2 = \sigma_{\Phi_e}^2 + \sigma_{\Phi_j}^2$, assuming Φ_e and Φ_j are uncorrelated. Defining BBPD gain in terms of $\sigma_{\hat{\Phi}_e}$:

$$K_{BBPD} = \sqrt{\frac{2}{\pi}} \cdot \frac{1}{\sigma_{\hat{\Phi}_e}} = \sqrt{\frac{2}{\pi}} \cdot \frac{1}{\sqrt{\sigma_{\Phi_e}^2 + \sigma_{\Phi_j}^2}} \quad (68)$$

It is then observed that the output Z is valued ± 1 , thus its power is always $\sigma_Z^2 = 1$. Furthermore:

$$\sigma_Z^2 = 1 = K_{BBPD}^2 (\sigma_{\phi_e}^2 + \sigma_{\phi_j}^2) + \sigma_{q_{n,BBPD}}^2 \quad (69)$$

As determined in section 2.4.3, it is inherent that $\sigma_{q_{n,BBPD}}^2 = 1 - \frac{2}{\pi}$. If the total output noise

$$\sigma_{\phi_{n,BBPD}}^2 = \sigma_{q_{n,BBPD}}^2 + K_{BBPD}^2 \sigma_{\phi_j}^2 = 1 - \frac{2}{\pi} \frac{\sigma_{\phi_e}^2}{\sigma_{\phi_j}^2 + \sigma_{\phi_e}^2} \quad (70)$$

If the BB-PD is connected directly to oscillator output, $\sigma_{\phi_e}^2 = \sigma_{\phi_n}^2$, i.e. the PLL output phase noise. The spectral density of the BB-PD phase noise is then:

$$S_{\phi_{n,BBPD}} = \frac{\sigma_{\phi_{n,BBPD}}^2}{f_{ref}} = \frac{1 - \frac{2}{\pi} \frac{\sigma_{\phi_n}^2}{\sigma_{\phi_j}^2 + \sigma_{\phi_n}^2}}{f_{ref}} \quad (71)$$

$$S_{\Phi n_{BBPD,out}}(f) = S_{n_{BBPD}}(f) \left| \frac{\Phi_{out}(f)}{q_{n_{BBPD}}(f)} \right|^2 = \frac{\frac{\pi}{2}(\sigma_{\phi_j}^2 + \sigma_{\phi_n}^2) - \sigma_{\phi_n}^2}{f_{ref}} |T(f)|^2 \quad (72)$$

4.2.1 Circuit

The physical implementation of the bang-bang phase detector has been selected to utilize a true single phase clock (TSPC) D-flip flop [25]. The positive-edge triggered variant of this circuit has been implemented as shown in figure 23. Selection of this topology was based on the desire for the usage of a single ended clock as a reference signal.

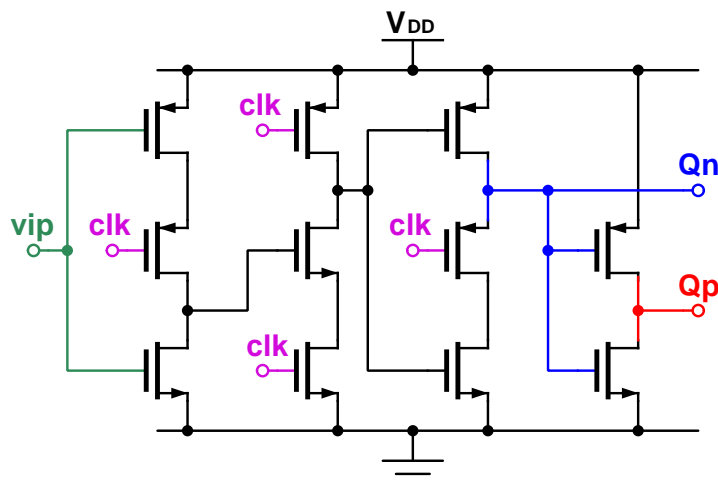


Figure 23: True single-phase clock (TSPC) D flip-flop, positive edge triggered.

This TSPC design was validated in simulation with RVT devices with all devices set with $(W/L) = \{100n/20n, 200n/20n\}$, and with supply voltages of 0.5 and 0.8 volts. Results for the RMS jitter and power consumption are in table 3. For implementation $(W/L) = 200n/20n$ was selected for all devices, as the requirement of $10 \mu\text{W}$ is met with layout parasitics, whilst having low jitter. Final simulation results for the BBPD are in results section 5.8, and the layout in appendix A.6.

(W/L)	Supply [V]	RMS jitter [ps]	Power [μW]
100n/20n	0.5	6.01	1.64
100n/20n	0.8	0.832	3.942
200n/20n	0.5	1.776	2.215
200n/20n	0.8	0.496	4.591

Table 3: Schematic simulation of TSPC DFF.

4.3 Voltage Controlled Ring oscillator

Oscillator circuits implemented in CMOS technology either fall under the category of resonant LC circuits, or RC based ring and relaxation oscillators. LC circuits provide favorable phase noise performance, as seen in figure 14, which demonstrates phase noise improvements on the order of 20 dB for LC designs over RC designs that have been published. This is due to the inherent nature of an LC circuit, as the higher the quality factor it has, the narrower the resonance line width and consequent phase noise is. In the ultra-low power domain of this work, however, ring oscillators pose several advantages over LC designs. These include substantially smaller integration area due to no need for integrated inductors, simpler design, convenient rail-to-rail signal levels, and lower achievable minimum power at a given frequency. Also significant, is the ability to instantly start up a ring oscillator, which can be achieved with known phase if using appropriate reset circuitry. Coupled with the BBPD, which is a phase only detector (which is not able to detect frequency), the ability to start the oscillator with a known zero-phase, in tandem with being able to set the digital loop filter to a zeroed state, enables faster and more consistent locking compared to randomized initial phase. With the intent of this design to allow for fast duty cycled operation, the need for fast start up is imperative, thus for this reason a ring oscillator topology has been selected for this work.

It has been decided in this work to exploit the ability of the FD-SOI backgate terminal to alter threshold voltage in order to implement a backgate voltage controlled ring oscillator as the main PLL VCO. As will be shown in the following sections, backgate tuning results in transconductor modulation within the ring oscillator, which therefore modulates the RC time constant of the delay stages, and consequently the frequency of oscillation. A novel delay cell topology which exploits FD-SOI backgates to implement both differential operation and frequency is subsequently introduced. The described design enables usage of capacitive DACs to set oscillator control voltages, leading to minimal extra power consumption needed to convert the voltage controlled ring oscillator into a DCO.

4.3.1 22FDX considerations

To analyze the body effect with FD-SOI backgates in 22FDX, SPICE simulations to extract the body effect coefficient γ and threshold voltage V_{TH} for different channel lengths and bias conditions have been performed. Parameters for threshold voltage, and transconductances g_m and g_{mb} have been extracted using DC operating point simulations. Noting the relation from 13, where $g_{mb} = \gamma g_m$, γ can be deduced from operating point g_m and g_{mb} values. Figures 24a and 24b show the extracted threshold voltage versus backgate bias and the slope of that relationship. Figures 25a and 25b show the extracted threshold voltage and body effect coefficient versus channel length. Table 4 provides extracted N-channel device parameters, and table 5 provides extracted P-channel devices parameters.

4. DESIGN

It is observed that the threshold voltage slopes of figure 24 are not perfectly linear, but for the simplified analytical purposes of this work, they can be approximated as linear. The P-channel devices in 22FDX show a high degree of linearity, whereas the N-channel devices show variation in slope as in figure 24b. It is also observed that the threshold voltage and body effect coefficient vary as channel lengths approach zero, but flatten out for longer device length. A final note is there is substantial variation of γ and V_{TH} between device types, so prudent care must be taken in the oscillator for selection of devices and their sizing.

$$V_{th} = V_{th0} - \gamma V_{BS} \quad (73)$$

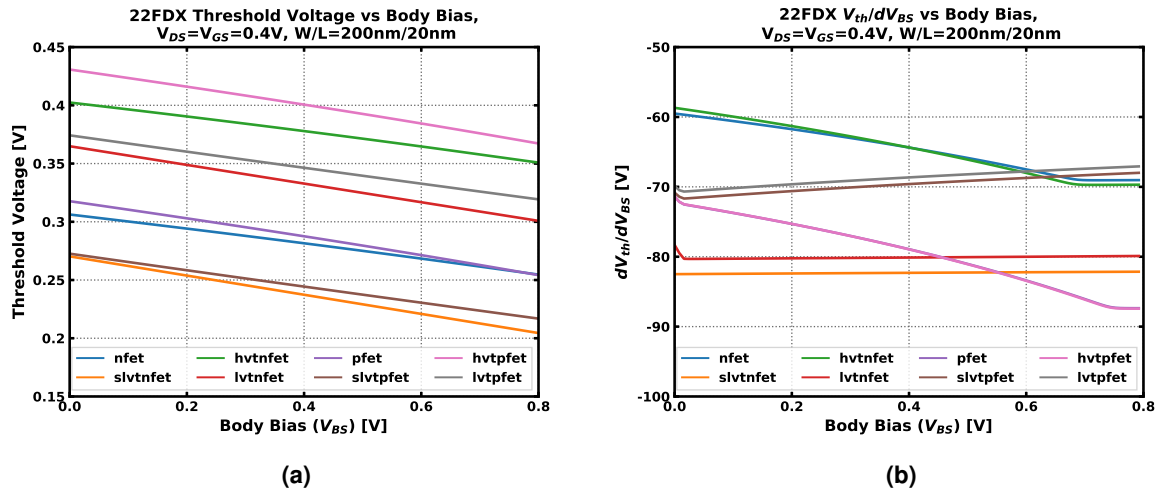


Figure 24: (a) 22 FDX threshold voltage versus body bias, (b) Rate of change of threshold voltage versus body bias.

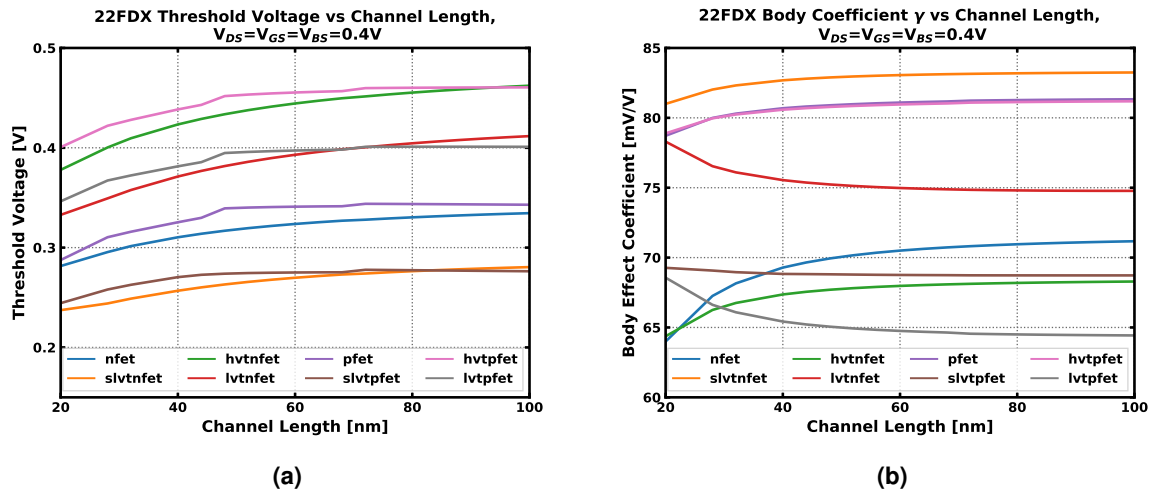


Figure 25: (a) 22 FDX extracted threshold voltage versus channel length, (b) Extracted body effect coefficient.

Device	L [nm]	W [nm]	V_{th} [mV]	γ [mV/V]
nfet	20	100	306.3	59.14
nfet	100	500	376.4	65.4
slvtnfet	20	100	270.3	81.38
slvtnfet	100	500	326.7	83.23
hvt_nfet	20	100	402.4	58.85
hvt_nfet	100	500	513.5	61.96
lvtnfet	20	100	364.9	77.72
lvtnfet	100	500	466.3	74.85

Table 4: 22FDX core NFET threshold voltage and body effect coefficient extraction.

Device	L [nm]	W [nm]	V_{th} [mV]	γ [mV/V]
pfet	20	100	317.7	71.51
pfet	100	500	366.8	74.32
slvtpfet	20	100	272.6	71.09
slvtpfet	100	500	294.4	70.79
hvt_pfet	20	100	430.7	71.28
hvt_pfet	100	500	488.4	74.23
lvtpfet	20	100	374.2	69.93
lvtpfet	100	500	422.8	66.43

Table 5: 22FDX core PFET threshold voltage and body effect coefficient extraction.

4.3.2 Channel length consideration

Scaling of device channel length has a great impact on phase noise for ring oscillators, according to [26] takes form of equation 74. V_{DD} is the supply voltage, V_t is the threshold voltage, P_{DC} is the oscillator power consumption, γ_p and γ_n are the respective PMOS and NMOS noise factors, f_0 is the oscillator frequency, and f is the offset from the carrier for the phase noise. It is expected that excess noise factor of the transistor will increase with decreasing channel length [27], thus unavoidably phase noise will also increase with decreasing length following equation 74. To analyze the effect of channel length on ring oscillator performance in 22FDX technology, a 5-stage single ended ring oscillator was simulated for channel lengths between 20-500nm, with a fixed (W/L) = 5 and no external loading. The resulting phase noise FOM_{pn} data is shown in figure 26a, oscillator frequency in figure 26b, oscillator power in figure 27a, and phase noise at offset 1 MHz from the carrier in figure 27b. The phase noise FOM is that defined in equation 49. It is seen that FOM degrades as expected near minimum channel length, and improves asymptotically as the channel length grows. The asymptote closely correlates to that predicted theoretically for RC based oscillators, in equation 53. At 300K, as simulated,

4. DESIGN

this is -165.2 dB. Better (i.e. lower valued) FOM corresponds to better phase noise per unit of oscillator power expenditure. Thus, based on the data of figure 26a, the best design strategy to minimize phase noise for a fixed power budget is to use the longest possible channel length. Channel length limits frequency of operation, as seen in figure 26b, so there is a trade off between frequency of operation and achievable FOM.

$$\mathcal{L}(f) = \frac{2kT}{P_{DC}} \left(\frac{V_{DD}}{V_{DD} - V_t} (\gamma_N + \gamma_P + 1) \right) \left(\frac{f_0}{f} \right)^2 \quad (74)$$

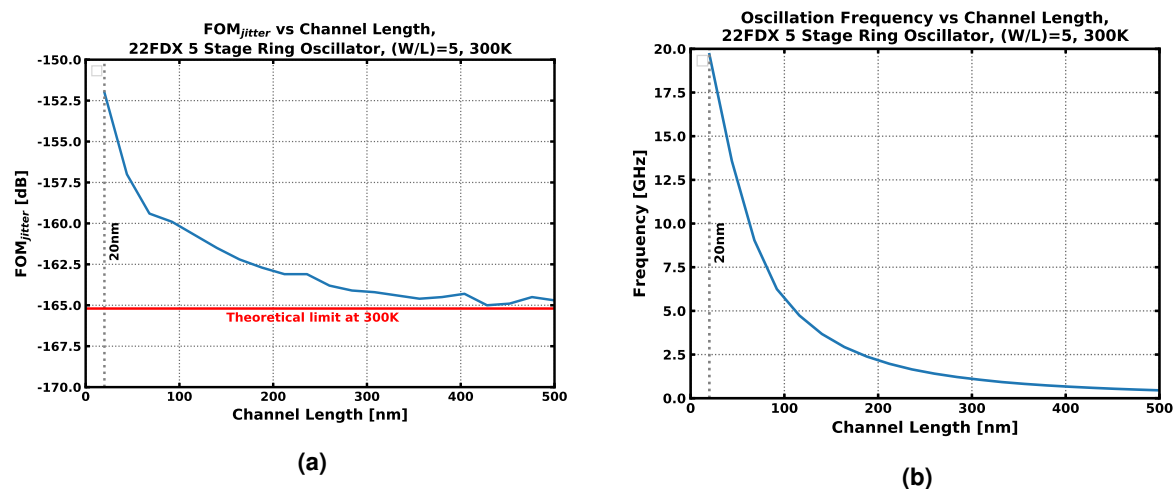


Figure 26: 22FDX ring oscillator channel length sweep versus (a) FOM, (b) Oscillation frequency.

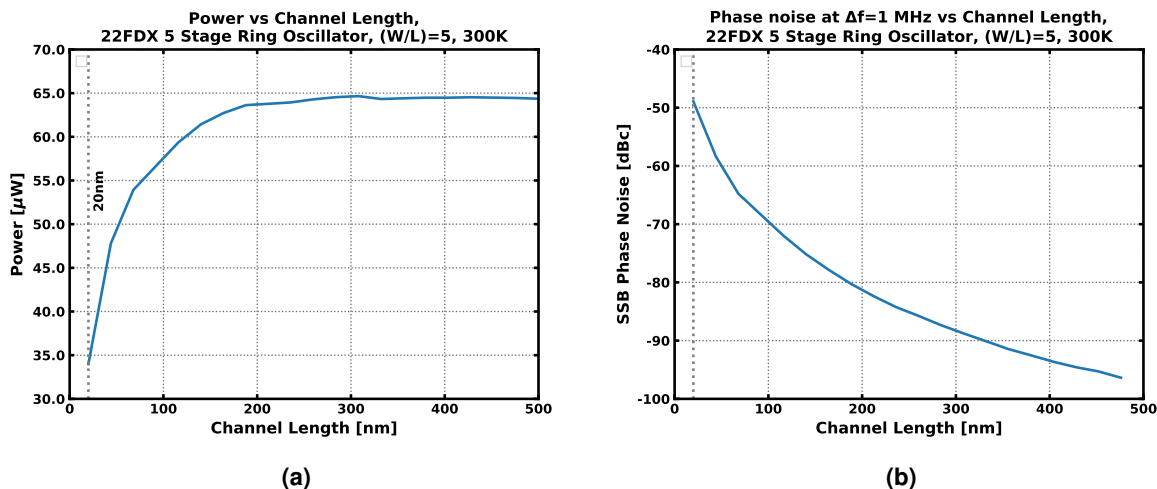


Figure 27: 22FDX ring oscillator channel length sweep versus (a) Power, (b) Phase noise at 1 MHz carrier offset (SSB).

4.3.3 Ring oscillator frequency derivation

To analyze the effect of backgate tuning on a FD-SOI ring oscillator, a general mathematical model for CMOS ring oscillators will be developed first here. To begin, an approximate model

for a CMOS inverter will first be considered. A common model for delay in digital circuits is an RC circuit, where the MOSFET channels are approximated with an averaged conductance value $\langle g_{ch} \rangle$, and the output node is approximated to have a capacitance of C . With such a model, a ring oscillator is assumed to have waveforms that are decaying exponentials, with time constant $\tau = \langle g_{ch} \rangle^{-1}C$. In context of the 3-stage ring oscillator of figure 28, figure 29 demonstrates the described inverter model and the resulting input and output waveforms.

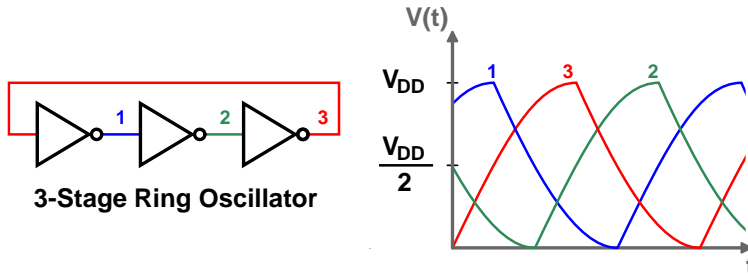


Figure 28: Model for ring oscillator.

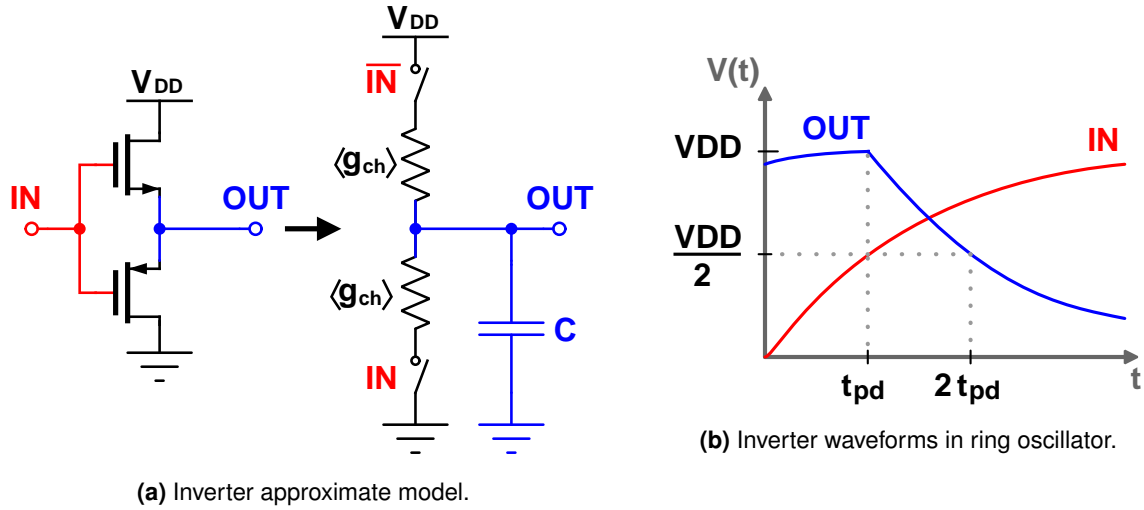


Figure 29: Approximate model for ring oscillator inverter delay cell.

To calculate oscillation frequency ring oscillator from the RC model, several inferences are made:

- The switching point V_M of the inverters is $V_{DD}/2$, based on the assumption that the NMOS and PMOS are of equal strength.
- The output of an inverter will have a decaying exponential which starts coincident with the passing of V_M at the input.
- The propagation delay t_{pd} for an inverter will be the time differential between the V_M crossing points on the input and output.
- The oscillator frequency will be $f_{osc} = 1/2Nt_{pd}$, where N is the number of stages (i.e. defined by $2N$ propagation delays).

4. DESIGN

Given the falling edge inverter waveform equation in 75, and observing that t_{pd} occurs at the point where $V(t) = V_{DD}/2$, it is found that $t_{pd} = \tau \ln(2)$. Finally, using the aforementioned assumptions, the equation for oscillator frequency in equation 76.

$$V(t) = V_{DD} \cdot e^{\frac{-t}{\tau}} \cdot u(t) \quad (75)$$

$$f_{osc}^{-1} = 2Nt_{pd} = \frac{2 \ln(2)NC}{\langle g_{ch} \rangle} \quad (76)$$

4.3.4 Finding $\langle g_{ch} \rangle$ and C

The node capacitance C is trivial to find based on the inverter gate capacitance and a lumped load capacitance term C_L :

$$C = C_{ox} (W_N L_N + W_P L_N) + C_L \quad (77)$$

The average channel conductance $\langle g_{ch} \rangle$ is more involved to find. To do so, several assumptions are made:

- $L \gg L_{min}$, so no velocity saturation, and therefore square law is applicable.
- NMOS and PMOS have equal V_{TH} and transconductance.
- Output transition occur with the active FET in saturation from the start of the transition until t_{pd} after the start of the transition. This requires:
 - $V_{DD}/4 < V_{TH} < V_{DD}/2$

Following those assumptions, $\langle g_{ch} \rangle$ can be computed via integration within the period t_{pd} :

$$\langle g_{ch} \rangle = \frac{1}{t_{pd}} \int_0^{t_{pd}} \frac{I_{out}(t)}{V_{out}(t)} dt \quad (78)$$

I_{out} is computed using the saturated MOSFET square law model an exponential waveforms assumptions. An I_{short} term is included to account for output current reduction from short-circuit conduction when both PMOS and NMOS are conducting.

$$I_{out}(t) = \frac{k_n}{2} \left(\frac{W}{L} \right)_n [(V_{in}(t) - V_{TH})^2] - I_{short} \quad (79)$$

$$= \frac{k_n}{2} \left(\frac{W}{L} \right)_n \left[(V_{DD} (1 - e^{-t/\tau}) - V_{TH})^2 - \left(\frac{V_{DD}}{2} - V_{TH} \right)^2 \right] \quad (80)$$

$k_n = \mu_n C_{ox}$, with the equal PMOS/NMOS assumption, $k_n (\frac{W}{L})_n = k_p (\frac{W}{L})_p$. V_{out} is simply a decaying exponential with a delay t_{pd} versus the input:

$$V_{out}(t) = V_{DD} e^{-(t-t_{pd})/\tau} u(t) \quad (81)$$

Now, computing the integral for $\langle g_{ch} \rangle$ yields:

$$\langle g_{ch} \rangle = \frac{1}{2} \mu_n C_{ox} \left(\frac{W}{L} \right)_n \left[V_{DD} \left(\frac{7}{8 \ln 2} - 1 \right) - V_{TH} \left(\frac{1}{\ln 2} - 1 \right) \right] \quad (82)$$

As a simplification, α is defined as:

$$\alpha = \left[V_{DD} \left(\frac{7}{8 \ln 2} - 1 \right) - V_{TH} \left(\frac{1}{\ln 2} - 1 \right) \right] \quad (83)$$

4.3.5 Handling unequal NMOS/PMOS

In the case of different threshold voltages for NMOS and PMOS:

$$f_{osc}^{-1} = N(t_{pdn} + t_{pdp}) = \ln(2) NC \left(\frac{1}{\langle g_{ch} \rangle_n} + \frac{1}{\langle g_{ch} \rangle_p} \right) = \frac{2 \ln(2) NC}{\langle g_{ch} \rangle'} \quad (84)$$

A modified $\langle g_{ch} \rangle'$ is defined:

$$\langle g_{ch} \rangle' = 2 \left(\frac{1}{\langle g_{ch} \rangle_n} + \frac{1}{\langle g_{ch} \rangle_p} \right)^{-1} = 2 \frac{\langle g_{ch} \rangle_n \langle g_{ch} \rangle_p}{\langle g_{ch} \rangle_n + \langle g_{ch} \rangle_p} = 2 \frac{\frac{1}{2} \mu_n C_{ox} \left(\frac{W}{L} \right)_n \alpha_n \frac{1}{2} \mu_p C_{ox} \left(\frac{W}{L} \right)_p \alpha_p}{\frac{1}{2} \mu_n C_{ox} \left(\frac{W}{L} \right)_n \alpha_n + \frac{1}{2} \mu_p C_{ox} \left(\frac{W}{L} \right)_p \alpha_p} \quad (85)$$

This is somewhat unmanagable, however enforcing $\mu_n C_{ox} \left(\frac{W}{L} \right)_n = \mu_p C_{ox} \left(\frac{W}{L} \right)_p$ for V_M to equal $V_{DD}/2$ gives:

$$\langle g_{ch} \rangle' = \frac{1}{2} \mu_n C_{ox} \left(\frac{W}{L} \right)_n \frac{2 \alpha_n \alpha_p}{\alpha_n + \alpha_p} = \frac{1}{2} \mu_n C_{ox} \left(\frac{W}{L} \right)_n \alpha' \quad (86)$$

Thus α_n and α_p are found for the according threshold voltages and then $\langle g_{ch} \rangle$ can be found.

$$\alpha' = \frac{2 \alpha_n \alpha_p}{\alpha_n + \alpha_p} \quad (87)$$

4.3.6 Solving for oscillator frequency and power

Solving for oscillator frequency:

$$f_{osc} = \frac{\mu_n C_{ox}}{4 \ln 2 NC} \left(\frac{W}{L} \right)_n \left[V_{DD} \left(\frac{7}{8 \ln 2} - 1 \right) - V_{TH} \left(\frac{1}{\ln 2} - 1 \right) \right] \quad (88)$$

4. DESIGN

If gate capacitance is the dominant load component, and PMOS/NMOS are equal sized such that $C = 2WLC_{ox}$:

$$f_{osc} = \frac{\mu_n}{8 \ln 2N} \cdot \frac{1}{L^2} \left[V_{DD} \left(\frac{7}{8 \ln 2} - 1 \right) - V_{TH} \left(\frac{1}{\ln 2} - 1 \right) \right] \quad (89)$$

Power can also be calculated, knowing in digital circuits $P = fC_{\Sigma}V_{DD}^2$, where C_{Σ} is the total capacitance of the active nodes. Thus:

$$P_{osc} = N f_{osc} C V_{DD}^2 = \frac{\mu_n C_{ox}}{4 \ln 2} \left(\frac{W}{L} \right)_n \left[V_{DD} \left(\frac{7}{8 \ln 2} - 1 \right) - V_{TH} \left(\frac{1}{\ln 2} - 1 \right) \right] \quad (90)$$

It should be noted that the power consumption is proportional to FET aspect ratio (W/L), regardless of the load.

4.3.7 Ring oscillator backgate tuning derivation

Using the basic expressions for ring oscillator frequency, the frequency characteristics under backgate biasing can be found. In FD-SOI, the threshold voltage of a FET varies with linear dependence on the applied back gate bias V_{BG} (relative to source). Given the body effect coefficient of a process, γ , V_t is:

$$V_{TH} = V_{t0} - \gamma V_{BG} \quad (91)$$

Using this in the ring oscillator frequency equation:

$$f_{osc} = \frac{\mu_n C_{ox}}{4 \ln 2NC} \left(\frac{W}{L} \right)_n \left[V_{DD} \left(\frac{7}{8 \ln 2} - 1 \right) - V_{t0} \left(\frac{1}{\ln 2} - 1 \right) + \gamma V_{BG} \left(\frac{1}{\ln 2} - 1 \right) \right] \quad (92)$$

Equivalently, $f_{osc} = f_{0,osc} + \Delta f_{osc}(V_{BG})$, provided $f_{0,osc}$ is the frequency with no backgate bias where. Thus it is found that:

$$\Delta f_{osc}(V_{BG}) = \gamma V_{BG} \frac{\mu_n C_{ox}}{4 \ln 2NC} \left(\frac{W}{L} \right)_n \left[\frac{1}{\ln 2} - 1 \right] = K_{VCO} \quad (93)$$

The important finding here is that the change in oscillator frequency is linear with backgate voltage, that is $\Delta f_{osc} \propto V_{BG}$. The expression of 93 also happens to be the oscillator VCO gain, K_{VCO} . Given the wide voltage range that FD-SOI backgates may be biased to, this implies that a highly linear VCO with wide input range may be implemented with backgate tuning. If the backgate voltage is constrained in the range $[0, V_{DD}]$, the center frequency f_c of such a VCO is then:

$$f_c = \frac{\mu_n C_{ox}}{4 \ln 2NC} \left(\frac{W}{L} \right)_n \left[V_{DD} \left(\frac{7}{8 \ln 2} - 1 + \frac{\gamma}{2 \ln 2} - \frac{\gamma}{2} \right) - V_{t0} \left(\frac{1}{\ln 2} - 1 \right) \right] \quad (94)$$

Correspondingly, the tuning range with $V_{BG} \in [0, V_{DD}]$ is:

$$\Delta f = \gamma V_{DD} \frac{\mu_n C_{ox}}{4 \ln 2 N C} \left(\frac{W}{L} \right)_n \left[\frac{1}{\ln 2} - 1 \right] \quad (95)$$

Finally, the fractional tuning range of the oscillator found to be that of equation 96. Notice that this is only a function of supply voltage V_{DD} , nominal threshold voltage V_{t0} and body effect coefficient γ .

$$\frac{\Delta f}{f_c} = \frac{\gamma V_{DD} (1 - \ln 2)}{V_{DD} \left(\frac{7}{8} - \ln 2 + \frac{\gamma}{2} - \frac{\gamma}{2} \ln 2 \right) - V_{t0} (1 - \ln 2)} \quad (96)$$

If a N-bit DAC is used to control the oscillator, the resulting DCO gain is therefore:

$$K_{DCO} = \frac{\Delta f}{2^{N_{DAC}}} = \frac{f_c}{2^{N_{DAC}}} \cdot \frac{\gamma V_{DD} (1 - \ln 2)}{V_{DD} \left(\frac{7}{8} - \ln 2 + \frac{\gamma}{2} - \frac{\gamma}{2} \ln 2 \right) - V_{t0} (1 - \ln 2)} \quad (97)$$

4.3.8 DCO Gain Uncertainty

The DCO gain K_{DCO} is used in setting the loop filter coefficients, so the uncertainty of the DCO gain is of interest to allow for statistical analysis of the PLL across process variation. The uncertainty of K_{DCO} (normalized with nominal K_{DCO} value) as a function of V_{DD} , V_{t0} and γ is:

$$\sigma_{KDCO} = \sqrt{\left(\frac{\partial K_{DCO}}{\partial V_{DD}} \cdot \frac{\sigma_{VDD}}{K_{DCO}} \right)^2 + \left(\frac{\partial K_{DCO}}{\partial V_{t0}} \cdot \frac{\sigma_{Vt0}}{K_{DCO}} \right)^2 + \left(\frac{\partial K_{DCO}}{\partial \gamma} \cdot \frac{\sigma_\gamma}{K_{DCO}} \right)^2} \quad (98)$$

$$\frac{\partial K_{DCO}}{\partial V_{DD}} = \frac{f_c}{2^{N_{DAC}+1}} \cdot \frac{-\gamma V_{t0} (1 - \ln 2)^2}{\left[V_{DD} \left(\frac{7}{8} - \ln 2 + \frac{\gamma}{2} - \frac{\gamma}{2} \ln 2 \right) - V_{t0} (1 - \ln 2) \right]^2} \quad (99)$$

$$\frac{\partial K_{DCO}}{\partial V_{t0}} = \frac{f_c}{2^{N_{DAC}+1}} \cdot \frac{\gamma V_{DD} (1 - \ln 2)^2}{\left[V_{DD} \left(\frac{7}{8} - \ln 2 + \frac{\gamma}{2} - \frac{\gamma}{2} \ln 2 \right) - V_{t0} (1 - \ln 2) \right]^2} \quad (100)$$

$$\frac{\partial K_{DCO}}{\partial \gamma} = \frac{f_c}{2^{N_{DAC}+1}} \cdot \frac{V_{DD} \cdot (1 - \ln 2) \left[V_{DD} \left(\frac{7}{8} - \ln 2 \right) - V_{t0} (1 - \ln 2) \right]}{\left[V_{DD} \left(\frac{7}{8} - \ln 2 + \frac{\gamma}{2} - \frac{\gamma}{2} \ln 2 \right) - V_{t0} (1 - \ln 2) \right]^2} \quad (101)$$

Simplified:

$$\sigma_{KDCO} = \frac{1}{\sqrt{\left((\gamma V_{t0} (1 - \ln 2) \sigma_{VDD})^2 + (\gamma V_{DD} (1 - \ln 2) \sigma_{Vt0})^2 + \left(V_{DD} \left[V_{DD} \left(\frac{7}{8} - \ln 2 \right) - V_{t0} (1 - \ln 2) \right] \sigma_\gamma \right)^2 \right)}} \quad (102)$$

4.3.9 Backgate-controlled Ring Oscillator Sensitivity Analysis

The frequency tuning sensitivity of the ring oscillator for supply and backgate voltages will be compared. First the following is defined, following that the derived equations for oscillator frequency are linear.

$$f_{osc}(V_{DD} + \Delta V_{DD}) = f_{osc}(V_{DD}) + f_{osc}(\Delta V_{DD}) \quad (103)$$

$$f_{osc}(V_{DD}) = f_0 \quad (104)$$

$$f_{osc}(\Delta V_{DD}) = \Delta f \quad (105)$$

In the case of supply voltage tuning, the change (proportion) of frequency per voltage of applied extra bias is (evaluated at zero back-gate bias):

$$S_{V_{DD}}^{f_{osc}} = \frac{\Delta f}{f_0} \cdot \frac{1}{\Delta V_{DD}} = \frac{\left(\frac{7}{8 \ln 2} - 1\right)}{V_{DD} \left(\frac{7}{8 \ln 2} - 1\right) - V_{t0} \left(\frac{1}{\ln 2} - 1\right)} \quad (106)$$

With $V_{DD} = 0.8$, $V_{t0} = 0.3$ (approximately true for 22FDX devices), it is expected 340% change in frequency will result per extra volt of applied bias. Of course, this is linearized, and one does not expect to apply an extra 1V of supply bias to a 0.8V oscillator. Realistically, the supply can be tuned $\pm 10\%$, which corresponds to a $\pm 27.2\%$ tuning range of the oscillator. Supply tuning stands as a viable coarse tuning mechanism for the oscillator, however, fine tuning is more limited due to difficulty in achieving small resolution step (e.g 10 bits in $V_{DD} = 0.8\text{V}$ $\pm 10\%$ corresponds to $156 \mu\text{V}/\text{LSB}$, and $26 \text{ m\%}/\text{LSB}$ of frequency tuning).

In the case of backgate tuning, the change (proportion) of frequency per volt of applied backgate bias is:

$$S_{V_{BG}}^{f_{osc}} = \frac{\Delta f}{f_0} \cdot \frac{1}{\Delta V_{BG}} = \frac{\gamma \left(\frac{1}{\ln 2} - 1\right)}{V_{DD} \left(\frac{7}{8 \ln 2} - 1\right) - V_{t0} \left(\frac{1}{\ln 2} - 1\right)} \quad (107)$$

With $\gamma=0.07$, $V_{DD}=0.8$, $V_{t0}=0.3$, as is typical in 22FDX, it is expected a 29.5% change in frequency will result per volt applied of backgate bias. This is much finer than achieved with supply voltage tuning. The ratio of frequency sensitivity to supply and backgate voltage tuning is:

$$\frac{S_{V_{DD}}^{f_{osc}}}{S_{V_{BG}}^{f_{osc}}} = \frac{\frac{7}{8 \ln 2} - 1}{\gamma \left(\frac{1}{\ln 2} - 1\right)} \quad (108)$$

Under the aforementioned biasing conditions, it is expected that 8.4x finer control can be achieved with backgate tuning. The wide backgate voltage ranges allowed for with FD-SOI technology permit for design of a voltage-DAC based control scheme which will achieve far smaller frequency resolution than with supply voltage tuning.

4.3.10 Capacitor-based coarse tuning scheme

It is observed that oscillator frequency of ring oscillator is capacitance dependent. Thus if a bank of quantized capacitances may be switched into the oscillator, coarse control of frequency can be implemented. Figure 30 demonstrates the effect of such a tuning scheme, for increasing capacitance settings C_0-C_3 . Under such a scheme it is important to ensure that the frequency ranges achieved through backgate tuning overlap between successive capacitor settings to ensure continuity of frequencies accessible by the oscillator.

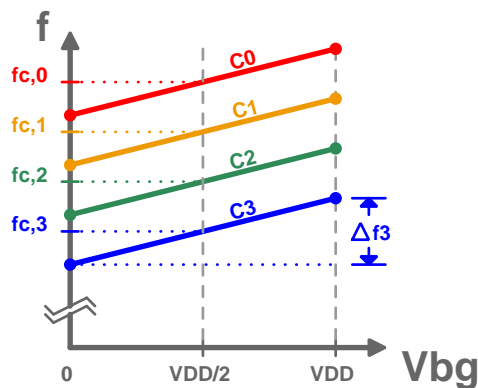


Figure 30: Backgate-tuned ring oscillator with coarse tuning capacitor bank.

4.3.11 Pseudodifferential Backgate-Coupled Inverter Delay Cell

To utilize backgate tuning for frequency control, a suitable delay cell design must be devised. Accordingly, the delay topology used in this work has been derived from the FD-SOI pseudodifferential backgate coupled inverter delay cell of [28], shown in figure 31. This inverter uses two single ended FD-SOI inverters, with the backgates of the transistors in a given inverter connected together. This is implemented with a common well structure below the two transistors of each inverter. Nominally, to avoid forward biasing of the well-substrate diodes, a N-doped well or a triple well is used, with well potentials constrained to be ≥ 0 . The result of this well configuration and the FD-SOI BOX layer is that the backgate terminals of the PMOS and NMOS may be tuned in tandem across a wide positive voltage range. This is not possible in bulk technology. In 22FDX, such well configurations allow biasing from 0 to +2V, which is inclusive of the full rail-to-rail range of a circuit supplied with $V_{DD} = 0.8V$, as in this work. Thus, in figure 31, when the two FD-SOI sub-cells inverter cells connected with the shown cross-coupled output and backgate configuration, safe well biasing is achieved. The backgate cross-coupled configuration has the effect of inducing differential behavior in the circuit, as positive feedback is introduced. It should be noted that cell of figure 31 does not employ back gate tuning to tune frequency. This work proposes a modification to the topology which implements backgate differential coupling and backgate frequency tuning.

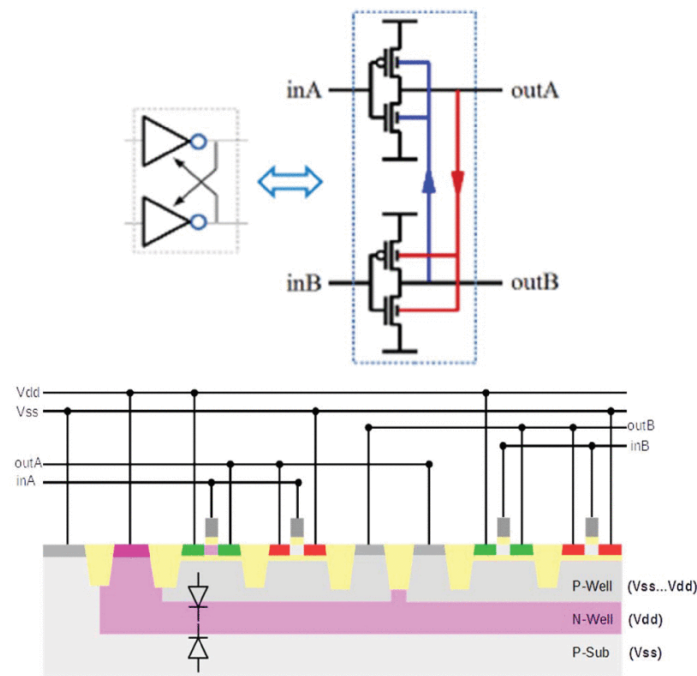


Figure 31: FD-SOI backgate-coupled inverter topology, .

The emergence of differential behavior in this delay cell can be understood through circuit analysis. First, the common backgate inverter cell (figure 32a) is converted to a linearized model, for an arbitrary bias point, in figure 32b. A simplification of the linearized model is arrived at by lumping terms together, giving figure 32c. Using the linearized model of figure

32c, a linearized version of the pseudodifferential inverter circuit is then arrived at in figures 33a and 33b. It is observed that transconductors $-G_{mb}$ in figure 33b couple the two outputs with positive feedback loop. Therefore, any differential components generated via the feed forward terms $-G_m R_o v_{in}$ and $-G_m R_o v_{ip}$ will be positively amplified by the cross coupling. Elementary circuit analysis for differential gain of the linear circuit in figure 33b leads to the expression in equation 109.

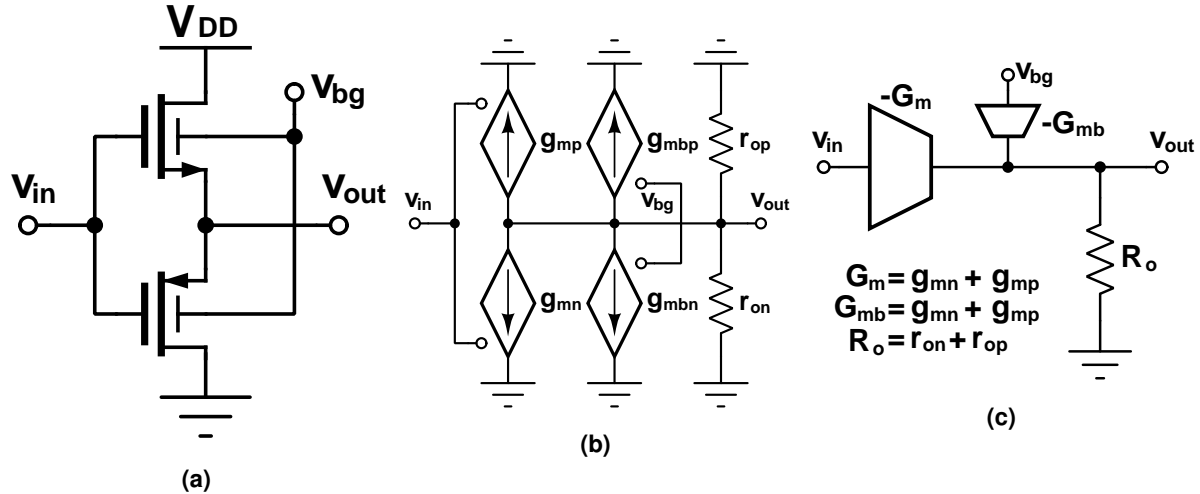


Figure 32: (a) Common backgate inverter, (b) Linearized circuit, (c) Simplified linearized model.

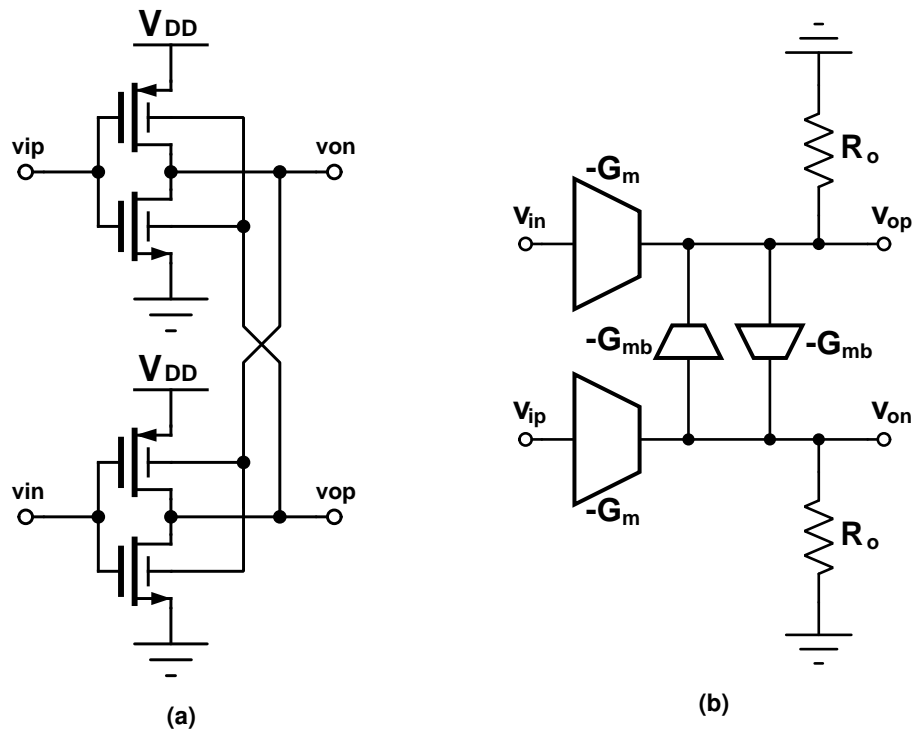


Figure 33: (a) Pseudodifferential backgate-coupled inverter circuit, (b) Linearized circuit.

$$A_{DM} = \frac{G_m R_o + G_{mb}^2 R_o^2}{1 - G_{mb}^2 R_o^2} \quad (109)$$

Using the relation $G_{mb} = \gamma G_m$ found in equation 13, equation 109 can be simplified to 110

4. DESIGN

(this is assuming PMOS and NMOS have approximately equal γ). In the special case where $\gamma G_m R_o \approx 1$, the differential gain of the delay cell can be very high, implying the pseudodifferential coupling can be very effective at inducing differential behavior. A major advantage of this topology is that it is implemented using only two inverters, unlike typical differential pair circuits which rely on current biasing to achieve differential behavior. The removal of the need for current biasing reduces power consumption, as no bias generators are required. Circuit noise is also reduced due to fewer total transistors generating noise in the circuit.

$$A_{DM} = \frac{G_m R_o}{1 - \gamma G_m R_o} \quad (110)$$

For the sake of completeness, the common mode gain of the circuit has also been determined by the same method, given in equation 111.

$$A_{CM} = \frac{G_m R_o}{1 + \gamma G_m R_o} \quad (111)$$

4.3.12 Optimal Selection of Backgate-Couple Pseudodifferential Inverter Devices

For positive voltage well biasing in 22FDX, devices that are over N-wells must be used. In 22FDX, these are PFET, HVTPFET, SLVTNFET, LVTNFET. The devices should be relatively matched in terms of threshold voltage and body effect coefficient. Referencing the extracted device parameters in tables 4 and 5. HVTPFET is not considered here due to the high threshold voltage, being greater than $V_{DD}/2$ for $V_{DD} = 0.8$. Thus, an optimization for ratio of inverter W_P/W_N for the circuit shown in figure 34 was performed. This circuit is used to determine the common mode level of the inverter V_M of the inverter achieved through self-biasing. This level should be ideally at $V_{DD}/2$, thus the optimization simulation run determined the optimal W_P/W_N required in order to achieve $V_M = V_{DD}/2$. This optimization was run for inverters of PFET + LVTNFET devices, and PFET + SLVTNFET devices. The result of this optimization is in figure 35. It is seen that for PFET + SLVTNFET, large W_P/W_N ratios are required, on the order of 5 or greater. In the PFET + LVTNFET combination, a near unity ratio is achieved, with $W_P/W_N \in [0.8, 1.5]$ for $L \in [20, 100]$ nm. It is of interest to keep device sizes similar to reduce device capacitance, so the selection of PFET + LVTNFET devices in 22FDX is the optimal device combination for backgate-coupled pseudodifferential inverter implementation. These devices also possess close backgate coefficients, for LVTNFET $\gamma \in [77.72, 74.85]$ mV/V and for PFET $\gamma \in [71.51, 74.32]$ mV/V, for $L \in [20, 100]$ nm.

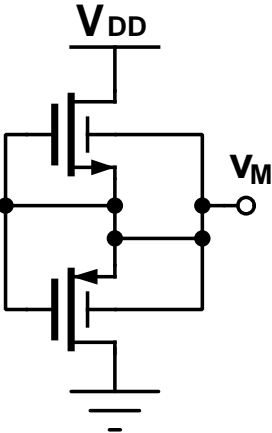


Figure 34: Circuit to extract self-biased common mode level.

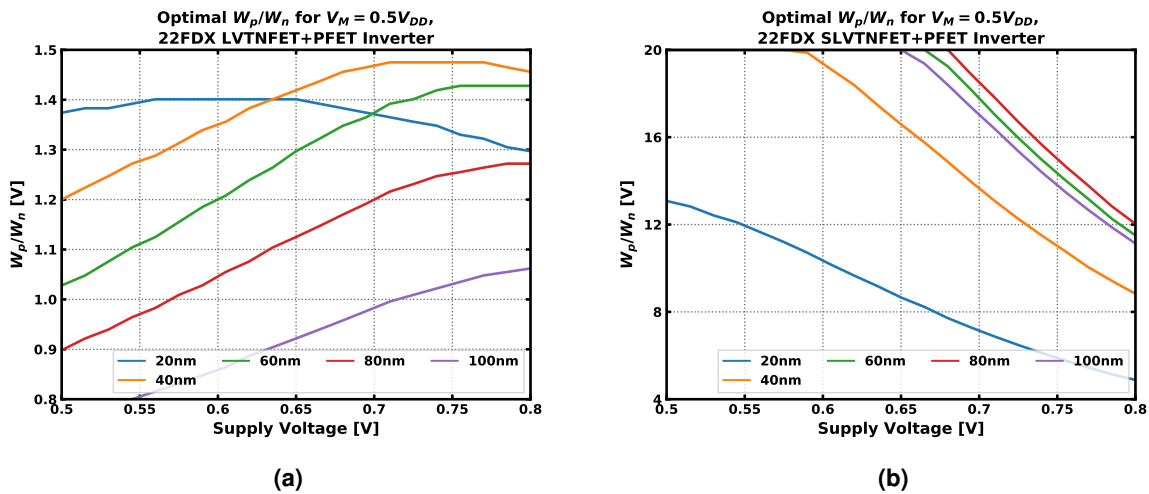


Figure 35: (a) Optimal width PFET/LVTNFET, (b) Optimal width PFET/SLVTNFET.

4.3.13 Tunable Frequency Backgate-Coupled Pseudodifferential Delay Cell

To implement the backgate-coupled pseudo-differential inverter delay cell topology with back-gate tuning, two candidate topologies have been devised. The first is the parallel configured topology of figure 36a, and the second is a telescopic configuration, shown in figure 36b. Tuning of the delay cells is done in accordance with figure 37, where the backgate voltages v_{bgp} and v_{bgn} change in a complementary fashion. Tuning for increased frequency results in greater V_{BS} biasing for both PMOS and NMOS, such that the threshold voltage in both devices increases, modulating the channel conductances to be lower, and thus increase frequency. These cells were devised with a priority to maintain overall symmetry, specifically in regards to rise and fall time behavior. Hajimiri's highly cited paper [29] on the effect of impulse injection on oscillator edges finds that it is favorable for an oscillator to have as symmetric rise and fall time in terms of phase noise. Specifically, it was found that higher symmetry of waveform in terms of rise and fall behavior results in a lower corner frequency for flicker noise, thus improving lower frequency phase noise components of an oscillator.

4. DESIGN

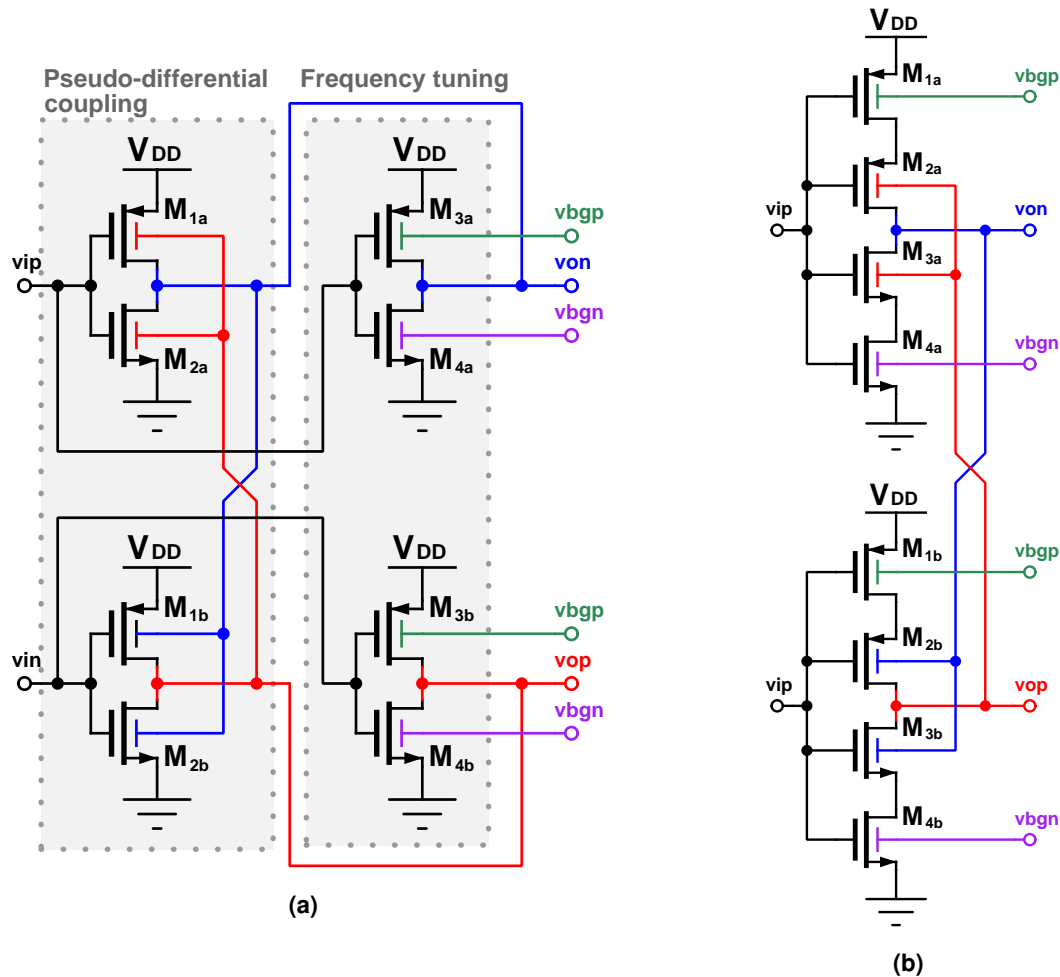


Figure 36: Backgate tunable backgate-coupled pseudodifferential delay cell in (a) Parallel, (b) Telescopic implementations.

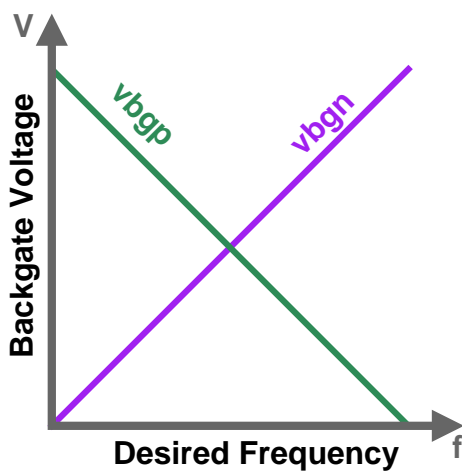


Figure 37: Complementary tuning of backgate voltages to achieve frequency tuning.

The parallel configured topology employs backgate-coupled pseudo-differential inverter in parallel with a second set of inverters, which the backgate voltages are set externally to control the oscillator frequency. The delay cell operates through superposition position of current, by connecting the inverters in parallel, their individual effects are combined to result in both fre-

quency tuning and differential operation. The frequency gain of this delay cell is controlled by setting a ratio of the device widths utilized in the cross-coupled inverter to the widths of the frequency tuning inverters. If this ratio is defined as $R = W_{1x}/W_{3x} = W_{2x}/W_{4x}$, the VCO gain is defined in equation 112. In a simulation case with 22FDX technology where LVTNFET + PFET devices, a nominal $(W/L) = 200\text{nm}/150\text{ nm}$ for all devices, and $R = 1$, a tuning range of 10% was observed in the ring oscillator. Changing $R = 2$ results in (resimulate this.. I lost the result...), corresponding to the prediction.

$$K'_{VCO,parallel} = \frac{K_{VCO}}{R + 1} \quad (112)$$

The telescopic topology is comprised of two sub-inverters each with a telescopic stack of four transistors. The header and footer transistor backgates are connected to external control voltages to adjust frequency. Modulating the control voltages will modulate the conductance of the header and footer devices, which result in a current-starving like behavior that modulate oscillator frequency. The inner pair of transistors in each sub-inverter are configured with a common backgate, which are cross-coupled with the output of the other respective sub-inverter, to induce differential operation in the same manner as the basic backgate-coupled pseudo-differential inverter delay cell. Frequency gain of the cell is controlled via setting the ratio of the inner transistors to the header and footer transistors. Due to the telescopic arrangement, a simple argument of current superposition as in the parallel case can not be made. Also, the model assumptions made in the backgate-controlled oscillator theory of section 4.3.3 are not necessarily valid, as the FET operating regime of the telescopic devices cannot be guaranteed to be in saturation during the delay cell propagation period. Rather than a full circuit analysis of this topology, an approximate result backed by simulated observation has been devised. If a ratio R is defined as $R = W_{1x}/W_{4x} = W_{2x}/W_{3x}$, it was determined via simulation that the oscillator frequency gain is reduced by $1/R$ for R near unity. Combining the two aforementioned observations results in equation 113. In a simulation case with 22FDX technology where LVTNFET + PFET devices, a nominal $(W/L) = 400\text{nm}/150\text{ nm}$ for all devices, and $R = 1$, a tuning range of 10% was observed in the ring oscillator. Changing $R = 2$ results in 4.8% tuning range.

$$K'_{VCO,telescopic} = \frac{K_{VCO}}{R} \quad (113)$$

These two topologies present different trade offs between frequency and achievable power. Inspecting equation 90, it is seen that oscillator power consumption is proportional to device (W/L) used in the delay cells. For low power, low effective (W/L) is desirable. In the case of the parallel delay stage, an effective $(W/L)'_{parallel}$ is arrived at by adding the device (W/L) 's of the cross-coupled and frequency tuning sub-inverters, yielding $(W/L)'_{parallel} = (1+R)(W/L)$. In the telescopic case, assuming $R=1$, it is observed that two FETs with size (W/L) cascaded have

4. DESIGN

an effective $(W/L)'_{tele} = 0.5(W/L)$. It is expected that minimum power attainable is achieved by utilizing the smallest available devices size in a technology, that is (W_{min}/L_{min}) , with $R=1$. Comparing the telescopic and parallel cases, it is seen that $(W/L)'_{parallel}/(W/L)'_{tele} = 4$, implying that the power consumption of the parallel stage can be presumed to be four times that of the series design with equal device sizes. In the case of this work, scaling of power is very important, and it has been found that the parallel topology was unable to achieve small enough K_{VCO} needed in this work with satisfactory power consumption. This is due to the need to increase R to reduce $K'_{VCO,parallel}$, which correspondingly increases power. Thus, a telescopic topology has been pursued in this work.

4.3.14 Final Delay Circuit

The final delay cell inverter topology employed in this work is shown in figure 38, which is the previous telescopic topology with a modification to enable fine and coarse tuning ranges. This modification is the addition of a second transistor to the header and footer of the telescopic stage. Transistors M_{1x} and M_{5x} implement medium granularity tuning, and transistors M_{2x} and M_{6x} implement fine granularity tuning. Defining $R = W_{1x}/W_{2x} = W_{5x}/W_{6x} > 1$, tuning the parameter R can be utilized to provide different tuning gains for the two ranges with respect to the applied backgate biases. This topology has been arrived at due to the finding that coupled with a CDAC fitting the area constraints of this work, it was not possible to achieve a satisfactorily wide tuning range with small enough K_{DCO} granularity with a single tuning range. For sizing of devices, it is recommended to select a channel length selected based on the findings for FOM_{jitter} versus channel length in section 4.3.2, picking the longest channel length possible. Then, the width of all devices (set equal) should be varied until the target power is achieved. Finally, the header and footer device widths should be varied until satisfactory K_{VCO} is found for the delay cell topology. Achieving design goals with this topology may require several iterations with layout.

4.3.15 Number of Ring Oscillator Stages

In the process of simulation, it has been determined that a two stage differential ring oscillator, generating in-phase and quadrature phase signals, will not oscillate. With a delay stage propagation time of t_{pd} , the cycle period is $1/f_{osc} = Nt_{pd}$, where in this case the number of stages $N = 2$. Every node is expected to switch two times per cycle, therefore it is determined that the switching period of a given node is $2t_{pd}$ for two stages. Previously, it has been determined that the propagation delay for the RC dominated ring oscillator is $\ln(2)\tau$, resulting in a switching period of $2\ln(2)\tau$. If switching from 0 to V_{DD} with exponential dependence, in a time period of $2\ln(2)\tau$, a change of $0.75V_{DD}$ is seen in voltage, implying that such a ring oscillator does not fully saturate to the rails, and therefore results in an extinction of oscillation as seen via

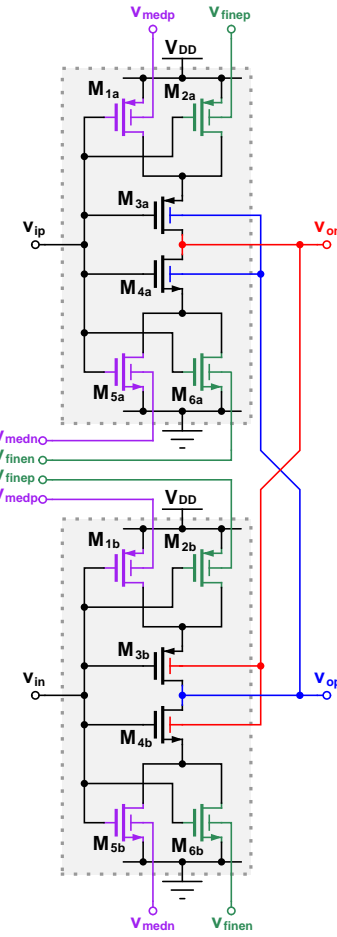


Figure 38: Pseudo-differential backgate-coupled inverter delay cell with fine and medium backgate-based tuning.

simulation. Originally, it was planned to implement a two-stage quadrature VCO at 2.448 GHz, however due to the infeasibility of this, alternative configurations were attempted. First was a 4-stage oscillator at 2.448 GHz was attempted, however, it was seen that it was not possible to achieve the desired power and phase noise requirements with the proposed telescopic backgate-coupled delay cell. Thus, another alternative, being a subharmonic oscillator operating at 1/3 of 2.448 GHz was considered. This was implemented as a 6-stage differential ring oscillator, as shown in figure 39, which oscillates at 816 MHz. With 6-stages, 12 oscillator phases can be derived, and it is possible to derive a quadrature 2.448 GHz sampling clock by combining with digital logic the different 816 MHz oscillator phases, as shown in figure 40. It was found to be feasible to implement an 816 MHz, 6-stage oscillator in 22FDX meeting power and phase noise requirements in the proposed topology.

4.3.16 Final Ring Oscillator Implementation

With a selection of inverter topology and number of delay cells, a final circuit topology for the ring oscillator has been devised. The oscillator is comprised of six basic delay cell elements shown in figure 41, which contains (1) a backgate-coupled and tunable pseudodifferential in-

4. DESIGN

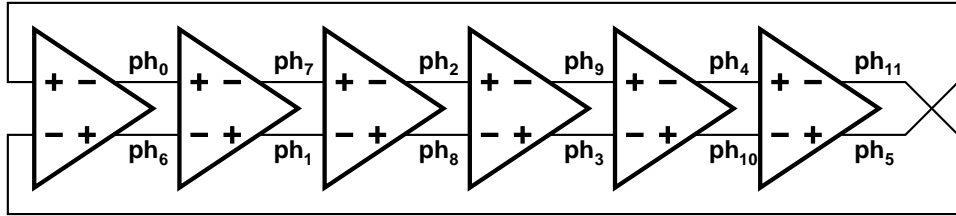


Figure 39: Basic differential ring oscillator circuit.

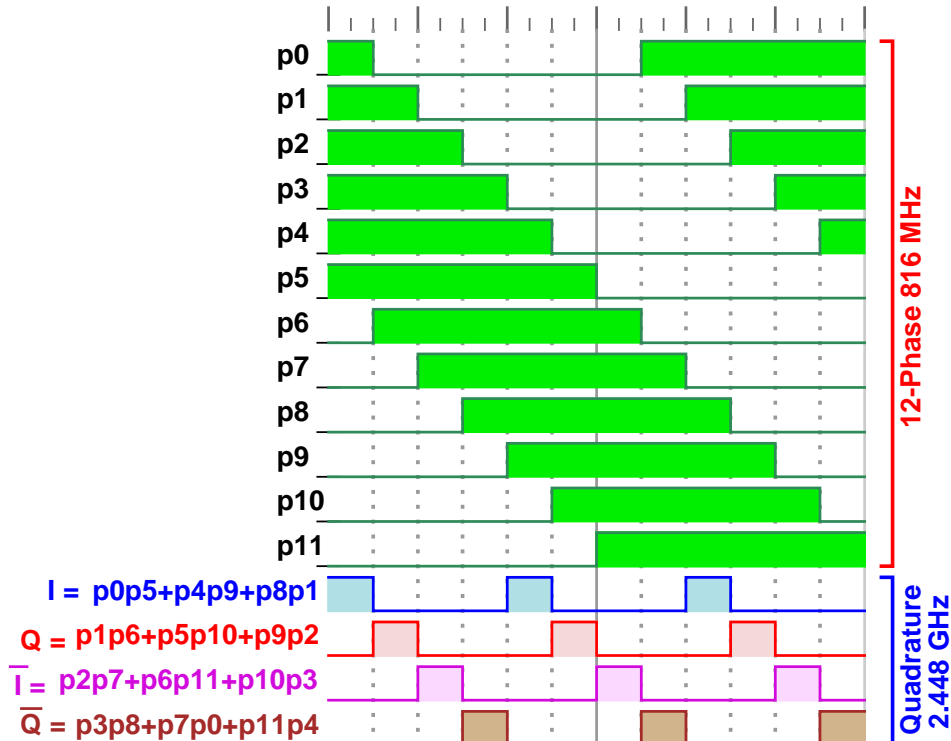


Figure 40: Third subharmonic to quadrature full rate conversion.

verter, (2) an adjustable capacitor bank, (3) reset switches, and (4), a buffer. A simplified symbol for the delay cell is shown in figure 42a, and the placement of the delay cells into a full ring oscillator is shown in figure 43. This delay cell was devised from the base inverter topology in order to obtain several goals. First of which, is the ability to adjust frequency for process, voltage and temperature variation. To achieve this, the adjustable capacitor bank is added to tune the oscillation frequency with greater range than achievable with the backgate tuning. The second goal is to be able to reset the oscillator to a known phase at start up, which is implemented via addition of switches at the output nodes which force the nodes to rail levels when a reset condition is asserted. This is such that when reset is de-asserted in tandem with a clock edge for the PLL, the initial edge of the oscillator sampled by a phase detector will be in sync with the clock, as shown in figure 42b. The third goal is to remove any effect of external noise and loading on the oscillator, for which a buffer has been added to each delay cell, that the external world connects to. Table 6 contains the devices sizes used to implement the delay cell of figure 41.

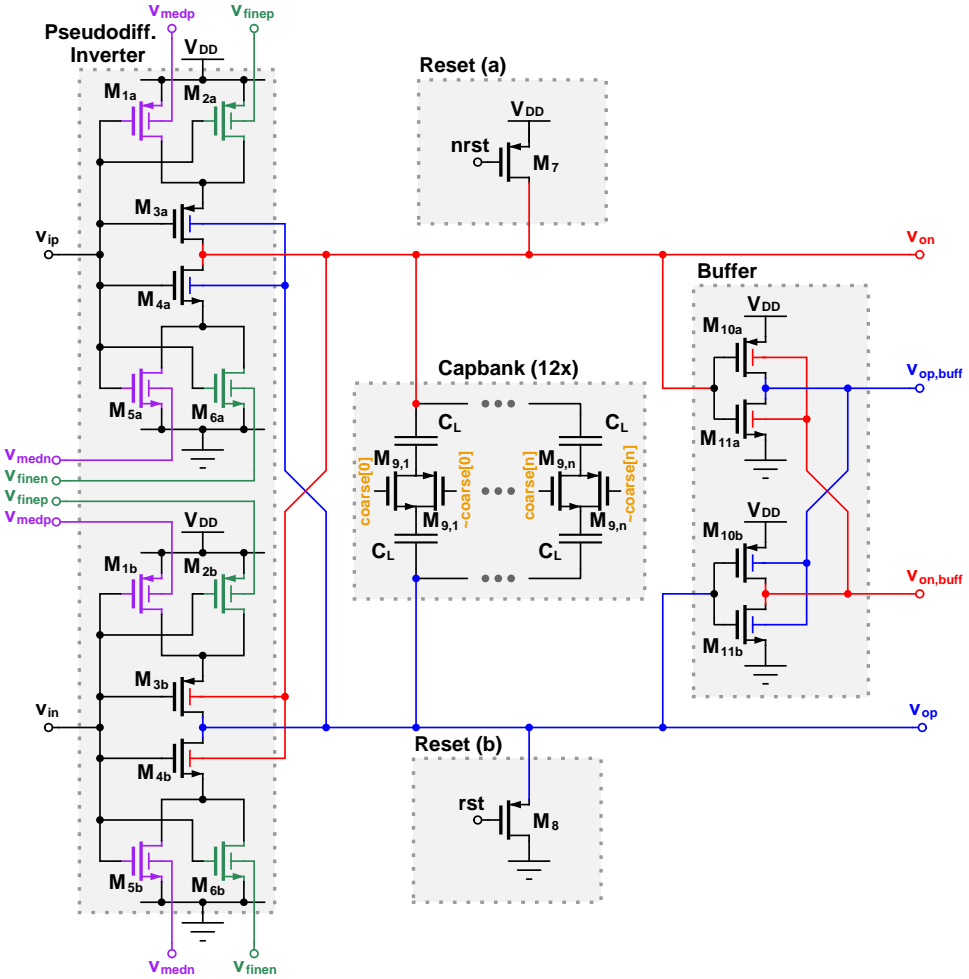


Figure 41: Ring oscillator delay cell full circuit.

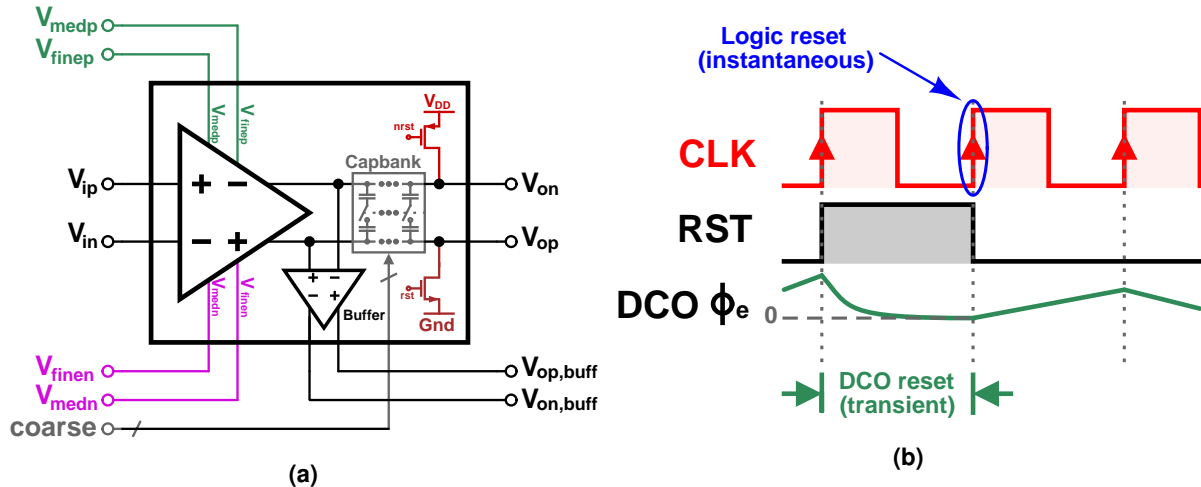


Figure 42: (a) Ring oscillator delay cell symbol, (b) DCO Reset scheme.

4.3.17 Layout

In order to implement a compact oscillator core, the delay cells were layed out as slices, for which several slices are abutted together to make a full ring oscillator. This is similar to the

4. DESIGN

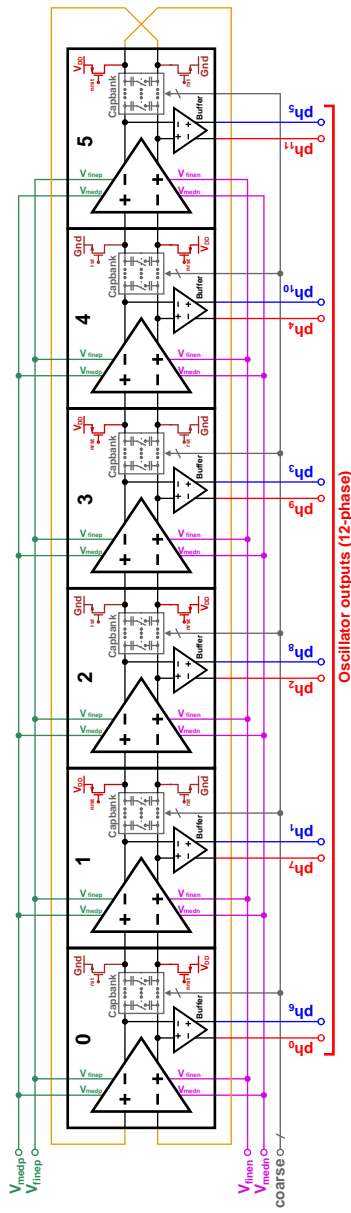


Figure 43: Ring oscillator full schematic.

Device	(W/L)
M_{1x}, M_{5x}	800n/40n
M_{2x}, M_{6x}	100n/40n
M_{3x}, M_{4x}	400n/40n
M_{7x}, M_{8x}	200n/20n
$M_{9,1}, \dots, M_{9,n}$	100n/20n
M_{10x}, M_{11x}	200n/20n
C_L	200 aF

Table 6: Delay Stage Device Sizes.

approach of utilizing bit slices in a processor to implement a many bit architecture. The unit delay cell slice is shown in figure 44, where there pseudodifferential inverter, capacitor bank, reset switch, and output buffer out place in a row, $3.5 \mu\text{m}$ tall by $10.85 \mu\text{m}$ wide. Supply voltages, the fine and medium control votages, capacitor switch signals, and reset signals run vertically from top to bottom edge, to allow for delay cell abuttment to form the ring oscillator. The full oscillator is shown in figure 45 (rotated 90 degrees), where the delay cells are placed out of order (4,3,5,2,6,1) to assist in making wire lengths between all cells approximately the same. A non out of order sequence (1,2,3,4,5,6) would result in short connections between all cells, except for between cells 1 and 6, which would result in unequal loading on stage 6, leading to a constant phase error for that stage.

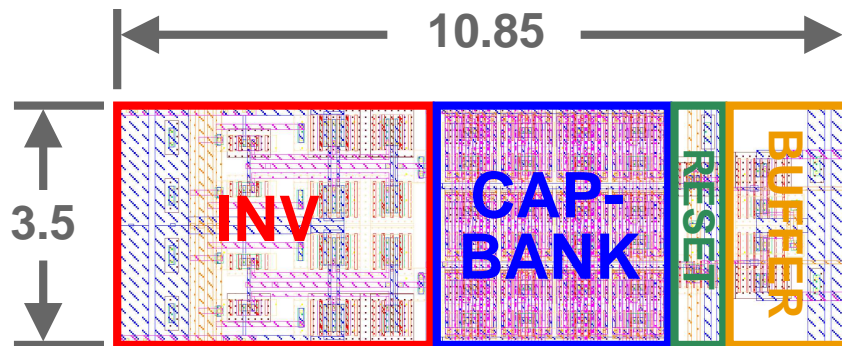


Figure 44: Delay cell slice layout (in microns).

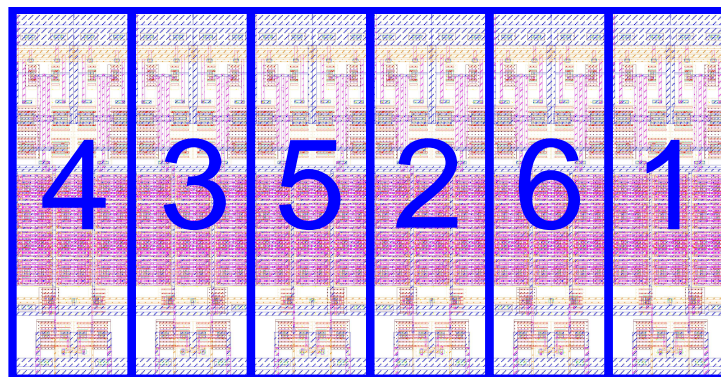


Figure 45: Delay cell arrangement in layout to result in similar wirelengths between stages.

Simulation results pertaining to the ring oscillator are found in results section 5.5, and the full set of layout images are in appendix A.1.

4.4 Loop Filter

For selection of a loop filter, some basic criteria have been selected for desirable synthesizer behavior:

- ① Zero steady state error, for accuracy of the synthesized frequency.
- ② Minimize complexity of implemented logic (i.e. minimize the number of loop filter poles and zeros).
- ③ Low pass response of PLL in closed-loop.

From this work author's previous findings [1], it was established that the pole-zero filter satisfying these requirements is a proportional-integral controller.

4.4.1 Proportional-integral Loop Filter

A proportional-integral controller [30] is given in equation 114, containing a proportional gain term K_p , and an integral gain term K_i . This can be optionally represented using a pole at zero and a zero with $\omega_z = K_i/K_p$:

$$H_{LF}(s) = K_p + \frac{K_i}{s} = \frac{K_i}{s} \left(\frac{s}{\omega_z} + 1 \right) \quad (114)$$

Substitution of this controller into the PLL closed loop transfer function (equation 64) results in:

$$T(s) = \frac{\Phi_{out}(s)}{\Phi_{ref}(s)} = \frac{2\pi K_{BBPD} K_{DCO} K_i \left(\frac{s}{\omega_z} + 1 \right)}{s^2 + 2\pi K_{BBPD} K_{DCO} K_i \left(\frac{s}{\omega_z} + 1 \right)} \quad (115)$$

4.4.2 Discretization of Loop Filter

Using the continuous filter discretization approach described in section 2.4.6 on the loop filter of equation 114 results in equation 116. When converting a continuous time PLL model into a discrete time controller implementation, a commonly cited rule of thumb in PLL literature states that the PLL loop bandwidth should be constrained as $BW_{loop} \leq 0.1 f_{ref}$ [31] (here $\Delta T_s = 1/f_{ref}$). This is due to the fact that low degrees of oversampling lead to deviations between continuous PLL models and real sampled-PLL performance, possibly causing instability or sub-optimal performance versus an intended design.

$$H_{LF}(z) = \frac{K_i}{s} \left(\frac{s}{\omega_z} + 1 \right) \Big|_{s=\frac{1}{\Delta T_s}(1-z^{-1})} = K_p \frac{(1 + \omega_z \Delta T_s) - z^{-1}}{1 - z^{-2}} \quad (116)$$

The transformation of equation 116 into a digitally implementable design as a direct form 1 IIR filter shown in figure 46. Its filter coefficients given by equations 117 and 118.

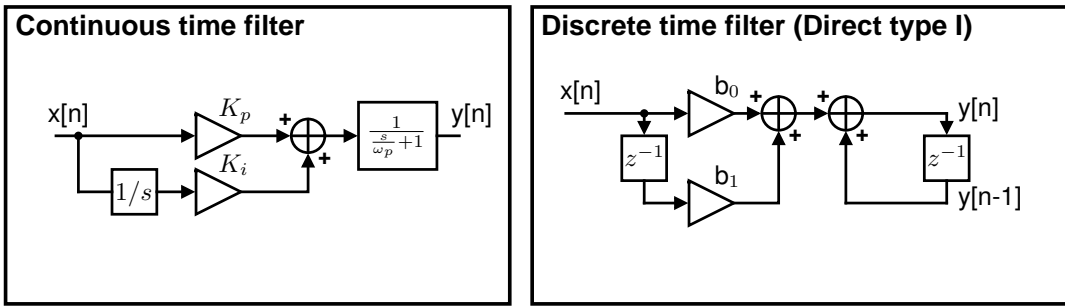


Figure 46: Implementation of filter.

$$b_0 = K_p(1 + \omega_z \Delta T_s) \quad (117)$$

$$b_1 = -K_p \quad (118)$$

4.4.3 Optimal Filter Selection (Noisy BBPD)

Optimization of a loop filter under BBPD operation will be performed by minimizing the total integrated phase noise power out of the PLL. First, some mathematical simplifications of the PLL model are introduced. Rewriting equation 115 with substitutions $\omega_z = K_i/K_p$ and $K = 2\pi K_{BBPD} K_{DCO} K_i$:

$$T(s) = \frac{\Phi_{out}(s)}{\Phi_{ref}(s)} = \frac{s \frac{K}{\omega_z} + K}{s^2 + s \frac{K}{\omega_z} + K} \quad (119)$$

The denominator can be redefined in terms of a natural frequency ω_n and damping ratio ζ :

$$s^2 + s \frac{K}{\omega_z} + K = s^2 + s 2\zeta \omega_n + \omega_n^2 \quad (120)$$

Thus, $\omega_n = \sqrt{K}$, and $\omega_z = \sqrt{K}/2\zeta$. The poles of equation 119 are then located at $s = \zeta\sqrt{K} \pm j\sqrt{K}\sqrt{1-\zeta^2}$. The time constant of the PLL is obtained from the real portion of the dominant pole in equation 119:

$$\tau = \frac{1}{|\min(\Re(\{s_{p1}, s_{p2}\}))|} \quad (121)$$

It is of interest to minimize settling time of the PLL (i.e. time constant), thus maximizing the frequency of the dominant pole of the PLL is of interest. In the pole-zero plot of figure 47, the dominant pole of equation 119 is observed to be maximized with $\zeta = 1$ (loci are oriented based on increasing ζ values). Citing Razavi [7], ζ is typically "chosen to be $> \sqrt{2}/2$ or even 1 to avoid excessive ringing." According it has been chosen to fix $\zeta = 1$ for the PI-controller.

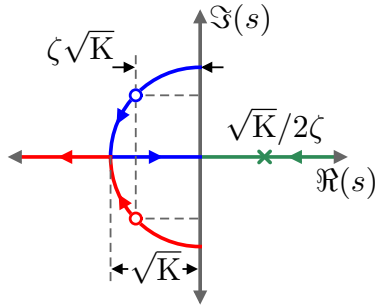


Figure 47: PI-controller PLL pole-zero locations.

With ζ is constrained to 1, the final simplified PLL closed loop transfer function is in equation 122. The form of this equation is favorable for integration, due to the selection of $\zeta=1$.

$$T(s) = \frac{2\sqrt{K}s + K}{s^2 + 2\sqrt{K}s + K} \quad (122)$$

Now, the PLL output referred noise power of the oscillator and BBPD may be calculated. First, if the PLL-less oscillator is defined as equation 123, where $S_{0_{osc}}$ is defined as the oscillator spectral density at 1 Hz frequency offset from the carrier. This takes the form of the theoretical limit for ring oscillator phase noise in section 2.5.4. This is based from a phase noise measurement of the oscillator $\mathcal{L}(f)$ at carrier offset f .

$$\mathcal{L}(f) = \frac{S_{0_{osc}}}{f^2} \quad \rightarrow \quad S_{0_{osc}} = \mathcal{L}(f)f^2 \quad (123)$$

The PLL output spectrum is then computed as:

$$S_{\Phi n_{DCO,out}}(f) = \mathcal{L}(f)|1 - T(f)|^2 = \frac{S_{0_{osc}}}{f^2}|1 - T(f)|^2 \quad (124)$$

Now, $|1 - T(f)|^2$ is found to be after much simplification:

$$|1 - T(f)|^2 = \frac{f^4}{\left(f^2 + \frac{K}{(2\pi)^2}\right)^2} \quad (125)$$

Thus, re-evaluating equation 124 yields:

$$S_{\Phi n_{DCO,out}}(f) = S_{0_{osc}} \frac{f^2}{\left(f^2 + \frac{K}{(2\pi)^2}\right)^2} \quad (126)$$

The total PLL phase noise power associated with the oscillator, $\sigma_{\Phi n_{DCO}}^2$ is achieved by integrat-

ing equation 126 with respect to frequency.

$$\sigma_{\Phi_{n,DCO}}^2 = \int_{-\infty}^{\infty} S_{\Phi_{n,DCO,out}}(f) df = S_{0_{osc}} \int_{-\infty}^{\infty} \frac{f^2}{\left(f^2 + \frac{K}{(2\pi)^2}\right)^2} df \quad (127)$$

$$= S_{0_{osc}} \frac{\pi^2}{\sqrt{K}} \quad (128)$$

Next, the total BBPD noise at the PLL output is computed. The expression for BBPD noise density in equation 72 will be used, and for which $|\mathbf{T}(f)|^2$ must be computed. This is:

$$|\mathbf{T}(f)|^2 = \frac{4 \frac{K}{(2\pi)^2} f^2 + \frac{K^2}{(2\pi)^4}}{\left(f^2 + \frac{K}{(2\pi)^2}\right)^2} \quad (129)$$

The resulting BBPD spectral density equation is:

$$S_{\Phi_{n,BBPD,out}}(f) = \frac{\frac{\pi}{2}(\sigma_{\phi_j}^2 + \sigma_{\phi_n}^2) - \sigma_{\phi_n}^2}{f_{ref}} |\mathbf{T}(f)|^2 \quad (130)$$

$$= \frac{\frac{\pi}{2}(\sigma_{\phi_j}^2 + \sigma_{\phi_n}^2) - \sigma_{\phi_n}^2}{f_{ref}} \cdot \frac{4 \frac{K}{(2\pi)^2} f^2 + \frac{K^2}{(2\pi)^4}}{\left(f^2 + \frac{K}{(2\pi)^2}\right)^2} \quad (131)$$

The total PLL phase noise power associated with the BBPD, $\sigma_{\Phi_{n,BBPD}}^2$ is achieved by integrating equation 130 with respect to frequency:

$$\sigma_{\Phi_{n,BBPD}}^2 = \frac{\frac{\pi}{2}(\sigma_{\phi_j}^2 + \sigma_{\phi_n}^2) - \sigma_{\phi_n}^2}{f_{ref}} \int_{-\infty}^{\infty} \frac{4 \frac{K}{(2\pi)^2} f^2 + \frac{K^2}{(2\pi)^4}}{\left(f^2 + \frac{K}{(2\pi)^2}\right)^2} df \quad (132)$$

$$= \frac{5\sqrt{K}}{4f_{ref}} \cdot \left[\frac{\pi}{2}(\sigma_{\phi_j}^2 + \sigma_{\phi_n}^2) - \sigma_{\phi_n}^2 \right] \quad (133)$$

The total noise out of the PLL is therefore the sum of $\sigma_{\Phi_{n,BBPD}}^2$ and $\sigma_{\Phi_{n,DCO}}^2$:

$$\sigma_{\phi_n}^2 = \sigma_{\Phi_{n,DCO}}^2 + \sigma_{\Phi_{n,BBPD}}^2 = S_{0_{osc}} \frac{\pi^2}{\sqrt{K}} + \frac{5\sqrt{K}}{4f_{ref}} \cdot \left[\frac{\pi}{2}(\sigma_{\phi_j}^2 + \sigma_{\phi_n}^2) - \sigma_{\phi_n}^2 \right] \quad (134)$$

Reorganization of equation 134 in terms of $\sigma_{\phi_n}^2$ yields:

$$\sigma_{\phi_n}^2 = \frac{S_{0_{osc}} \frac{\pi^2}{\sqrt{K}} + \frac{5\pi\sqrt{K}}{8f_{ref}} \sigma_{\phi_j}^2}{1 - \frac{5\sqrt{K}}{4f_{ref}} \left(\frac{\pi}{2} - 1 \right)} \quad (135)$$

In the presence of a non-ideal phase detector having phase noise power $\sigma_{\phi_j}^2 = (2\pi f_{osc})^2 \sigma_{t_j}^2$, the

4. DESIGN

optimal value K that minimizes phase noise is obtained as the root of $d\sigma_{\phi_n}^2/dK = 0$ in equation 136. The obtained result for K_{opt} may be substituted into equation 135 to determine the total noise power $\sigma_{\phi_n}^2$.

$$K_{opt} = \left[\frac{S_{0osc}\pi(\pi - 2)}{\sigma_{\phi_j}^2} - \sqrt{\frac{S_{0osc}^2\pi^2(\pi - 2)^2}{\sigma_{\phi_j}^4} + \frac{S_{0osc}8\pi f_{ref}}{5\sigma_{\phi_j}^2}} \right]^2 \quad (136)$$

The parameter of K has a direct relationship to the closed loop bandwidth BW_{loop} of the PLL, which is determined by solving $|T(f)|^2 = 0.5$. The result is given in equation 137.

$$BW_{loop} = \frac{1}{2\pi} \sqrt{K} \sqrt{3 + \sqrt{10}} \quad (137)$$

As mentioned before, it is advisable to observe a limit of loop bandwidth of at most $BW_{loop} = 0.1f_{ref}$. The coefficient α is defined here now to describe the loop bandwidth-reference frequency ratio, where $BW_{loop} = \alpha f_{ref}$. In the potential case that α must be constrained for sampling reasons, equation 138 is found to determine K. Thus with a 16 MHz reference, and $\alpha=0.1$, $K = 1.64 \times 10^{13}$.

$$K_\alpha = \frac{(2\pi\alpha f_{ref})^2}{3 + \sqrt{10}} \quad (138)$$

It is best to be as near to the optimal value of α as possible. Figure 48 demonstrates the effect of α on the phase noise power (normalized to the optimal value). It is seen that the total phase noise asymptotically grows to infinity as α approaches 0 and 0.55. In the case of $\alpha = 0.1$, the phase noise is expected to be 1.69 times the optimal value, resulting in a 2.3 dB degradation in phase noise power from optimal.

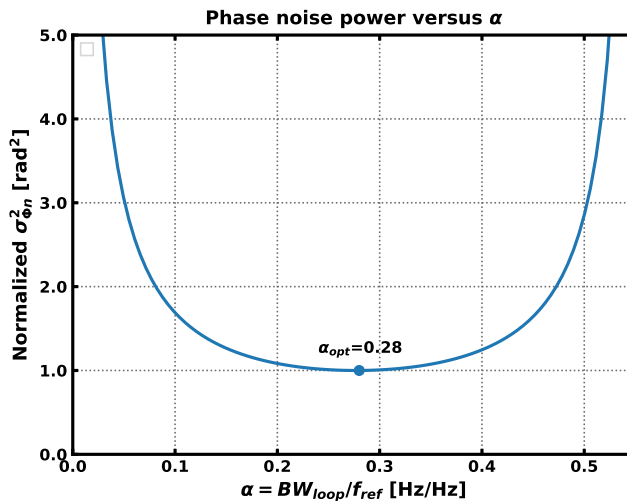


Figure 48: Phase noise power (normalized) versus α .

It is possible to derive a constraint for BBPD jitter $\sigma_{\phi_j}^2$ in terms of α and a target $\sigma_{\phi_n}^2$ (i.e. CNR

value), which allows for the performance specification for the physical BBPD to be set. Equation 139 defines the maximum allowable phase noise power due to BBPD jitter, and equation 140 defines the maximum RMS timing jitter of the same detector.

$$\sigma_{\phi_j}^2 \leq \sigma_{\phi_n}^2 \left[\frac{4\sqrt{3 + \sqrt{10}}}{5\pi^2\alpha} + \frac{2}{\pi} - 1 \right] - \frac{2S_{0osc}(3 + \sqrt{10})}{5\pi\alpha^2 f_{ref}} \quad (139)$$

$$\sigma_{t_j} \leq \frac{\sigma_{\phi_n}}{2\pi f_{osc}} \sqrt{\left[\frac{4\sqrt{3 + \sqrt{10}}}{5\pi^2\alpha} + \frac{2}{\pi} - 1 \right] - \frac{2S_{0osc}(3 + \sqrt{10})}{5\pi\alpha^2 f_{ref}}} \quad (140)$$

Now with theory in place to optimize PLL performance, mapping of the optimal parameter K onto the loop filter of equation 114 will be considered. Recall that $\omega_z = K_i/K_p = \sqrt{K}/2\zeta$ and $K = 2\pi K_{BBPD} K_{DCO} K_i$. The parameters K_i , K_p , and ω_z are thus provided in equations 141-143.

$$\omega_z = \frac{\sqrt{K}}{2} \quad (141)$$

$$K_p = \frac{\sqrt{K}}{\pi K_{BBPD} K_{DCO}} = \frac{\sqrt{K} \sqrt{\sigma_{\phi_j}^2 + \sigma_{\phi_n}^2}}{\sqrt{2\pi} K_{DCO}} \quad (142)$$

$$K_i = \frac{K}{2\pi K_{BBPD} K_{DCO}} = \frac{K \sqrt{\sigma_{\phi_j}^2 + \sigma_{\phi_n}^2}}{2\sqrt{2\pi} K_{DCO}} \quad (143)$$

Converting the filter design into discrete time equivalent results in equations 144 and 145

$$b_0 = \frac{\sqrt{K} \sqrt{\sigma_{\phi_j}^2 + \sigma_{\phi_n}^2}}{\sqrt{2\pi} K_{DCO}} \left(1 + \frac{\sqrt{K}}{2f_{ref}} \right) \quad (144)$$

$$b_1 = -\frac{\sqrt{K} \sqrt{\sigma_{\phi_j}^2 + \sigma_{\phi_n}^2}}{\sqrt{2\pi} K_{DCO}} \quad (145)$$

If design of the PLL is with fixed target for $\sigma_{\phi_n}^2$ (CNR), has a known $\sigma_{\phi_j}^2$ for the BBPD, and α is selected to be constant (i.e. 0.1), the filter coefficients may be calculated as in equations 146 and 147.

$$b_0 = \frac{\alpha f_{ref} \sqrt{2\pi} \sqrt{\sigma_{\phi_j}^2 + \sigma_{\phi_n}^2}}{\sqrt{3 + \sqrt{10}} K_{DCO}} \left(1 + \frac{\pi\alpha}{\sqrt{3 + \sqrt{10}}} \right) \quad (146)$$

$$b_1 = -\frac{\alpha f_{ref} \sqrt{2\pi} \sqrt{\sigma_{\phi_j}^2 + \sigma_{\phi_n}^2}}{\sqrt{3 + \sqrt{10}} K_{DCO}} \quad (147)$$

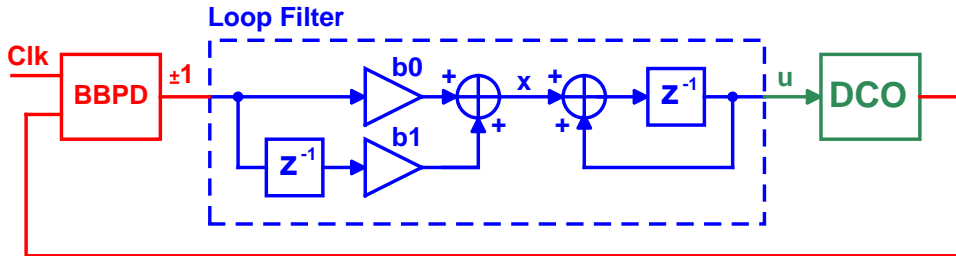


Figure 49: Simplified model of BBPD-PLL

4.4.4 Emergent Bang-Bang PLL Phase Noise

Since the output of BBPD is quantized to ± 1 , the use of a PI loop filter architecture results in only 4 possible values that node x can be valued as shown in the simplified BBPD-PLL model of figure 49. These are $[b_0 + b_1]$, $[b_0 - b_1]$, $[-b_0 + b_1]$, $[-b_0 - b_1]$. The result of this is the loop filter output u must increment by one of these four values every reference cycle.

The worst case scenario of this is the BBPD outputting an alternating sequence of $+1/-1/+1/-1\dots$, for which the output will toggle by increments $[b_0 - b_1]$ and $[-b_0 + b_1]$. In terms of frequency, the output will shift up and down by $K_{DCO}[b_0 - b_1]$ and $[-b_0 + b_1]$ every other cycle, which can be substantial depending on the product of those factors. In the phase domain, this results in a cyclostationary triangle-wave like phase trajectory (ignoring other sources of phase noise), as shown in figure 50a. The worst case increment in phase per cycle is given in equation 148. In the frequency domain, this cyclostationary behavior can result in spurs, as shown in figure 50b. When phase noise from other processes in the PLL are large enough that they dwarf the worst case cyclostationary behavior, it is expected that output of the BBPD will be stochastically scrambled and the cyclostationary effects will be subsided.

$$\Delta\Phi = \frac{2\pi|b_0 - b_1|K_{DCO}}{f_{ref}} \quad (148)$$

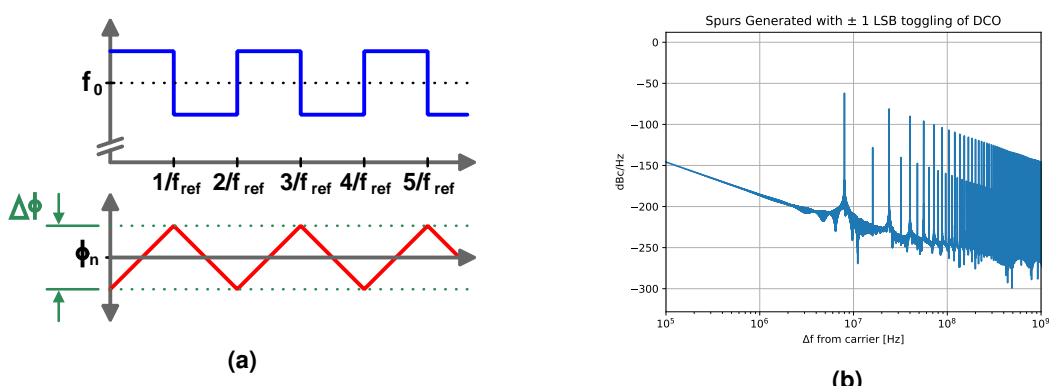


Figure 50: (a) Worst case cyclostationary behavior of BBPD-PLL, (b) Resulting in spurs from worst case cyclostationary behavior.

Even if cyclostationary effects are avoided, the quantization of the loop filter output to increments of the four aforementioned values results in an additive phase noise contribution to the PLL. These increments result in a forced deterministic change in output phase error in every reference interval. The RMS contribution of phase noise to the PLL output due to the quantized steps in frequency from bang-bang operation has the relationship given in equation 149. This phase noise component will be termed "emergent bang-bang phase noise", represented by $\sigma_{\Phi_{nem}}$. Later, proportionality of the phase noise to $|b_0 - b_1|$ will be shown through simulation. Thus, adding a factor of proportionality β_1 results in equation 150. Optimization of the PLL with inclusion of emergent bang-bang phase noise contributions will now be considered.

$$\sigma_{\Phi_{nem}} \approx \frac{\pi|b_0 - b_1|K_{DCO}}{f_{ref}} \quad (149)$$

$$\sigma_{\Phi_{nem}} = \beta_1 \frac{\pi|b_0 - b_1|K_{DCO}}{f_{ref}} \quad (150)$$

If α is used to describe the loop bandwidth-reference frequency ratio, the quantity $|b_0 - b_1|$ is provided in equation 151. It will be shown that α is a constant under optimal conditions, so the optimized $|b_0 - b_1| = 2\beta_2|b_1|$, where β_2 is a constant proportionality factor. Lumping proportionality constants together, we define $\beta = \beta_1\beta_2$, thus $\sigma_{\Phi_{nem}}$ is defined in equation 152.

$$|b_0 - b_1| = \left(2 + \frac{\pi\alpha}{\sqrt{3 + \sqrt{10}}}\right) |b_1| = 2\beta_2|b_1| \quad (151)$$

$$\sigma_{\Phi_{nem}} = \frac{2\pi\beta|b_1|K_{DCO}}{f_{ref}} \quad (152)$$

Including $\sigma_{\Phi_{nem}}^2$, BBPD noise and oscillator noise, the total phase noise $\sigma_{\Phi_n}^2$ out of the PLL is in equation 153.

$$\sigma_{\Phi_n}^2 = \sigma_{\Phi_{n,DCO}}^2 + \sigma_{\Phi_{n,BBPD}}^2 + \sigma_{\Phi_{nem}}^2 = S_{0_{osc}} \frac{\pi^2}{\sqrt{K}} + \sigma_{\phi_n}^2 \frac{5\sqrt{K}}{4f_{ref}} \cdot \left(\frac{\pi}{2} - 1\right) + \sigma_{\Phi_{nem}}^2 \quad (153)$$

Redefining equation 145 using equation 153 as the phase noise power results in equation 154.

$$b_1 = -\frac{\sqrt{K} \sqrt{\sigma_{\Phi_{n,em}}^2 + \sigma_{\Phi_{n,DCO}}^2 + \sigma_{\Phi_{n,BBPD}}^2}}{\sqrt{2\pi} K_{DCO}} \quad (154)$$

$$= -\frac{\sqrt{K} \sqrt{\sigma_{\Phi_{nem}}^2 + S_{0_{osc}} \frac{\pi^2}{\sqrt{K}} + \sigma_{\phi_n}^2 \frac{5\sqrt{K}}{4f_{ref}} \left(\frac{\pi}{2} - 1\right)}}{\sqrt{2\pi} K_{DCO}} \quad (155)$$

A resulting expression for $\sigma_{\Phi_{nem}}^2$ is obtained by solving the system of equations given by 152 and 154 is equation 156. Redefining K in terms of α as defined by equation 138 results in the

4. DESIGN

latter portion of the equation.

$$\sigma_{\Phi_n}^2 = \frac{S_{0_{osc}} \frac{\pi^2}{\sqrt{K}}}{1 + \frac{2\pi K \beta^2}{f_{ref}^2} - \frac{5\sqrt{K}}{4f_{ref}} \left(\frac{\pi}{2} - 1\right)} = \frac{\frac{\pi S_{0_{osc}} \sqrt{3+\sqrt{10}}}{2f_{ref}}}{\alpha - \alpha^2 \frac{5\pi}{2\sqrt{3+\sqrt{10}}} \left(\frac{\pi}{2} - 1\right) - \alpha^3 \frac{8\pi^3 \beta^2}{3+\sqrt{10}}} \quad (156)$$

To minimize total phase noise power, $d\sigma_{\Phi_n}^2/d\alpha = 0$ is solved for, to yield the expression in equation 157 for optimal value of α .

$$\alpha_{opt} = -\frac{5\sqrt{3+\sqrt{10}}}{48\pi^2 \beta^2} + \frac{1}{2} \sqrt{\frac{25(3+\sqrt{10})}{24^2 \pi^4 \beta^4} \left(\frac{\pi}{2} - 1\right)^2 + \frac{3+\sqrt{10}}{6\pi^3 \beta^2}} \quad (157)$$

$$K_{opt} = \frac{(2\pi\alpha_{opt} f_{ref})^2}{3 + \sqrt{10}} \quad (158)$$

Computation of the value of constant β is not straightforward, so it has been solved numerically through discrete time simulation of a PLL with BBPD and PI-controller. It has been determined that at the optimum, $\beta = 1.0088433$ and accordingly $\alpha_{opt} = 0.07669725$. Furthermore, $\beta_1 = 0.919552$ and $\beta_2 = 1.097068$. These values were observed to be independent of PLL frequency, oscillator phase noise and reference and DCO gain. An example case of this simulation is shown in figure 51a, where the ratio β_1 of equation 150 is seen with the vertical lines. Figure 51b shows the effect of α versus total integrated phase noise power. Phase noise grows asymptotically with $\alpha = 0$ and $\alpha = 0.136$.

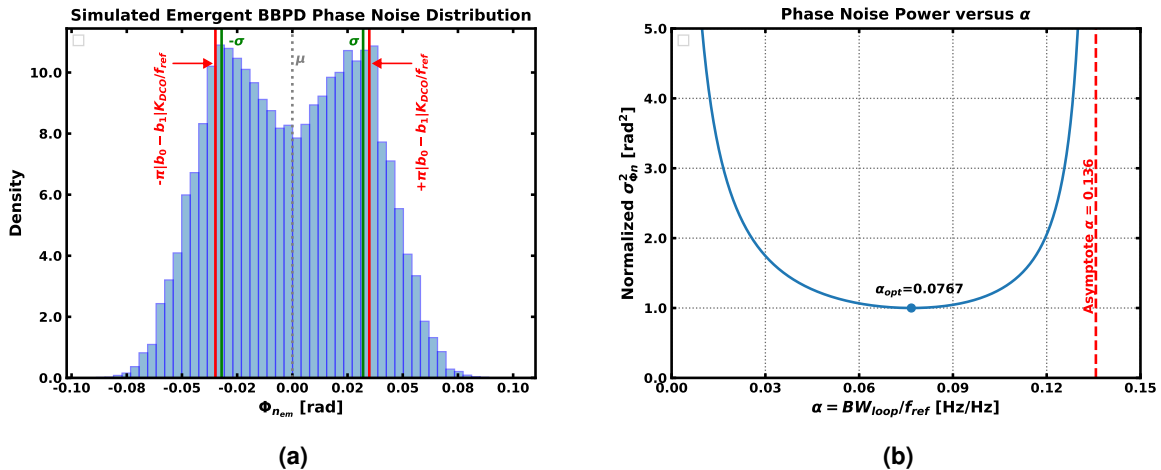


Figure 51: (a) Simulated emergent bang bang phase noise component of PLL phase noise, (b) Total output phase noise (normalized) versus α .

Application of the determined optimal parameters into equation 156 results in equation 159.

$$\sigma_{\Phi_n}^2 \Big|_{\alpha_{opt}} = 81.9353 \cdot \frac{S_{0_{osc}}}{f_{ref}} = 81.9353 \cdot \frac{\mathcal{L}_{osc}(f) f^2}{f_{ref}} \text{ [rad}^2\text{]} \quad (159)$$

Computed discrete time filter coefficients for this optimization case are provided in equations

160 and 162.

$$b_0 = \frac{\alpha_{opt} \sqrt{81.9353 \cdot 2\pi S_{0osc} f_{ref}}}{K_{DCO} \sqrt{3 + \sqrt{10}}} \left(1 + \frac{\pi \alpha_{opt}}{\sqrt{3 + \sqrt{10}}} \right) \quad (160)$$

$$= 0.769071 \frac{\sqrt{S_{0osc} f_{ref}}}{K_{DCO}} \left(1 + \frac{\pi \alpha_{opt}}{\sqrt{3 + \sqrt{10}}} \right) \quad (161)$$

$$b_1 = -\frac{\alpha_{opt} \sqrt{81.9353 \cdot 2\pi S_{0osc} f_{ref}}}{K_{DCO} \sqrt{3 + \sqrt{10}}} \quad (162)$$

$$= 0.701027 \frac{\sqrt{S_{0osc} f_{ref}}}{K_{DCO}} \quad (163)$$

4.4.5 Choice of Optimization Strategy

Depending on the implementation, the noise contributions from the phase detector jitter may exceed the emergent bang bang phase noise components. This may be the case in high frequency PLLs, e.g. mm-wave PLLs, where cycle periods are short. For 2.4 GHz operation in 22FDX, this poses less of a problem. The theory of section 4.4.4 ignores detector jitter while considering emergent effects, and section 4.4.3 ignores emergent behavior, while considering BBPD jitter. The recommended strategy therefore to calculate the optimal filter design using both theories, and select the one that results in a larger total phase noise value $\sigma_{\Phi_n}^2$, as that will be the dominant noise mode.

In this work, $80\mu\text{W}$ oscillator power at 2.448 GHz, 16 MHz reference, and 300K ambient temperature, $K_{DCO} = 4.2 \text{ kHz/LSB}$, oscillator noise density at 1 Hz of $\mathcal{L}(f)|_{f=1} = 11885 \text{ rad}^2/\text{Hz}$, and a detector jitter of 1.4 ps RMS, leads to a CNR of 17.2 dB when optimizing for oscillator plus jitter-inclusive BBPD noise, and a CNR of 12.2 dB when optimizing for oscillator noise plus emergent bang bang phase noise and jitterless detector noise. Selecting the worse valued result as the accurate model for this implementation then implies that this work should be optimized with the later model.

The final optimized filter parameters for the design of this work are in results section 5.9.

4.4.6 Filter Design for Synchronous counter

As gear-switching is intended to be used in this work, a separate loop filter will be calculated that is optimized for settling time (i.e. lock time) with the synchronous counter phase detector during initial start up. It was determined in the previous section that the poles of the PI-PLL occur at $s = \zeta\sqrt{K} \pm j\sqrt{K}\sqrt{1 - \zeta^2}$, as a conjugate pair. Taking the real portion (same for both)

4. DESIGN

provides for the value of the PLL time constant:

$$\tau = \frac{1}{|\min(\Re(\{s_{p1}, s_{p2}\}))|} = \frac{1}{\zeta\sqrt{K}} \quad (164)$$

If δ is considered the fraction of the initial frequency error during the lock process that may be described as being in-lock, then the PLL lock time is given by equation 165. δ can be also stated in terms of initial frequency error Δf , and the frequency tolerance from steady state f_{tol} that is considered to be in lock for a given application.

$$t_s = \frac{-\ln(\delta)}{\zeta\sqrt{K}} = \frac{-\ln\left(\frac{f_{tol}}{|\Delta f|}\right)}{\zeta\sqrt{K}} \quad (165)$$

It is observed that lock time is decreased by increasing the value of both ζ and K . Again, the constraint $\zeta=1$ is used due to its favorable characteristics. Thus, it is of interest here to maximize the value of K . It is seen that in equation 137 that $K \propto BW_{loop}^2$, thus loop bandwidth should be maximized. Again defining a constraint between loop bandwidth and reference frequency of $\alpha = BW_{loop}/f_{ref}$, equation 138 can be used to determine the optimal selection of K for a given α and f_{ref} . Plugging this into equation 165 yields equation 166.

$$t_s = \frac{-\sqrt{3 + \sqrt{10}} \ln\left(\frac{f_{tol}}{|\Delta f|}\right)}{2\pi\alpha f_{ref}} \quad (166)$$

Now, these defined filters parameters will be translated into a filter design. Again, the definitions $K = 2\pi K_{PD} K_{DCO} K_i$ and $\omega_z = K_i/K_p$ are used. A detector gain K_{PD} must be defined first for the synchronous counter. Since the synchronous counter counts cycles, it in effect converts 2π of phase into an increment of count of 1. Thus the gain is:

$$K_{PD} = \frac{1}{2\pi} \quad (167)$$

The parameters K_i , K_p and ω_z are then solved for, to result in equations 168 to 172.

$$K_p = \frac{4\pi\alpha f_{ref}}{\sqrt{3 + \sqrt{10}} K_{DCO}} \quad (168)$$

$$K_i = \frac{(2\pi\alpha f_{ref})^2}{(3 + \sqrt{10}) K_{DCO}} \quad (169)$$

$$\omega_z = \frac{\pi\alpha f_{ref}}{\sqrt{3 + \sqrt{10}}} \quad (170)$$

$$b_0 = K_p = \frac{4\pi\alpha f_{ref}}{\sqrt{3 + \sqrt{10}} K_{DCO}} \quad (171)$$

$$b_1 = \frac{4\pi\alpha f_{ref}}{\sqrt{3 + \sqrt{10}} K_{DCO}} \left(1 + \frac{\pi\alpha}{\sqrt{3 + \sqrt{10}}} \right) \quad (172)$$

$$(173)$$

4.4.7 PI-controller phase margin

The PI-PLL architecture of this work has a phase margin determined by the damping ratio ζ , given by equation 174. Figure 52 shows phase margin versus $0 \geq \zeta \geq 1$ of the PI-controller PLL. It is recommended to use at least 30-60 degrees in phase margin to achieve stability [32]. In this work, $\zeta = 1$ has been used, so a phase margin of 76 degrees is expected, and accordingly stability should be expected.

$$\angle L(\omega_{ug}) = \frac{180}{2\pi} \arctan \left(2\zeta \sqrt{2\zeta^2 + \sqrt{4\zeta^4 + 1}} \right) \quad [\text{degrees}] \quad (174)$$

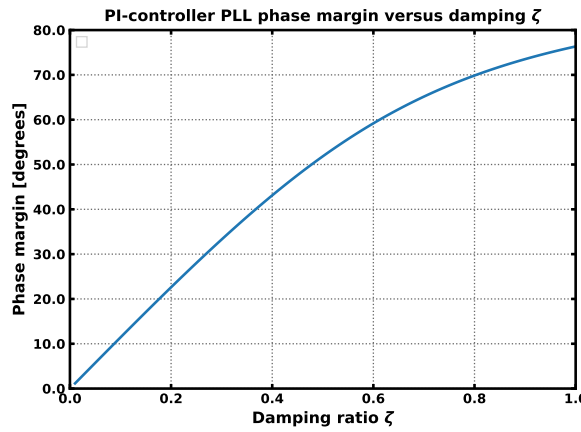


Figure 52: PI-controller PLL phase margin versus damping ratio.

4.4.8 Loop Filter Implementation

The loop filter has been chosen to be implemented with separate portions to construct the feed-forward paths for each phase detector of the PI-controller, but with a common integrator at the output, as shown in figure 53. This approach is intended to reduce dynamic power in steady state operation (using the BBPD). The rationale is that the synchronous counter is a linear detector, thus requires multipliers in the datapath to implement the filter, whereas the BBPD only outputs two values (+1 and -1), so the multipliers can be replaced with multiplexers that select between two sets of possible products ($\pm b_0$ and $\pm b_1$) depending on the input. It is lower energy to operate a multiplexer than an array multiplier due to substantially lower complexity of logic, so in steady state BBPD operation, substantial power savings will be seen. The usage of a common integrator at the output for both detector modes allows for seamless continuity of output value during transition between detector modes.

The computed filter coefficients $\{b_0, b_1\}$ for the PLL must be digitized into finite length signed two's complement words. A two's complement data word contains one sign bit, and variable

4. DESIGN

number of bits representing the integer and fractional portions of the encoded number. The author of this work has previously devised a method [1] for automatically computing the number of bits required to represent a filter in PLL. First, the selection of number of integer bits `int_bits` is determined by considering the integer part of the discrete filter coefficients. If the integer portions of the filter coefficients $\{b_0, b_1\}$ are divided into positive and negative valued sets `pos_ints` and `neg_ints`, the total integer bits required is therefore given in equation 177. Computation of the fractional portion is more complicated, and is based on reducing the quantization noise floor of the loop filter below other noise components of the PLL. The PLL design framework from [1] will be used in this work for determining the minimum digitized representation size of filter coefficients.

$$\text{pos_int_bits} = \lceil \log_2 (\max (|\text{pos_ints}|)) \rceil + 1 \quad (175)$$

$$\text{neg_int_bits} = \lceil \log_2 (\max (|\text{neg_ints}|)) \rceil \quad (176)$$

$$\text{int_bits} = \max(\{\text{pos_int_bits}, \text{neg_int_bits}\}) \quad (177)$$

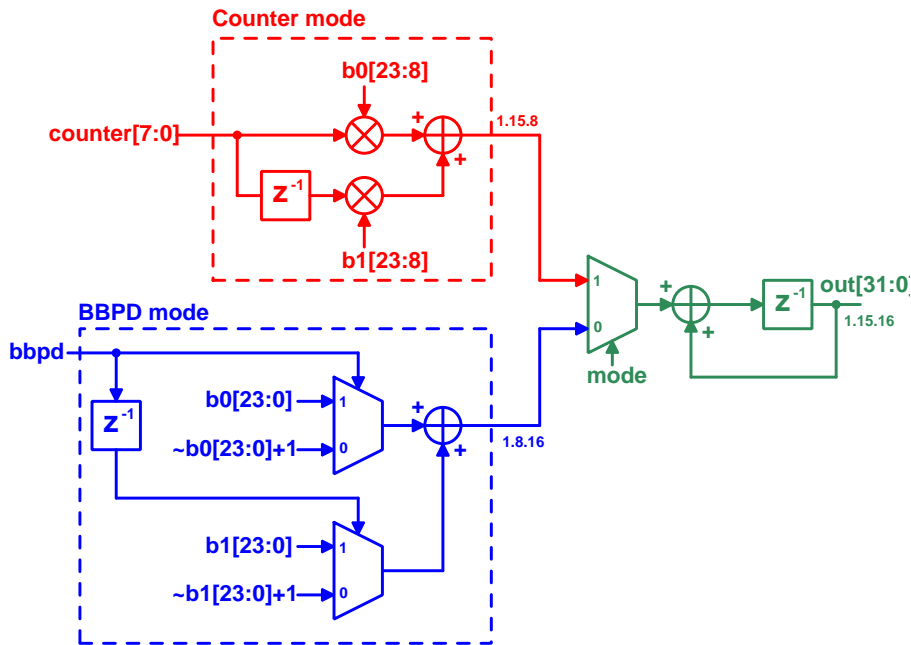


Figure 53: PI-controller implementation for combination of BBPD and synchronous counter usage.

need to fix this figure

4.5 CDAC - Fine Range

The required DAC resolution for using a VCO as a DCO may be analyzed in terms of the smallest possible change of the output of the loop filter. In 4.4.4, it was found that the possible increments for the loop filter are $|b_0 + b_1|$, $|b_0 - b_1|$, $|-b_0 + b_1|$, $|-b_0 - b_1|$. Evaluating these different possibilities, it is determined that the smallest magnitude occurs with $|b_0 + b_1|$. This

should be atleast be unity, corresponding to one LSB change of the DAC, to avoid quantizing this increment to zero. Using equations 144, 145, and $|b_0 + b_1| \geq 1$ results in in equation 178.

$$|b_0 + b_1| = \frac{\sqrt{K}}{2f_{ref}} \geq 1 \quad (178)$$

Applying this to the filter coefficients in the case of the bang-bang emergent phase noise optimized case, equations 160 and 162, results in the constraint for K_{DCO} in equations 179 and 180.

$$|b_0 + b_1| = \frac{\pi\alpha_{opt}^2 \sqrt{81.9353 \cdot 2\pi S_{0osc} f_{ref}}}{K_{DCO}(3 + \sqrt{10})} = 0.0680446 \cdot \frac{\sqrt{S_{0osc} f_{ref}}}{K_{DCO}} \geq 1 \quad (179)$$

$$K_{DCO} \leq 0.0680446 \cdot \sqrt{S_{0osc} f_{ref}} \quad (180)$$

With a reference level of V_{DD} , a voltage gain of the ring oscillator of K_{VCO} [Hz/V], and N bits in the CDAC, the DCO gain K_{DCO} is given in equation 181.

$$K_{DCO} = \frac{V_{DD} K_{VCO}}{2^N} \quad (181)$$

Combining 180 and 181 result in an expression for minimum number of DAC bits (using rail to rail reference levels), given in equation 182

$$N_{min} = \left\lceil \log_2 \left(\frac{V_{DD} K_{VCO}}{0.0680446 \sqrt{S_{0osc} f_{ref}}} \right) \right\rceil \quad (182)$$

Using the values $S_{0osc} = 11885$ and $K_{VCO} = 5.378$ kHz/mV obtained from phase noise simulation of the oscillator, $f_{ref} = 16$ MHz, $V_{DD} = 0.8$, the minimum number of bits is $N_{min} = 8$ bits. It has been decided therefore that to add a factor of safety, a 10 bit CDAC for fine tuning will be implmented. Higher resolution results in lower quantization noise added into the system by the DAC.

4.5.1 Circuit

It was attempted to maximize capacitance for a 10 bit DAC in an area constrained to $50 \mu\text{m} \times 15 \mu\text{m}$ (arrived at from the target PLL floor plan). MOM capacitors with 2.185 fF per unit were achieved with a unit cell of dimension $3\mu\text{m} \times 200$ nm, using 5 metal layers (C1-C5) to form the capacitor. The total capacitance is 2.24 pF, and the implementation area is $52 \mu\text{m} \times 16 \mu\text{m}$. The simulation results for this CDAC are in results section 5.6, and the layout in appendix A.2.

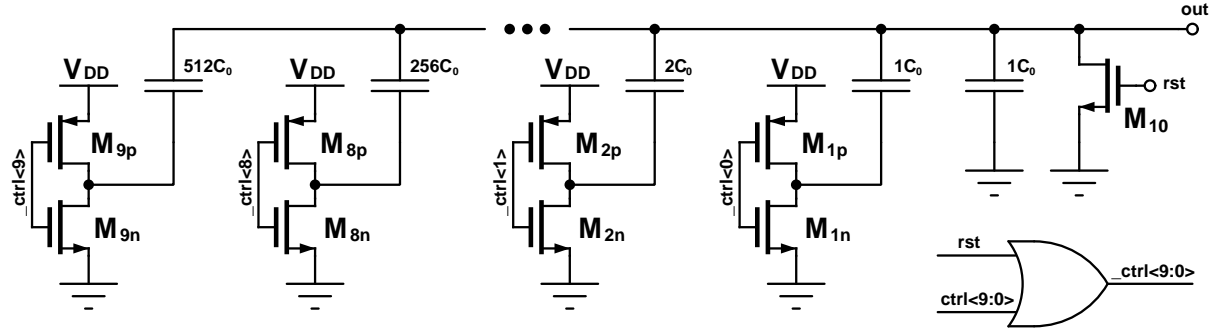


Figure 54: 10b CDAC.

4.6 CDAC - Medium Range

Selection of the medium tuning range DAC resolution has been coordinated with the fine range to provide continuity of tuning. Both tuning ranges are operated in steady state mode from the loop filter output, where if the fine CDAC is N_{fine} bits, and the medium CDAD is N_{med} bits, the fine CDAC is connected to the lowest N_{fine} bits of the loop filter output, and the medium DAC is connected to the next N_{med} bits. The K_{DCO} granularity of the medium range LSB must be larger than that of the MSB for the fine range, but smaller than that total range of the fine range. The inequality in equation 183 determines the range of bits which those criteria are satisfied.

$$\log_2 \left(\frac{K_{VCO,med}}{K_{VCO,fine}} \right) \leq N \leq \log_2 \left(\frac{2K_{VCO,med}}{K_{VCO,fine}} \right) \quad (183)$$

For the implemented oscillator, $K_{VCO,med} = 30.92$ kHz/mV, and $K_{VCO,fine} = 5.378$ kHz/mV. Thus the acceptable range of bits is $2.52 \leq N \leq 3.52$. Therefore, the number of bits for the medium DAC is 3 bits.

4.6.1 Circuit

The unit capacitance used is 249 fF/cap, yielding 2pF total capacitance. The size of the unit capacitor was selected to make the total capacitance near that of the 10b CDAC. The simulation results for this CDAC are in results section 5.7, and the layout in appendix A.4.

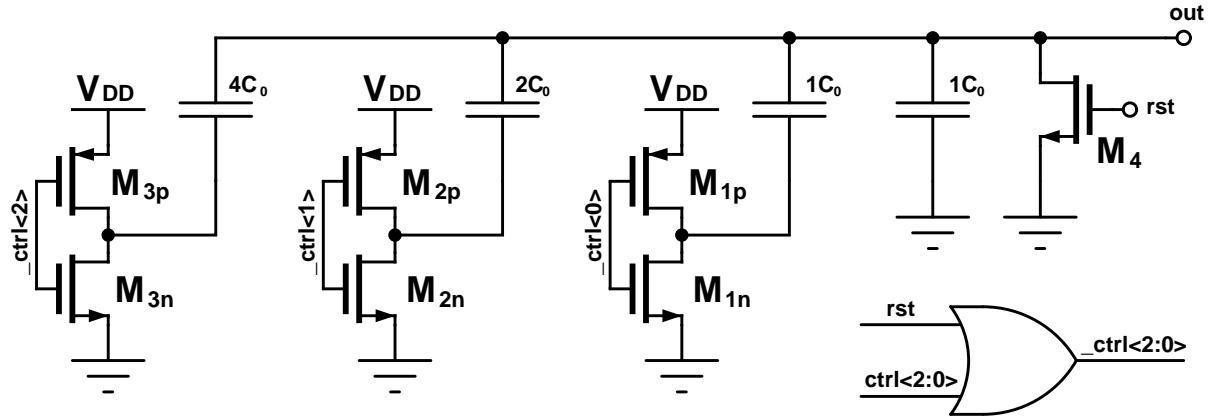


Figure 55: 3b CDAC.

4.7 Output buffer

Without a buffer, the frequency of the ring oscillator becomes external load dependent. Furthermore, the output of the ring oscillator is rather slow, this can result in issues with voltage-to-phase noise conversion. Thus a buffered PLL output is beneficial to the PLL operation. Analyzing the voltage-to-phase conversion, the frequency of the oscillator is first defined as in equation 184 (from equation 76), where N is the stage count, t_{pd} is the stage propagation delay, and τ is the RC time constant of a stage.

$$f_{osc} = \frac{1}{2Nt_{pd}} = \frac{1}{2\ln(2)N\tau} \quad (184)$$

It is noted that 10-90% rise/fall time is equivalent to 2.2τ , given in equation 185. For a 6-stage oscillator, the rise/fall time is expected to be 26% of the oscillation period, which is rather slow.

$$t_{10-90} = 2.2\tau = \frac{2.2}{2\ln(2)Nf_{osc}} \quad (185)$$

With a supply voltage of V_{DD} , the transient waveform (single-ended) for a positive transition of the oscillator is in equation 186.

$$V(t) = V_{DD} (1 - e^{-t/\tau}) \quad (186)$$

Presuming the buffer is differential in nature with non-trivial gain, the common mode level V_{CM} will be $V_{DD}/2$, and during a transition, noise will be most critical during the crossing of V_{CM} . It should be noted that $V(t) = V_{CM}$ at $t = \ln(2)\tau$. Evaluating the rate of change of the output at V_{CM} therefore results in equation 187.

$$\left. \frac{dV}{dt} \right|_{V_{CM}} = \left. \frac{dV(t)}{dt} \right|_{t=\ln(2)\tau} = \frac{V_{DD}}{2\tau} \quad (187)$$

4. DESIGN

Noting that $\Phi = 2\pi f_{osc} t$, an expression that converts RMS voltage noise $\sigma_{V_{CM}}$ at V_{CM} to phase noise $\sigma_{\Phi_{CM}}$ is given in equation 188. This is based upon the linearized relation between phase noise (jitter) and voltage noise illustrated in figure 56.

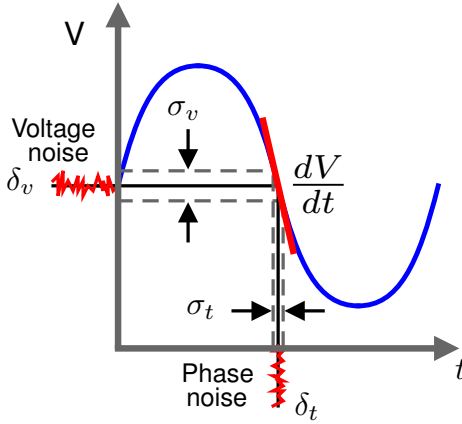


Figure 56: Voltage to phase noise conversion.

$$\sigma_{\Phi_{CM}} = 2\pi f_{osc} \left(\frac{dV}{dt} \Big|_{V_{CM}} \right)^{-1} \sigma_{V_{CM}} = \frac{2\pi}{V_{DD} \ln(2) N} \quad (188)$$

In the case of this work, where $V_{DD} = 0.8V$ and $N = 6$ stages, 1 mV of RMS noise converts to 1.89 mrad RMS of phase noise. It is expected that supply noise can be a significant contributor to voltage noise seen on the oscillator outputs. To reduce supply coupling to phase noise, the pseudodifferential buffer circuit of figure 57 is implemented as it provides some advantages in terms of buffering phase noise suppression. This circuit is identical to the backgate-coupled pseudodifferential inverter topology considered in section 4.3.11. Using the common mode gain A_{CM} in equation 111, and the differential mode gain A_{DM} for this circuit as given in equation 110, the common mode rejection ratio (CMRR) of this circuit can be defined as in equation 189. With proper selection of parameters, CMRR can be greater than zero. Supply noise is expected to be manifested as a common mode component on the differential buffer circuit, so a CMRR greater than zero would imply that the buffer circuit can help suppress common mode noise components.

$$CMRR = \left| \frac{1 + \gamma G_m R_o}{1 - \gamma G_m R_o} \right| \quad (189)$$

In a test simulation, with a RVT PFET and LVT NFET, both with $(W/L) = 200n/20n$, it was determined that $G_m R_o = 13.8$, and $\gamma \approx 78 \text{ mV/V}$ for both devices, thus a $CMRR = 28 \text{ dB}$ is obtained under these circumstances with the buffer.

4.7.1 Circuit

The implemented buffer circuit is shown in figure 57. All devices are $(W/L) = 200n/20n$, with LVT NFET devices and RVT PFET devices to allow for the usage of a common N-well to form

the common backgate for the inverters. The layout of this buffer in appendix A.5.

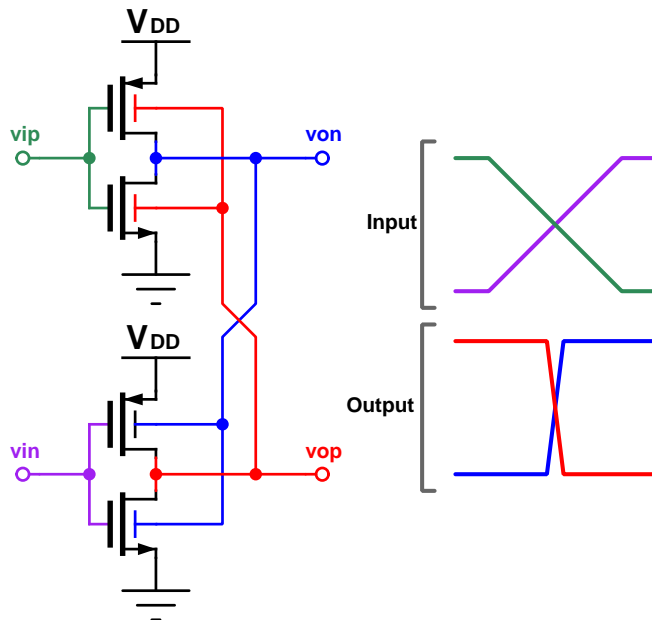


Figure 57: Backgate-coupled pseudodifferential buffer.

4.8 Synchronous Counter Phase Detector

For implementing a linear phase detector, there were primarily two options, a flash time-to-digital (TDC) detector based upon a delay line circuit, or a synchronous counter based circuit. The TDC approach is undesirable due to the need to calibrate the delay line, which introduces circuit complexity where it is not needed. The synchronous counter approach is inherently calibration free as it is simply a digital counter circuit, and can be digitally synthesized, reducing implementation work.

A standard digital implementation of a synchronous counter is shown in figure 58, which utilizes N D-flip flops in its implementation. This synchronous counter is clocked by the oscillator output, for which every successive cycle will increment the count by one. When the count passes $2^N - 1$, the counter will wrap back to an output value of zero. To extract a phase error signal from the rapidly changing output of the synchronous counter, a decoder circuit shown in figure 59 is used. This circuit has a fast sampling register, which stores the count value of the counter every clock edge. The circuit also retains the count value recorded at the previous clock edge. From the two counter samples, the circuit determines the total number of cycles counted in the preceding reference period by taking the difference of the two stored count values. As the counter can overflow, a count-unwrapping circuit is included in the decoder. With a desired divider modulus of N , the output phase error **error[7:0]** is determined as the difference of the number of oscillation cycles counted in the last reference period minus the divider modulus N . The resolution of this counter is very poor, with one LSB in a reference period corresponding to

4. DESIGN

a detected error of f_{ref} in the output. For purposes of using this phase detector as a frequency error detector for in calibration, integrating the phase error signal over a period of M reference cycles results in an improved frequency resolution given in equation 190. This is employed in this work, with $f_{ref} = 16 \text{ MHz}$, and a desired calibration accuracy to within of $\pm 1 \text{ MHz}$ ($\Delta f = 2 \text{ MHz}$), this implies an integration period of 8 reference cycles would be needed per calibration step to achieve the desired resolution.

$$\Delta f = \frac{f_{ref}}{M} \quad (190)$$

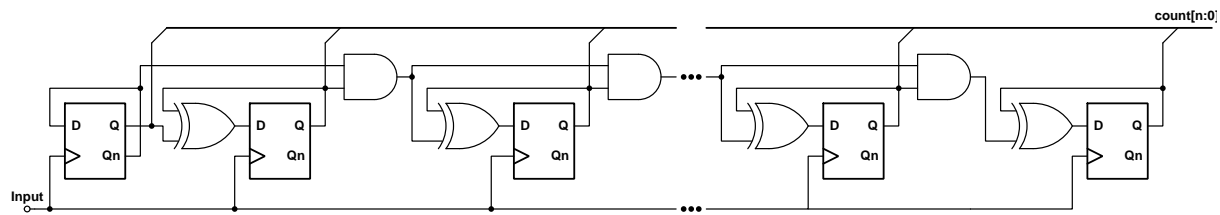


Figure 58: Standard synchronous counter circuit.

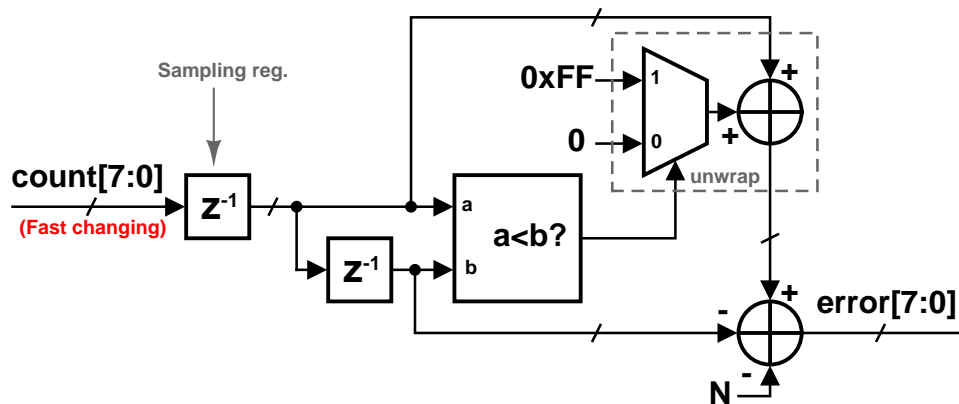


Figure 59: Count to phase error decoder with handling of counter wrapping.

4.8.1 Implementation

The listing in this section is the Verilog description of the synchronous counter phase detector, for which has been generated in 22FDX through automated synthesis and place and route of digital logic.

```

1 module scpd
2 (
3     input clk, in, rst,
4     output signed [7:0] error
5 );
6
7     // Counter Portion
8     reg [7:0] count;

```

```
9
10    always @ (posedge in) begin
11        if (rst)
12            count <= 0;
13        else
14            count <= count + 1;
15    end
16
17    // Decoder portion
18    reg [7:0] curr, last;
19    wire [8:0] unwrap;
20    wire signed [9:0] signed_unwrap, signed_last;
21
22    assign unwrap = (curr<last) ? 256+curr : curr;
23    assign signed_unwrap = unwrap;
24    assign signed_last = last;
25    assign error = signed_unwrap - signed_last;
26
27    always @ (posedge clk) begin
28        if (rst) begin
29            curr <= 0;
30            last <= 0;
31        end
32        else begin
33            curr <= count;
34            last <= curr;
35        end
36    end
37 endmodule
```

Listing 1: Synchronous counter phase detector (SCPD) hardware description.

4.9 Control and Calibration Logic

In order to startup the PLL, and to allow for the possibility of sleep and resume operation of the PLL, a control and calibration state has been devised, shown in figure 60. This state machine includes five nominal states:

- **cal_en** - Enables a calibration sub-state machine, which performs frequency calibration for PVT variation.
- **sc_en** - Enables synchronous counter phase detector based start up of the PLL, using a loop filter coefficient set optimized for fast and stable locking. This state is exited after a timer elapses, which has been determined to be a safe interval for guaranteed lock of the PLL with the synchronous counter.
- **bbpd_en** - Enables BBPD and disables synchronous counter. Loop filter is swapped to a phase noise optimized coefficient set. This state only exits when an external request for PLL to enter the low power sleep mode is requested.
- **sleep_en** - Loop filter state is stored dedicated set of registers, all logic and PLL components are powered off except for the state machine and the dedicated loop filter storage registers. Power consumption is greatly reduced.
- **restore_en** - Resume state of PLL. Power is restored, the PLL is placed into a reset state, and the state of the loop filter is set to be restored. This state lasts one cycle, upon returning to **bbpd_en** reset is de-asserted and the PLL resumes normal operation.

The calibration sub-state machine includes three states:

- **cal_init** - Resets PLL and configures loop filter for calibration procedure by setting the loop filter output to the middle of the fine/medium tuning ranges.
- **cal_reset** - Resets the phase of the PLL and the synchronous counter phase detector so a frequency error measurement may be run.
- **cal_run** - Synchronous counter phase detector output is integrated for a number of cycles determined to provide the desired calibration frequency resolution. Exits the state machine if a frequency error minimum is found, setting the final calibration setting, otherwise increments calibration setting and returns to **cal_reset** in order to attempt another error measurement.

Signals to control the rest of the PLL, including oscillator reset, synchronous counter reset, loop filter coefficient setting, loop filter output setting (forced), and loop filter reset. This state machine has been automatically synthesized, placed and routed into a single block of logic,

including the loop filter logic.

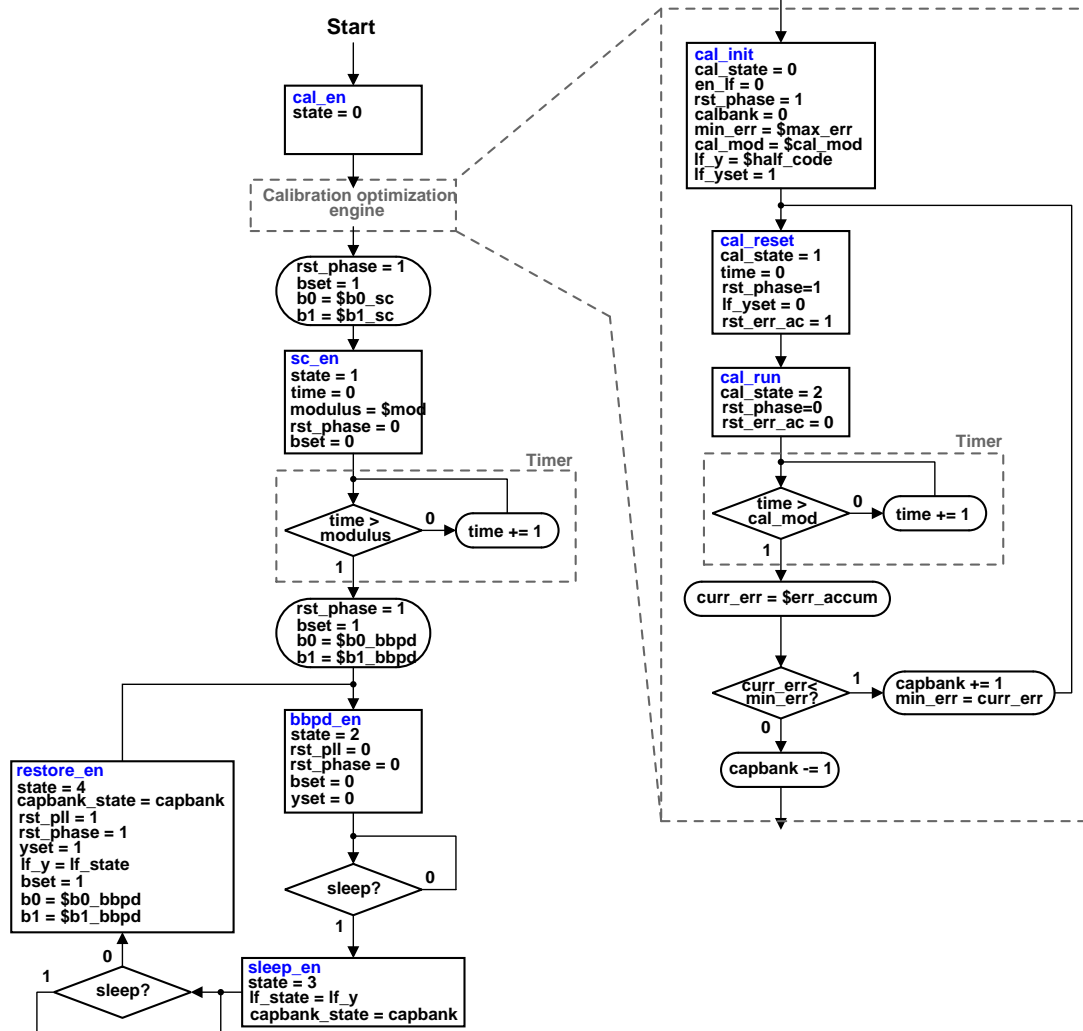


Figure 60: ASM chart for PLL state machine.

4.10 Level Shifter

Due to the split power domains, a level shifter is required interface the two domains (0.5 and 0.8V). High domain to low domain transitions do not require any level conversion, but low voltage to high voltage domain conversion requires a level shifter circuit.

4.10.1 Circuit

The implemented level shifter is a standard low to high voltage domain latch based shifter [11] shown in figure 61. All device dimensions are (W/L) = 200n/20n in RVT technology.

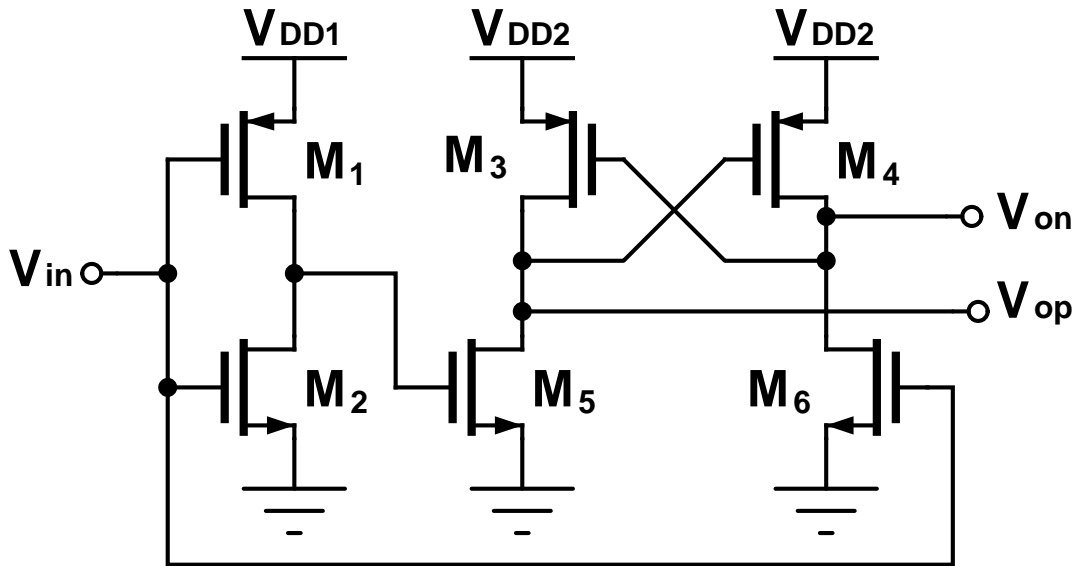


Figure 61: Basic low to high domain level shifter.

4.10.2 Behavioral Verification of PLL Design

Need to rerun this... Use variation results from SPICE sim to get predicted lock time histogram.
So current figures are outdated, please ignore... Using the extracted parameters for ring oscillator phase noise, K_{VCO} variation, and BBPD jitter (see results section, 5), and the proposed filter design methods, behavioral simulations of the PLL design were performed using a simulation framework [1] developed by the author of this work. This simulation is to verify phase noise and locking performance of the design with oscillator variation, as the behavioral simulation can be completed on much shorter time scales than a full transistor level PLL simulation.

Figures 62a and 62b demonstrate transient start up of the PLL with an initial frequency error of X% (X MHz), which is the worst case expectation here. Figure 63a shows the output of the synchronous counter and BBPD. Lock is achieved at X μ s. The computed phase noise spectrum is in figure 63b.

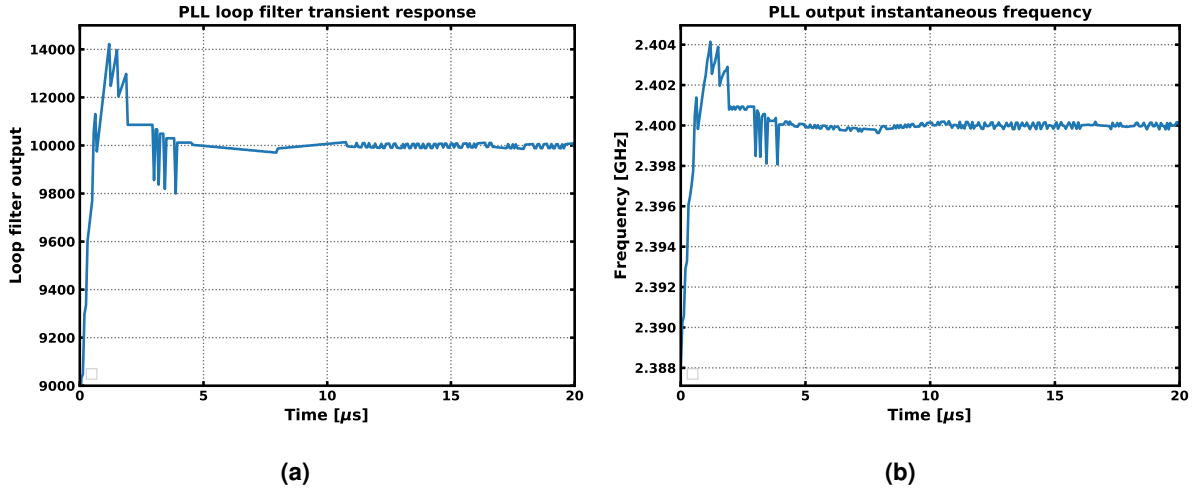


Figure 62: Simulation with 0.5% initial frequency error: **(a)** Loop filter transient response, **(b)** PLL output instantaneous frequency.

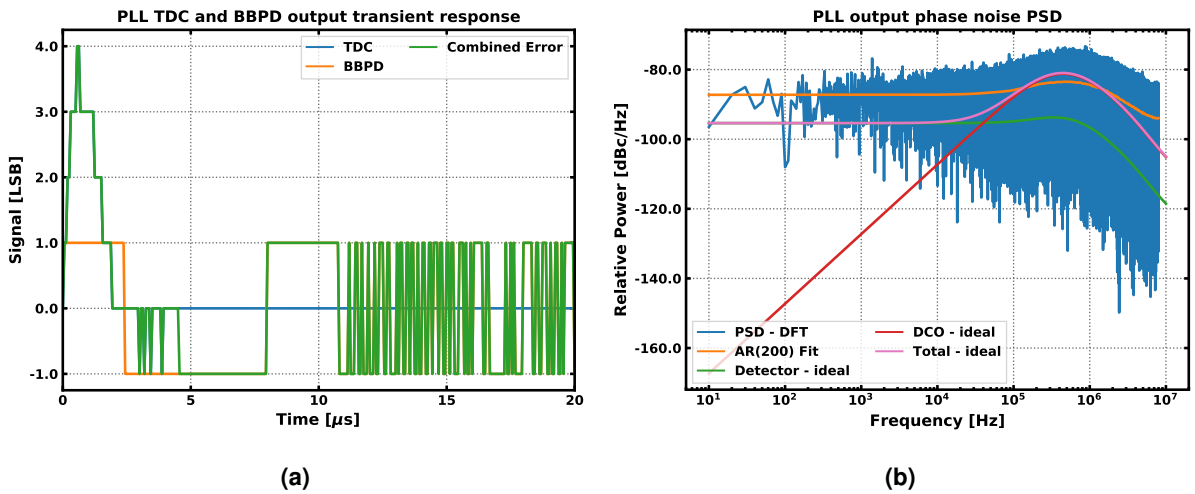


Figure 63: Simulation with 12 MHz (0.5%) initial frequency error: **(a)** BBPD/TDC detector responses, **(b)** PLL output phase noise power spectrum.

Figures 64a and 64b demonstrate a variational simulation of the PLL using Monte-Carlo sampling, with 1000 samples. The simulation was configured to vary K_{DCO} with a standard deviation of 4.2 % of the nominal value, and to vary the initial starting frequency with a standard deviation of 15 MHz (2.45 % of the final frequency). K_{DCO} was extracted via Monte Carlo SPICE simulation of the VCO. Under a transient simulation, it was observed that the PLL stably locked for all simulation instances, a mean lock time of $X \mu s$ was achieved. This value expected from the design equations is $X \mu s$. The upper bound for a 99% confidence interval of lock time is $X \mu s$, thus meeting the $10\mu s$ lock time specification. The extracted PLL performance parameters from these simulations of this gear-switching PLL is in table 7.

4. DESIGN

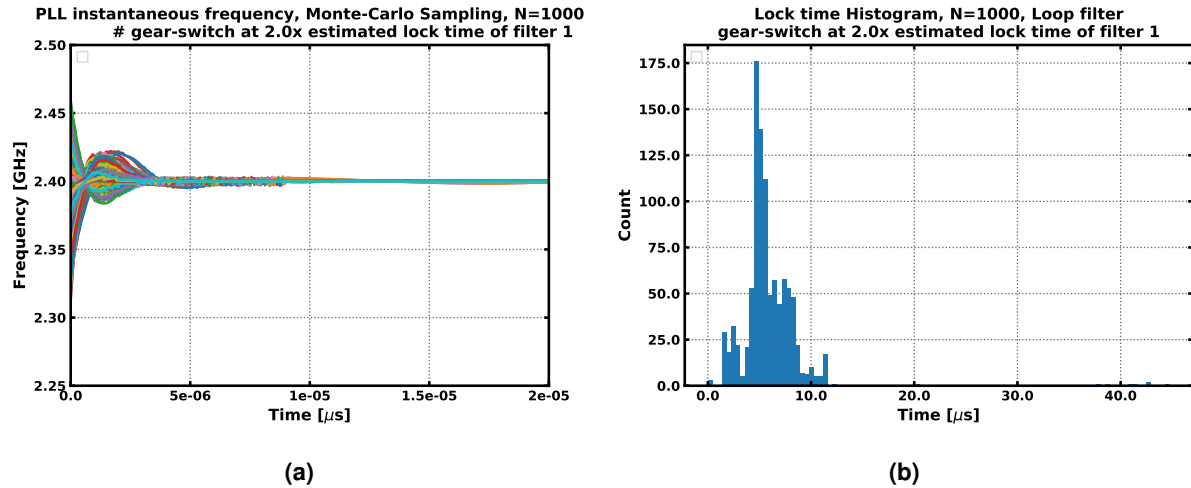


Figure 64: Monte-Carlo simulation with 1000 samples, 20% RMS deviation in KDCO, and 60 MHz (2.5%) RMS deviation in initial frequency error **(a)** Frequency transient responses, **(b)** Lock time histogram.

Parameter	Value	Unit
Mean lock time	X	μs
Lock time σ	X	μs
Lock time 99 % CI upper bound	X	μs
Residual phase modulation	$X \times 10^{-X}$	rad ²

Table 7: PLL parameters extracted from variance and parameter sweep simulations.

5 Results

5.1 Power breakdown

VCO	BBPD	Digital	CDACs	SUM
79.06 μW	3.47 μW	X μW	X μW	$\leq 100 \mu\text{W}$

Table 8: Power breakdown.

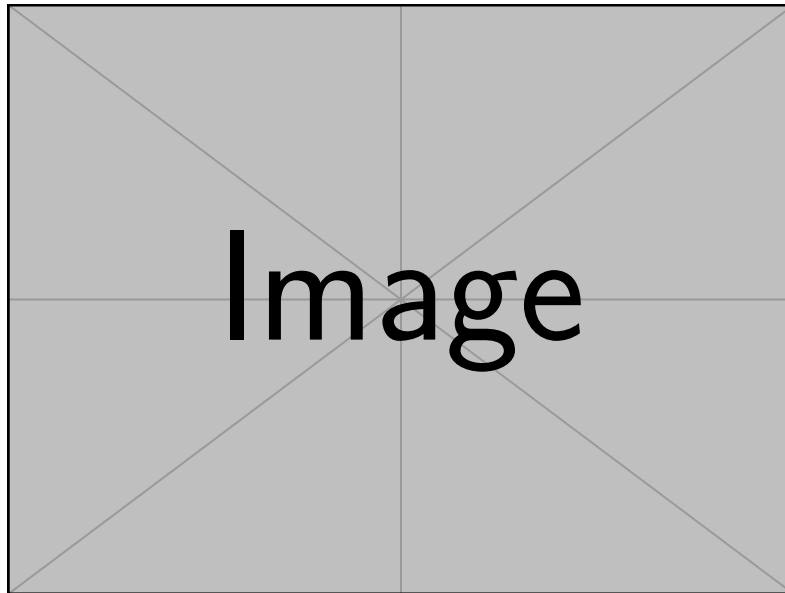


Figure 65: PLL Power breakdown.

5.2 Area Breakdown

The implemented area is $60 \mu\text{m} \times 85 \mu\text{m}$, or 0.0051 mm^2 . The breakdown of the implemented area is in table 9.

Component	Area [μm^2]	% of Total
VCO	227.8	4.5
2x 3b CDAC	735.0	14.4
2x 10b CDAC	1607.7	31.5
BBPD	5.31	0.1
Logic	1800	35.3
Other	724.2	14.2
Total	5100	100

Table 9: Area breakdown.

5.3 Phase Noise

Bandwidth and integrated phase noise power values.

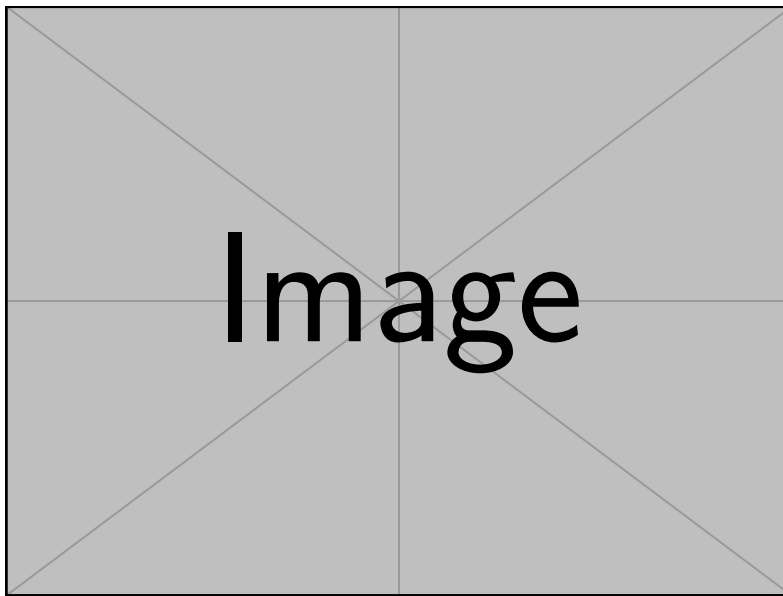


Figure 66: PLL phase noise SSB spectral density.

5.4 Start-up Transient

Lock time value.

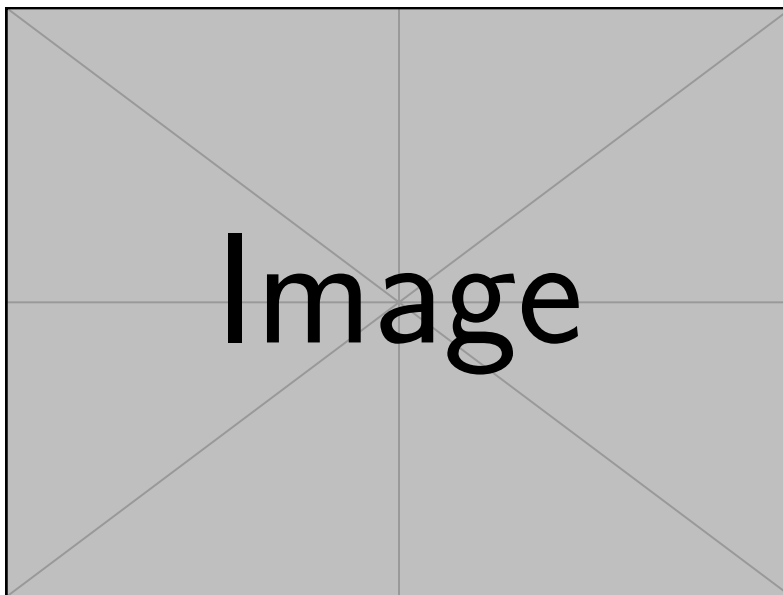


Figure 67: PLL start up transient.

5.5 Voltage Controlled Oscillator

Parameter	Value	Units
FOM_{pn}	-157.2	dB
$S_{0_{osc}}$	11885	rad^2/Hz
Power	79.06	μW
RMS Frequency Variance	34.5 / 4.2	MHz / %

Table 10: Ring oscillator performance parameters.

5.5.1 Phase Noise

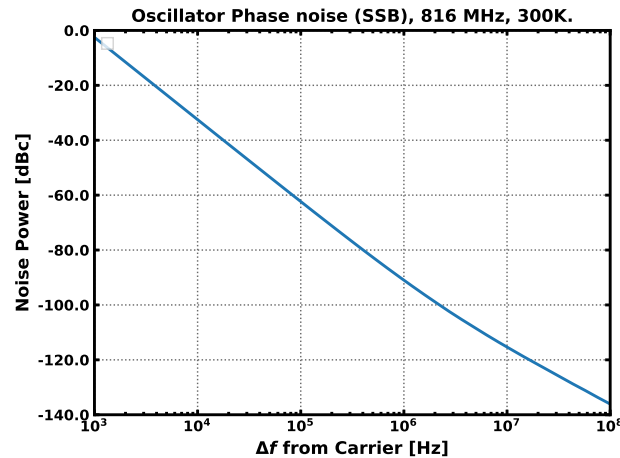


Figure 68: Ring oscillator phase noise (SSB).

5.5.2 Frequency

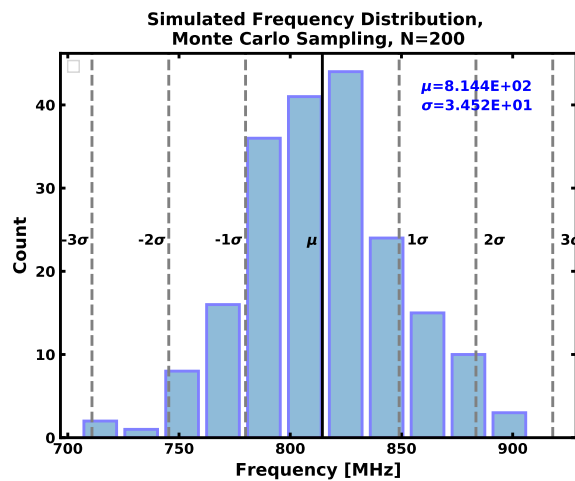


Figure 69: Variation of oscillator frequency from Monte-Carlo variation/mismatch simulation.

5. RESULTS

5.5.3 Tuning

Mode	VCO Gain	Units	Normalized gain	Units
Supply tuning	2.588	MHz/mV	317.2	%/V
Medium tuning	30.92	kHz/mV	3.789	%/V
Fine tuning	5.378	kHz/mV	0.659	%/V
Capacitor tuning	9782	kHz/cap	1.19	%/cap

Table 11: PLL parameters determined from filter design and optimization process for fast lock speed with TDC feedback.

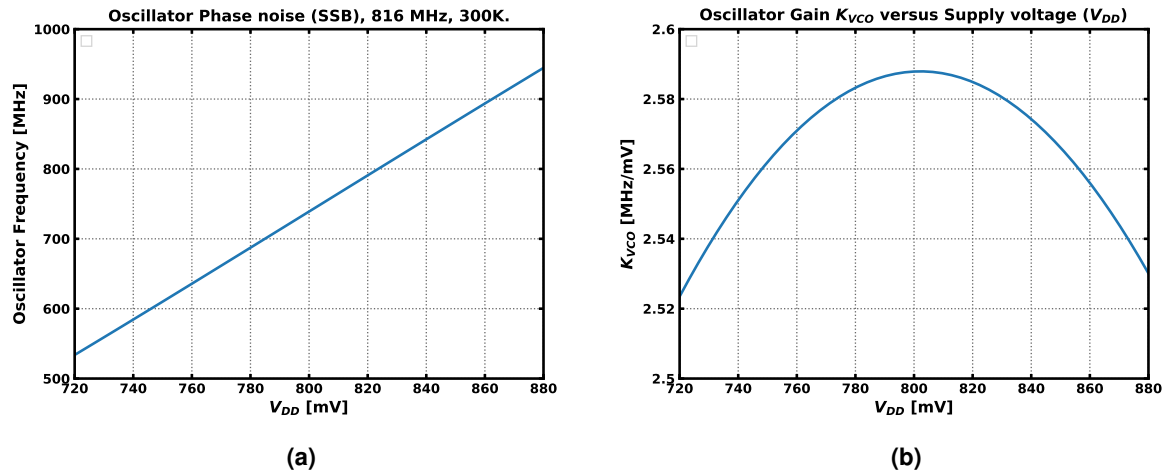


Figure 70: Supply voltage versus ($\pm 10\%$ from 0.8V) (a) Oscillation Frequency, (b) VCO gain.

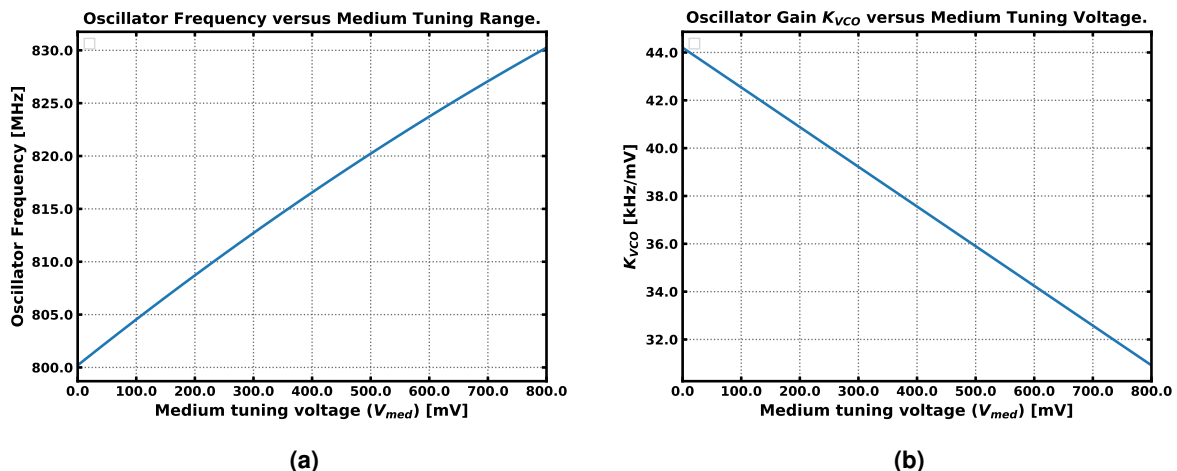


Figure 71: Medium tuning range versus (a) Oscillation Frequency, (b) VCO gain.

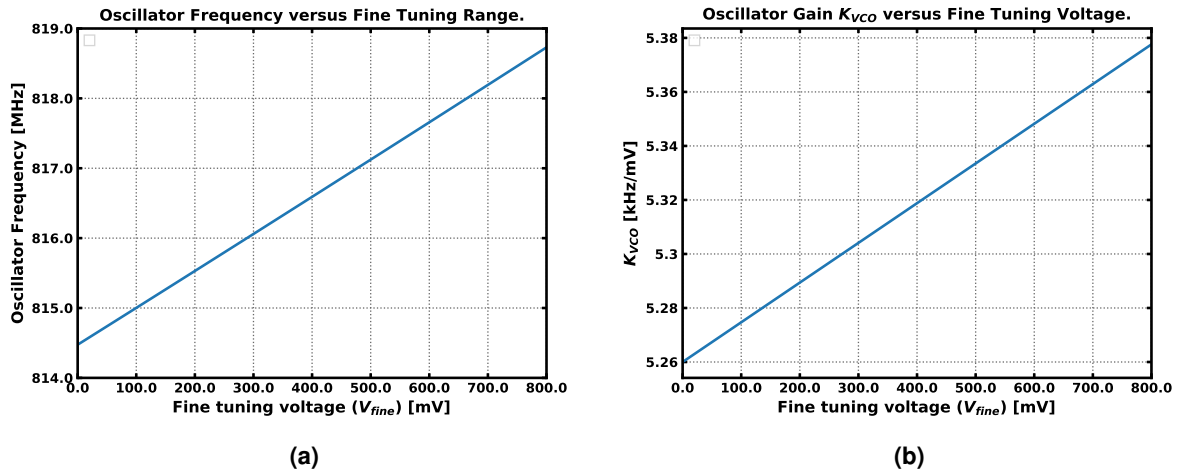


Figure 72: Fine tuning range versus (a) Oscillation Frequency, (b) VCO gain.

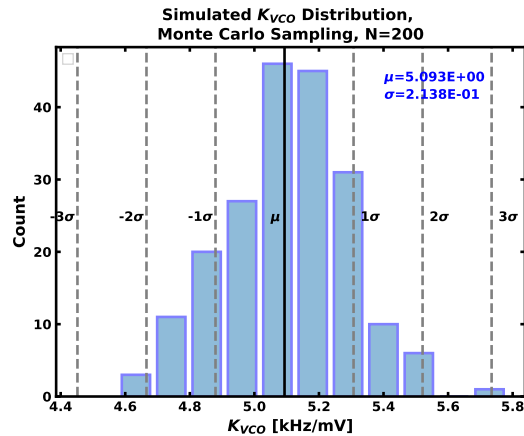


Figure 73: Variation of VCO fine tuning gain from Monte-Carlo variation/mismatch simulation.

5.5.4 Waveforms

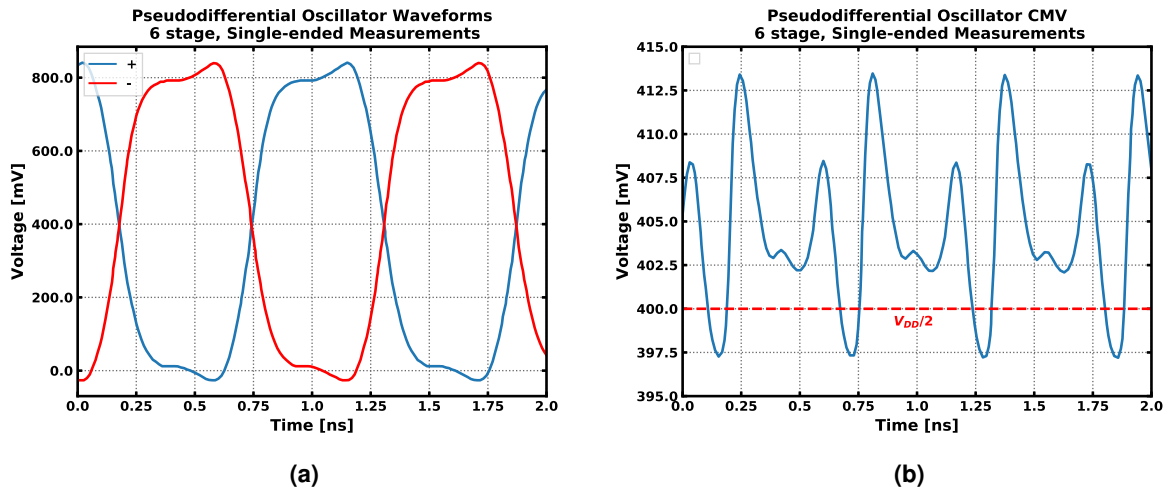


Figure 74: (a) Oscillator single-ended waveforms, (b) Oscillator common mode voltage waveform.

5. RESULTS

5.6 10b CDAC

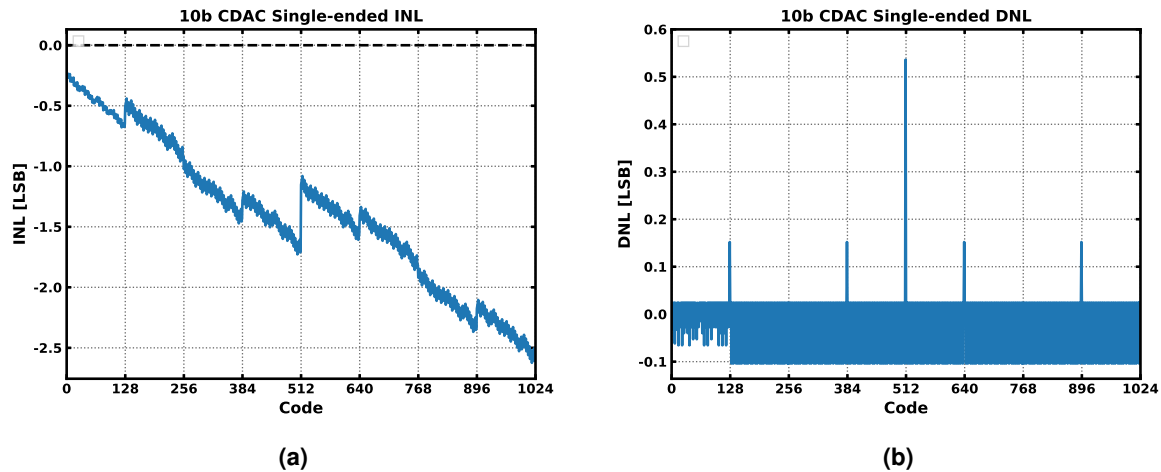


Figure 75: 10b CDAC single-ended **(a)** Integral Nonlinearity, **(b)** Differential Nonlinearity.

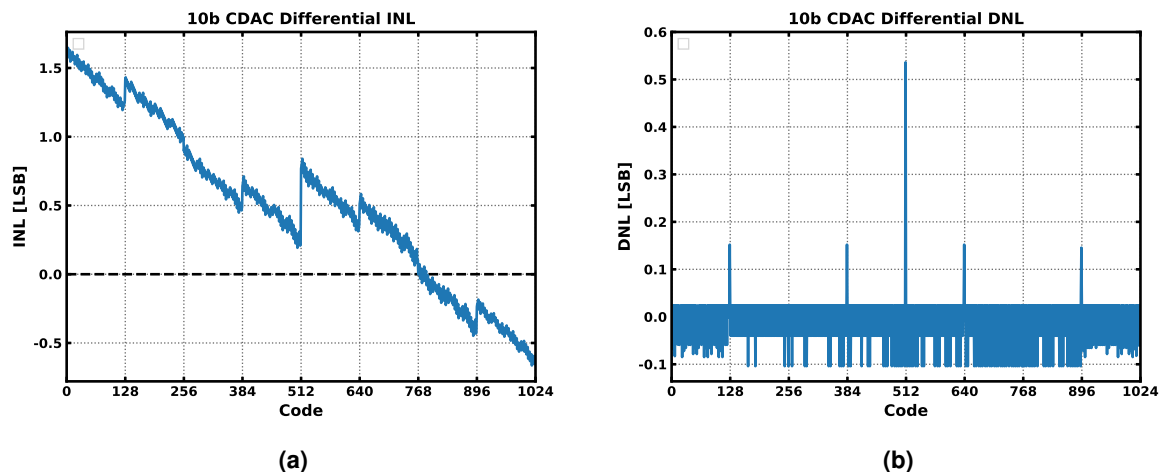


Figure 76: 10b CDAC differential **(a)** Integral Nonlinearity, **(b)** Differential Nonlinearity.

5.7 3b CDAC

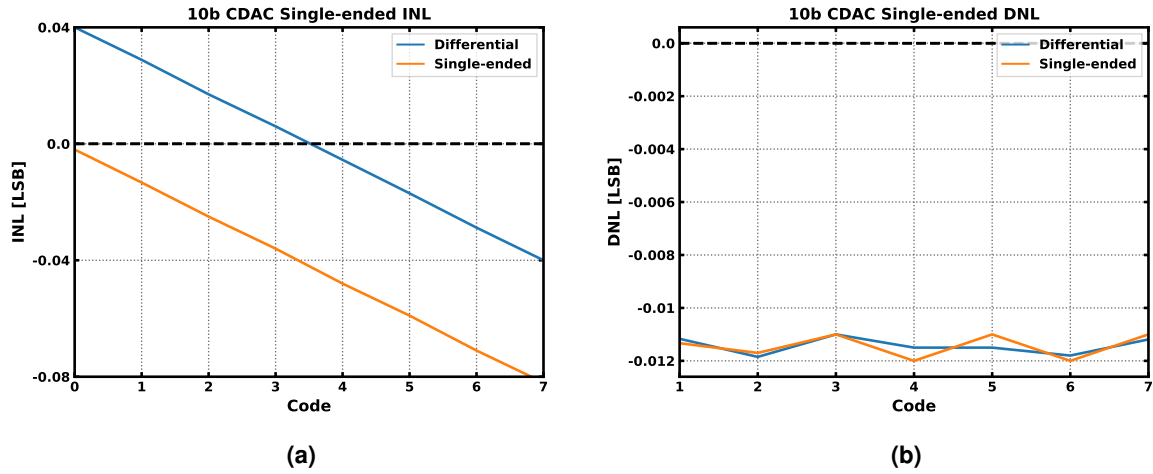


Figure 77: 3b CDAC differential (a) Integral Nonlinearity, (b) Differential Nonlinearity.

5.8 Bang-bang phase detector

With noise simulated up to 20 GHz, the RMS jitter of the detector is 1.342ps.

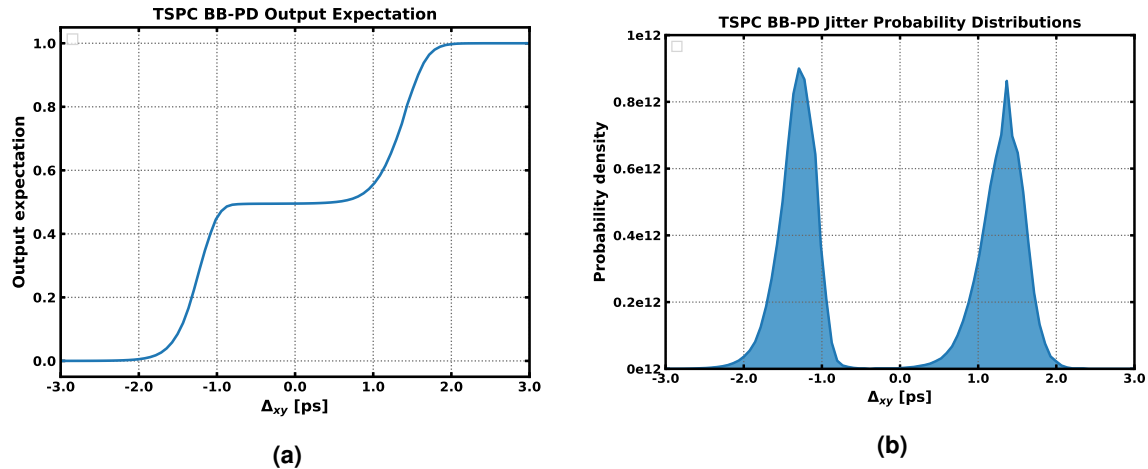


Figure 78: BBPD extracted jitter (a) Cumulative Distribution Function, (b) Probability Distribution Function.

5.9 Loop filter

5.9.1 Optimal Parameters

Parameter	Value	Unit
K	1.6400055×10^{15}	
K_i	3.904893×10^{11}	
K_p	1.928457×10^4	
f_z	3.222697×10^5	Hz
b_0	4.369015×10^4	
b_1	-1.92845×10^4	
Estimated bandwidth	1.6×10^6	Hz
Estimated lock time	9.65873×10^{-7}	seconds

Table 12: PLL parameters determined from filter design and optimization process for fast lock speed with synchronous counter feedback.

Parameter	Value	Unit
K	9.64757×10^{12}	
K_i	2.991366×10^7	
K_p	1.926152×10^1	
f_z	0.494343×10^5	Hz
b_0	2.300073×10^1	
b_1	-1.926152×10^1	
Estimated bandwidth	1.227156×10^6	Hz
Estimated lock time	9.65873×10^{-7}	seconds

Table 13: PLL parameters determined from filter design and optimization process for minimum phase noise with BBPD.

5.9.2 Digital Implementation Parameters

Parameter	Value	Value (digital)	Value Error
Total dataword bits	16		
Sign bits	1		
Integer bits	4		
Fractional bits	11		
b_0 (gear 1)	2.301440×10^2	0bX	$+x \times 10^{-x}$
b_1 (gear 1)	-2.115054×10^2	0bX	$+x \times 10^{-x}$
b_0 (gear 2)	2.300073×10^1	0bX	$+x \times 10^{-x}$
b_1 (gear 2)	-1.926152×10^1	0bX	$+x \times 10^{-x}$

Table 14: Loop filter digitized coefficients.

5.10 Logic

Component	Count	Area [μm^2]	Area (% total)
Sequential (DFF)	210	228.8	31.9
Inverter	112	14.9	2.1
Logic Gates	684	472.9	66.0
Total	1006	716.9	100

Table 15: Synthesized logic counts.

6 Discussion

In this discussion, the performance of the implemented design will first be analyzed via comparison to a theoretically calculated jitter limit, and current state of art. Small area and low power PLLs are considered for reference. Later, identified areas of improvement within the presented design are discussed.

6.1 Performance Limit for Ring Oscillator BBPD PLLs with PI-controllers

In the case of a perfect ring oscillator PLL, all components would be noiseless and consume minimal possible energy. In the case of an ADPLL, the consideration of power can be divided between logic and oscillator. In the case of logic, the theoretical energy limit for switching of a logical level of a gate equates to $E_s = \ln(2)k_B T$, [33]. With a reference frequency of f_{ref} , and N gates and digital, the minimum possible power expenditure from digital components of PLL is in equation 191. This assumes the worst case scenario where all gates switch every cycle.

$$P_{min,digital} = N f_{ref} \ln(2) k_B T \quad (191)$$

At 300 K, the design considered in this work having complexity $N \approx 1000$, and $f_{ref} = 16$ MHz, yields a *theoretical* consumption of 66 pW, practically zero. Infact, it is found *theoretically* that the one can operate 242 thousand gates at 1 GHz and consume only 1 μ W of power. Following these findings, and considering total PLL operating power on the regime of 1 μ W, it has been assumed here that the theoretical power limit for digital components of an ADPLL is practically zero. In the case of a ring oscillator, however, power may not be scaled to zero as with logic. This is due to the fundamental relationship between oscillator power and phase noise, as discussed in section 2.5.4. Therefore, it is now asserted that an optimal (AD)PLL will expend all of its power in its oscillator. Analyzing the case presented in this work of a BBPD and PI-controller based PLL, it was determined that the expected value of total phase noise is in equation 159. Using the theoretical limit of ring oscillator phase noise in equation 52, the result of equation 192 provides the minimum achievable PI-controller BBPD PLL phase noise.

$$\sigma_{\Phi_{n,opt}}^2 = 81.9353 \cdot \frac{\mathcal{L}_{min}(f) f^2}{f_{ref}} = 81.9353 \cdot \frac{7.33 k_B T f_{osc}^2}{f_{ref} P_{DC}} \quad (192)$$

This result can be converted into RMS jitter, with $\sigma_{\Phi_n} = 2\pi f_{osc} \sigma_{j_t}$, yielding equation 193.

$$\sigma_{j_t}^2 = 81.9353 \cdot \frac{7.33 k_B T}{(2\pi)^2 f_{ref} P_{DC}} \quad (193)$$

Using the $\text{FOM}_{\text{jitter}}$ expression in equation 53, it is seen that the theoretical limit for PLL FOM this class of PLL is in equation 194. Noting the dependence on reference frequency, with $f_{\text{ref}}=16$ MHz at 300 K, this is -234 dB. Equation 195 provides the general expression for $\text{FOM}_{\text{jitter}}$ limit provided an oscillator FOM_{pn} value. It should be noted that the only way to improve jitter FOM in the proposed architecture is to reduce temperature, increase frequency, or improve oscillator FOM (that is, use a resonant oscillator, such as an LC oscillator).

$$\text{FOM}_{\text{jitter,min}} = 10 \log_{10} \left(\frac{\sigma_{t_j}^2}{(1 \text{ s})^2} \cdot \frac{P_{DC}}{1 \text{ mW}} \right) = 10 \log_{10} \left(81.9353 \cdot \frac{7.33 \times 10^3 k_B T}{f_{\text{ref}}} \right) \quad (194)$$

$$\text{FOM}_{\text{jitter,min}} = \text{FOM}_{pn} + 10 \log_{10} \left(\frac{81.9353}{(2\pi)^2 f_{\text{ref}}} \right) \quad (195)$$

6.2 State of art

In order to form a comparison to the current state of art for ultra low power PLLs, a wide search of literature was undertaken, and data from relevant PLL designs were collected into table 16. Specific criteria for this search were power consumption below 1 mW, publication within 2 years of this work, similar oscillation frequency, and preference to ring oscillator designs implementing integer-N architectures. Filtering in this manner has resulted in a curated selection of 5 highly comparable designs to the one of this work.

Analyzing $\text{FOM}_{\text{jitter}}$, this work is on the lower end of being state of art, achieving -226.5 dB, where the observed range was [-236.8,-226.1] dB for the surveyed works. Using the theoretical limit for $\text{FOM}_{\text{jitter}}$ in this topology derived in 6.1, the best achievable value of $\text{FOM}_{\text{jitter}}$ possible with this work using a ring oscillator is -234 dB (at 300K and $f_{\text{ref}} = 16$ MHz). Adding a penalty for consuming power in non-oscillator components (20 μW of 100 μW power budget) results in a 1 dB reduction from the optimal FOM, and the oscillator performing 5 dB worse than theoretically obtainable -165.2 dB yields a total penalty of 6 dB. Thus the realistic best case result in this design is therefore -228 dB, which justifies the positioning on the low end of $\text{FOM}_{\text{jitter}}$ for comparable designs. In equation 195, oscillator FOM is seen to be improved with increasing reference frequency. In this work, however, a higher reference frequency is not an option, as this design was constrained with a 32 MHz reference frequency, and this must be divided to 16 MHz to achieve an integer ratio to the synthesized frequency of 2448 MHz. If it were possible to increase the reference frequency, for example to 200 MHz as in [34], the theoretical $\text{FOM}_{\text{jitter}}$ then is extended to -239 dB, or -233 dB penalized, bringing it to be more competitive with the other works. As a general statement, the $\text{FOM}_{\text{jitter}}$ of this work is necessarily limited by the design constraints imposed on the design.

In terms of oscillator performance, this design comes out ahead of all others in power, utilizing only 80 μW . The next closest work in oscillator power is that by Liu'19 [35]. That design uses

6. DISCUSSION

an LC VCO with a SSB phase noise of -107 dBc/Hz at 1 MHz for 2.46 GHz frequency, yielding an oscillator FOM of -184.5 dB. The oscillator is only a single stage differential LC oscillator, consuming $107 \mu\text{W}$. Practically, the PLL of this work is required to generate quadrature signals, so the non-quadrature $107 \mu\text{W}$ of that work should be doubled, i.e. to $214 \mu\text{W}$, to estimate power consumption for quadrature phase generation. A new oscillator FOM of -181.5 is achieved, which is 21.5 dB improved over the -160 dB achieved in this work. It is not expected the remaining works are substantially better than this work in terms of phase noise, due to them being ring oscillator based, coupled with the theoretical limit of -165.2 dB for FOM phase noise at 300 K. Based purely on oscillator phase noise values, and the prediction for PI-controller BBPD-PLL FOM_{jitter} in equation 195, the LC-based PLL should be expected to achieve *at least* 21.5 dB better FOM_{jitter} than this work. However, this is not completely observed, Liu only reports -236.8 dB, an improvement of 10.3 dB over this work, the discrepancy is probably due to the FLL architecture used in that work. It appears that the oscillator core from Liu's work, coupled with the PLL topology of this work, would yield a FOM_{jitter} of -248.0 dB, substantially better than that demonstrated in either work. It is a question, perhaps for future work, to determine if an LC oscillator core can be used satisfactorily with the topology of this work for the needs of wake up receivers. Issues cropping up related to the LC oscillator may prove challenging due to non-instantaneous start up, and inability to reset phase to align to a clock edge instantly, which may overall lead to instability with the BBPD-PLL and or slow lock times.

In regards to implementation area, this work is favorable compared to the other assembled designs, only beat in area by 30% by a PLL built in 5nm technology by Liu'20 [26]. This should be expected due to substantially smaller devices in 5nm versus the 22nm in this work. The LC based design by Liu'19 achieved an area 49x of this work, which was limited by integration area needed by the resonant LC circuit to have sufficiently high-Q. The analog designs also came close in area. One implemented by Zhang'19 [36] in 40 nm technology came close with only 1.746x greater area.

Concerning analog versus digital implementation, the two analog ring-oscillator PLL designs (Zhang'19 [36] and Xiang'20 [34]) are comparable in terms of FOM, however, power is not seen to scale as low as this work. Both designs also employ higher reference frequencies than here, being 100 MHz [36] and 200 MHz [34], which is expected to help reduce phase noise contribution from the oscillator significantly, as much higher loop bandwidth can be used, bringing down the in-band phase noise level. The analog designs discussed here are both phase-frequency detector and charge pump based, whose dynamics are linear [24], in comparison to the BBPD that is inherently nonlinear due to its detector characteristics. As seen in this work, BBPD designs have some undesirable consequences which increase phase noise contributions, and this can be mitigated to some extent with linearized designs employing PFD and CP loop filters. It is expected that analog implementation will, however, introduce extra analog noise into the loop. It is possible to implement a PFD with CP loop filter digitally to remove these noise sources, as Palaniappan'18 [37] does, to take advantage of the transfer function linear-

ity. In that work, comparable FOM (-226.1 dB) was seen to this work, albeit at a lower output frequency of circa 400 MHz. The PFD approach is not necessarily better, as in practice, equal performance in terms of total jitter is achievable with BBPD and charge pump designs according to [10]. Furthermore, implementation complexity is higher for a PFD, nominally requiring two D flip flops and an AND gate [24], whereas a BBPD is as simple as a single D flip flop. Thus, when scaling for minimum power, lower power should be achievable with a BBPD as it is simpler. Overall, it does not appear that analog implementation pose any significant advantages based upon existing works in the ultra low power sub-1mW regime when considering the design of a $100\mu\text{W}$ PLL. Rather, digital implementation are more favorable due to lower sensitivity to PVT variation, as the bulk of the circuits are digital.

In terms of lock time, highly favorable performance was seen in the analog design of Xiang, with circa $0.2\ \mu\text{s}$. However, a high reference frequency of 200 MHz is used, or equivalently 20 reference cycles. 20 reference cycles in this work is $1.25\ \mu\text{s}$, so it is more comparable to this work. Inspecting the the best FOM result of the table (Liu'19), an extremely long lock time is seen due to using a frequency locked loop approach requiring long calibration periods to adjust the frequency, in upwards of $120\mu\text{s}$ (1200 cycles at 10 MHz). This FLL approach does not appear viable for fast start of needs in WUR.

Two of the reviewed papers presented interesting comparison figures for (a) PLL FOM versus power consumption, in figure 79a, and (b), FOM versus implementation area, in figure 79b. The works that the figures were published in are from 2019 and 2020 respectively. With the PLL of this work having a power consumption of $100\ \mu\text{W}$, a $\text{FOM}_{\text{jitter}}$ of -226.5 dB, and area of $0.0051\ \text{mm}^2$, it is seen that this design lands off the chart, beyond the suggested FOM trend line in power versus FOM, and lands in a comparable position with other state of art design in terms of FOM versus area. Based on this comparison, it is concluded that this work is a leading design in terms of power consumption, and is also state of art in area of implementation.

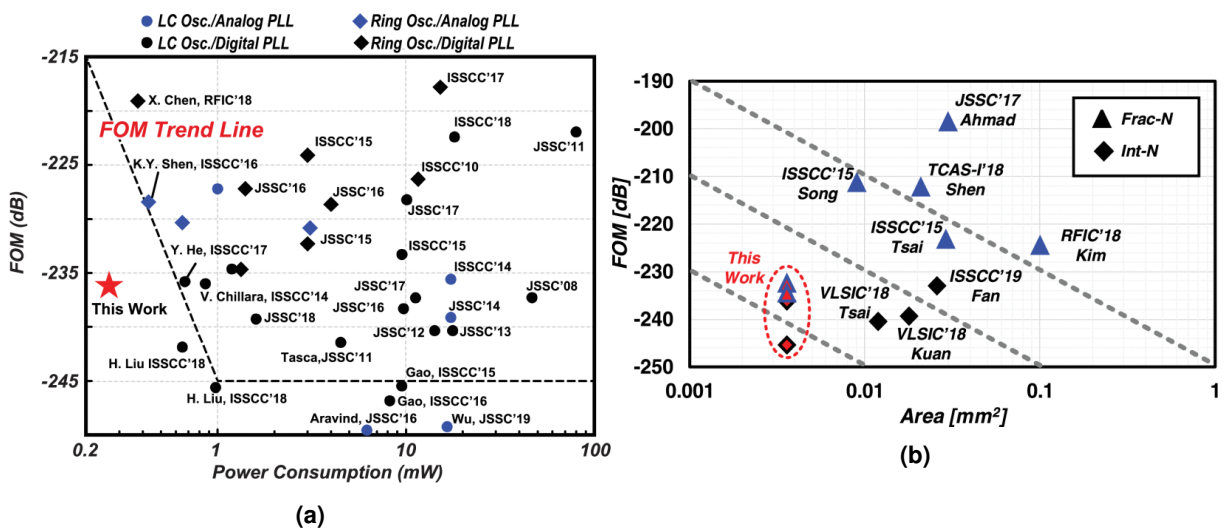


Figure 79: (a) $\text{FOM}_{\text{jitter}}$ versus power from [35] (JSSC 2019), (b) $\text{FOM}_{\text{jitter}}$ versus area from [26] (SSCL 2020). Note, "This work" refers to that described in the source papers.

6. DISCUSSION

Parameter	This Work	JSSC'19 Liu [35]	NORCHIP'18 Palaniappan [37]	SSCL'20 Liu [26]	2019 Zhang [36]	CICC'20 Xiang [34]
Analog/Digital	Digital	Digital	Digital	Digital	Analog	Analog
Int-N/Frac-N	Int-N	Frac-N	Int-N	Int-N	Int-N	Int-N
Architecture	BB-PLL ³	FLL + ODZ ⁴	Digital CP-PLL ⁵	IL-PLL ⁶	CP-PLL	CP-PLL
Process	22nm	65nm	40nm	5nm	40nm	22nm
Osc. Type	RO	LC	RO	RO	RO	RO
Detector	BBPD	ODZ	PFD ⁷	Sampling	PFD	PFD
Area [mm²]	0.0051	0.25	0.0186	0.0036	0.00873	0.015
Power [μW]	100	265	270.5	440	170	682
f_{ref} [MHz]	16	10	-	40	100	200
f_{osc} [GHz]	0.816	2.1-3.1	330-470	1.0	1.6	3.2
Osc. Stages (N_{stg})	6	1	8	-	3	-
f_{osc} × N_{stg} [GHz]	4.896	2.1-3.1	2640-3760	-	4.8	-
Osc. Power [μW]	80	107	-	398	-	225
Jitter [ps_{RMS}]	15.1	2.8	9.53	2.34	8.3	2.3
FOM_{jitter} [dB]	-226.5	-236.8	-226.1	-236.2	-229.3	-234.3
Lock-time [μs]	≤ X	≤ 120	-	-	-	0.2

Table 16: PLL parameters determined from filter design and optimization process for minimum phase noise with BBPD.

6.3 Areas of improvement

6.3.1 LC Oscillator

Based on the 100 μW power range LC-oscillator of [35], it is expected that on the order of 20 dB of oscillator phase FOM improvement is achievable over ring oscillators in the power domain of circa-100 μW. Based on equation 195, 20 dB of phase noise improvement should yield 20 dB in the jitter FOM, which characterizes RMS phase noise per unit power. It is therefore suggested to explore extension of this work to LC-based oscillators. It is unknown, however, if limitations imposed in LC-oscillator start up time, and power requirements of supporting circuitry for such an oscillator will be prohibitive in a PI-controller BBPD-PLL.

³BBPD PLL

⁴Out of deadzone detector

⁵Charge Pump PLL

⁶Injection-locked PLL

⁷Phase-frequency detector

6.3.2 Coarse calibration

The coarse calibration scheme implemented is capacitor based, and does not provide robust enough tuning in the presence of process and voltage variation. The coarse implementation of this work allows for approximately 15% fractional tuning range, where as standard deviation the simulated oscillator variance due to process variation under fixed biasing is 4.2 % of the oscillator frequency. This results in coverage of $\pm 1.78\sigma$ of the sample variance from the mean, or a yield of 92.5% under ideal biasing. However, under non ideal biasing conditions, extra deviation of the oscillator frequency is inherent. It was observed from simulation that the oscillator frequency deviates by 2.588 MHz/mV of extra bias, or 0.3% of the oscillator frequency per mV. A V_{DD} offset of only 47.3 mV (6% of 0.8V) to shift the oscillator by 15%, enough that there is no expectation that the coarse calibration can correct the frequency range.

The current capacitor-based coarse calibration is limited due to the loading it exerts on the ring oscillator core. For a greater tuning range, a larger bank work would be required, however it was found during the design process that obtaining the correct frequency range under constrained power with acceptable phase noise was not possible with a larger capacitor bank. A highly viable solution to this problem is to use tuning of the supply voltage to implement coarse tuning, and to forgo the capacitor tuning bank all together. Removal of the capacitor bank will reduce oscillator core loading, thus increasing frequency of the oscillator. Longer channel lengths could be used in the oscillator core (again reducing frequency), to improve phase noise performance. Such a change would require implementation of a digitally tunable voltage regulator for the oscillator core, with tight regulation of supply voltage. Requirement of tight regulation of the supply is paramount due to the high frequency gain of the oscillator with supply tuning (again 2.588 MHz/mV, or 0.3%/mV). Design of such a regulator within the PLL power requirements is possibly a daunting endeavor, and has been considered outside of the current scope of this work, as a possible future area of improvement.

6.3.3 Subharmonic oscillator

The usage of a 1/3 subharmonic oscillator as in this work is possibly undesirable in some regards for application to radio receiver design. This design choice pushes additional circuit complexity into receiver circuits, which must be designed to achieve full rate sampling by edge combining the 12 oscillator phases resulting from the 6-stage, 1/3 sub-harmonic oscillator. It is therefore probable that topological improvements for achieving full frequency operation of this PLL design for radio applications is a possible area of improvement. The removal of the capacitive tuning bank in the oscillator core, and utilization of supply tuning may allow for higher operating frequency for such an improvement to be realized.

6.3.4 CDAC switching noise

It has been observed in the implemented CDACs that transient spikes occur in the DAC output during changing of the input code, as demonstrated in figure 80. This is a result of differing RC constants of the different switch and capacitor combinations. The small RC constant switch and capacitor combinations will settle very fast, causing an initial rising/falling portion of a spike to be seen in the DCO output. The larger capacitor and switch combinations will settle delayed in time, causing the spike to subside and the output to settle to the desired value. The DCO spikes, while short in duration, are expected to have a contribution to increasing phase noise of the oscillator. An area of improvement in future is to reduce this spiking, through more careful design of the switch and capacitor combinations.

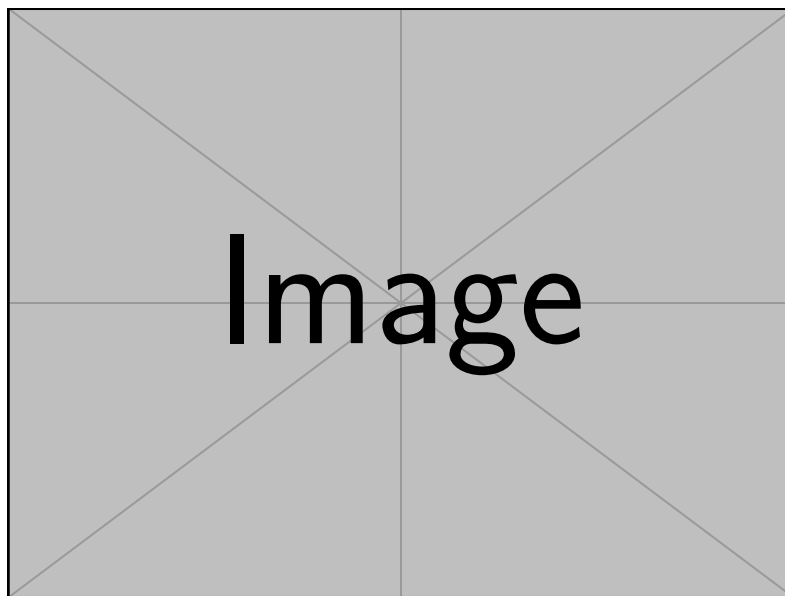


Figure 80: Noise transients in DAC output during switching.

6.3.5 Ignored Flicker Noise

In this work, only noise components proportional to $1/f^2$ were considered for purposes of PLL optimization. $1/f^2$ noise components were specifically paid attention due to being a fundamental component of ring oscillator phase noise [19], whereas flicker ($1/f$) components are dependent primarily on device characteristics. To simplify derivation, consideration of the fundamental $1/f^2$ noise components were the sole focus of optimization. In cases where flicker noise is significant, it may be meaningful to derive optimization theory including flicker noise effects.

7 Conclusion

In this work, an ultra-low power phase locked loop of novel architecture was implemented to achieve ultra-low power operation for the needs of wake up receiver applications, with state of art power ($100 \mu\text{W}$) and area (0.0051 mm^2). The proposed architecture sucessfully implemented power saving simplifications, including dividerless operation, all-digital loop filter, and novel DCO. The DCO architecture introduced a new pseudo-differential delay cell based voltage controlled ring oscillator topology, operating on backgate connections to implement both frequency tuning and differential operation. This ring oscillator topology exploits characteristics of FD-SOI, which enabled highly linear oscillator gain with rail-to-rail control voltages. The oscillator topology design was shown to operate effectively coupled with a capacitive DAC, resulting in a low energy, low complexity oscillator with fine control of frequency. Theory regarding the design and operation of such oscillators was introduced. Furthermore, theory for filter optimization of PI-controller BBPD-PLLs was derived, and a theoretical result for best case jitter and jitter FOM for such a topology was derived. Specifically, it was seen that PI-controller BBPD-PLL jitter is proportional directly to oscillator phase noise power, and inversely proportional to reference frequency. In the case of implementation with ring oscillators, the fundamental limit for jitter is inversely proportioal to reference frequency, implying it is best to maximize reference frequency for PI-controller BBPD-PLLs if possible.

References

- [1] Cole Nielsen. *Python Framework for Design and Simulation of Integer-N ADPLLs*. Norwegian University of Science and Technology, Dec. 2019.
- [2] Haowei Jiang et al. “24.5 A 4.5nW wake-up radio with -69dBm sensitivity”. In: *2017 IEEE International Solid-State Circuits Conference (ISSCC)*. IEEE, Feb. 2017. DOI: [10.1109/isscc.2017.7870438](https://doi.org/10.1109/isscc.2017.7870438). URL: <https://doi.org/10.1109/isscc.2017.7870438>.
- [3] Kamala Raghavan Sadagopan et al. “A 365nW -61.5 dBm sensitivity, 1.875 cm² 2.4 GHz wake-up receiver with rectifier-antenna co-design for passive gain”. In: *2017 IEEE Radio Frequency Integrated Circuits Symposium (RFIC)*. IEEE, June 2017. DOI: [10.1109/rfic.2017.7969047](https://doi.org/10.1109/rfic.2017.7969047). URL: <https://doi.org/10.1109/rfic.2017.7969047>.
- [4] Masahisa Tamura et al. “30.5 A 0.5V BLE Transceiver with a 1.9mW RX Achieving -96.4dBm Sensitivity and 4.1dB Adjacent Channel Rejection at 1MHz Offset in 22nm FDSOI”. In: *2020 IEEE International Solid-State Circuits Conference - (ISSCC)*. IEEE, Feb. 2020. DOI: [10.1109/isscc19947.2020.9063021](https://doi.org/10.1109/isscc19947.2020.9063021). URL: <https://doi.org/10.1109/isscc19947.2020.9063021>.
- [5] N. Planes et al. “28nm FDSOI technology platform for high-speed low-voltage digital applications”. In: *2012 Symposium on VLSI Technology (VLSIT)*. IEEE, June 2012. DOI: [10.1109/vlsit.2012.6242497](https://doi.org/10.1109/vlsit.2012.6242497). URL: <https://doi.org/10.1109/vlsit.2012.6242497>.
- [6] Maciej Wiatr and Sabine Kolodinski. “22FDX™ Technology and Add-on-Functionalities”. In: *ESSDERC 2019 - 49th European Solid-State Device Research Conference (ESSDERC)*. IEEE, Sept. 2019. DOI: [10.1109/essderc.2019.8901819](https://doi.org/10.1109/essderc.2019.8901819). URL: <https://doi.org/10.1109/essderc.2019.8901819>.
- [7] Behzad Razavi and Behzad Razavi. “16 Phase-Locked Loops”. In: *Design of analog CMOS integrated circuits*. McGraw-Hill.
- [8] Behzad Razavi. “Design of monolithic phase-locked loops and clock recovery circuits tutorial”. In: 1996.
- [9] M. Zanuso et al. “Noise Analysis and Minimization in Bang-Bang Digital PLLs”. In: *IEEE Transactions on Circuits and Systems II: Express Briefs* 56.11 (2009), pp. 835–839. DOI: [10.1109/tcsii.2009.2032470](https://doi.org/10.1109/tcsii.2009.2032470).
- [10] Hao Xu and Asad A. Abidi. “Design Methodology for Phase-Locked Loops Using Binary (Bang-Bang) Phase Detectors”. In: *IEEE Transactions on Circuits and Systems I: Regular Papers* 64.7 (2017), pp. 1637–1650. DOI: [10.1109/tcsi.2017.2679683](https://doi.org/10.1109/tcsi.2017.2679683).
- [11] Neil H. E. Weste and David Money Harris. “13.5.1.2 Divider”. In: *CMOS VLSI design: a circuits and systems perspective*. Addison Wesley, 2011.
- [12] John G. Proakis and Dimitris G. Manolakis. “3.1 The z-Transform”. In: *Digital signal processing: principles, algorithms, and applications*. Macmillan, 1993.
- [13] John G. Proakis and Dimitris G. Manolakis. “7.3 Structures for IIR Systems”. In: *Digital signal processing: principles, algorithms, and applications*. Macmillan, 1993.
- [14] D.b. Leeson. “A simple model of feedback oscillator noise spectrum”. In: *Proceedings of the IEEE* 54.2 (1966), pp. 329–330. DOI: [10.1109/proc.1966.4682](https://doi.org/10.1109/proc.1966.4682).
- [15] T.h. Lee and A. Hajimiri. “Oscillator phase noise: a tutorial”. In: *IEEE Journal of Solid-State Circuits* 35.3 (2000), pp. 326–336. DOI: [10.1109/4.826814](https://doi.org/10.1109/4.826814).
- [16] Peter Kinget. “Integrated GHz Voltage Controlled Oscillators”. In: *Analog Circuit Design*. Springer US, 1999, pp. 353–381. DOI: [10.1007/978-1-4757-3047-0_17](https://doi.org/10.1007/978-1-4757-3047-0_17). URL: https://doi.org/10.1007/978-1-4757-3047-0_17.
- [17] Xiang Gao et al. “Jitter Analysis and a Benchmarking Figure-of-Merit for Phase-Locked Loops”. In: *IEEE Transactions on Circuits and Systems II: Express Briefs* 56.2 (Feb. 2009), pp. 117–121. DOI: [10.1109/tcsii.2008.2010189](https://doi.org/10.1109/tcsii.2008.2010189). URL: <https://doi.org/10.1109/tcsii.2008.2010189>.

- [18] Marc-Antoine Parseval. “Mémoire sur les séries et sur l’intégration complète d’une équation aux différences partielles linéaire du second ordre, à coefficients constants”. In: *Mémoires présentés à l’Institut des Sciences, Lettres et Arts, par divers savants, et lus dans ses assemblées. Sciences, mathématiques et physiques*. (Apr. 1799), pp. 638–648.
- [19] R. Navid, T.H. Lee, and R.W. Dutton. “Minimum achievable phase noise of RC oscillators”. In: *IEEE Journal of Solid-State Circuits* 40.3 (Mar. 2005), pp. 630–637. DOI: [10.1109/jssc.2005.843591](https://doi.org/10.1109/jssc.2005.843591). URL: <https://doi.org/10.1109/jssc.2005.843591>.
- [20] Massoud Tohidian, S. Amir-Reza Ahmadi-Mehr, and R. Bogdan Staszewski. “A Tiny Quadrature Oscillator Using Low-Q Series LC Tanks”. In: *IEEE Microwave and Wireless Components Letters* 25.8 (Aug. 2015), pp. 520–522. DOI: [10.1109/lmwc.2015.2440663](https://doi.org/10.1109/lmwc.2015.2440663). URL: <https://doi.org/10.1109/lmwc.2015.2440663>.
- [21] M.h. Perrott, M.d. Trott, and C.g. Sodini. “A modeling approach for $\Sigma - \Delta$ fractional-N frequency synthesizers allowing straightforward noise analysis”. In: *IEEE Journal of Solid-State Circuits* 37.8 (2002), pp. 1028–1038. DOI: [10.1109/jssc.2002.800925](https://doi.org/10.1109/jssc.2002.800925).
- [22] Robert Bogdan Staszewski and Poras T. Balsara. “All-Digital PLL With Ultra Fast Settling”. In: *IEEE Transactions on Circuits and Systems II: Express Briefs* 54.2 (2007), pp. 181–185. DOI: [10.1109/tcsii.2006.886896](https://doi.org/10.1109/tcsii.2006.886896).
- [23] Xiang Gao, Eric Klumperink, and Bram Nauta. “Sub-sampling PLL techniques”. In: *2015 IEEE Custom Integrated Circuits Conference (CICC)*. IEEE, Sept. 2015. DOI: [10.1109/cicc.2015.7338420](https://doi.org/10.1109/cicc.2015.7338420). URL: <https://doi.org/10.1109/cicc.2015.7338420>.
- [24] Behzad Razavi. *Design of CMOS Phase-Locked Loops*. Cambridge University Press, Jan. 2020. DOI: [10.1017/9781108626200](https://doi.org/10.1017/9781108626200). URL: <https://doi.org/10.1017/9781108626200>.
- [25] J. Yuan and C. Svensson. “High-speed CMOS circuit technique”. In: *IEEE Journal of Solid-State Circuits* 24.1 (Feb. 1989), pp. 62–70. DOI: [10.1109/4.16303](https://doi.org/10.1109/4.16303). URL: <https://doi.org/10.1109/4.16303>.
- [26] Bangan Liu et al. “A Fully-Synthesizable Fractional-N Injection-Locked PLL for Digital Clocking with Triangle/Sawtooth Spread-Spectrum Modulation Capability in 5-nm CMOS”. In: *IEEE Solid-State Circuits Letters* 3 (2020), pp. 34–37. DOI: [10.1109/lssc.2020.2967744](https://doi.org/10.1109/lssc.2020.2967744). URL: <https://doi.org/10.1109/lssc.2020.2967744>.
- [27] Angelos Antonopoulos et al. “CMOS Small-Signal and Thermal Noise Modeling at High Frequencies”. In: *IEEE Transactions on Electron Devices* 60.11 (Nov. 2013), pp. 3726–3733. DOI: [10.1109/ted.2013.2283511](https://doi.org/10.1109/ted.2013.2283511). URL: <https://doi.org/10.1109/ted.2013.2283511>.
- [28] G. Jacquemod et al. “New design of analog and mixed-signal cells using back-gate cross-coupled structure”. In: *2019 IFIP/IEEE 27th International Conference on Very Large Scale Integration (VLSI-SoC)*. IEEE, Oct. 2019. DOI: [10.1109/vlsi-soc.2019.8920390](https://doi.org/10.1109/vlsi-soc.2019.8920390). URL: <https://doi.org/10.1109/vlsi-soc.2019.8920390>.
- [29] A. Hajimiri and T.H. Lee. “A general theory of phase noise in electrical oscillators”. In: *IEEE Journal of Solid-State Circuits* 33.2 (1998), pp. 179–194. DOI: [10.1109/4.658619](https://doi.org/10.1109/4.658619). URL: <https://doi.org/10.1109/4.658619>.
- [30] Katsuhiko Ogata. “Chapter 8 PID Controllers and Modified PID Controllers”. In: *Modern control engineering*. Prentice Hall, 2010.
- [31] F. Gardner. “Charge-Pump Phase-Lock Loops”. In: *IEEE Transactions on Communications* 28.11 (Nov. 1980), pp. 1849–1858. DOI: [10.1109/tcom.1980.1094619](https://doi.org/10.1109/tcom.1980.1094619).
- [32] Katsuhiko Ogata. “7-6 Stability Analysis”. In: *Modern control engineering*. Prentice Hall, 2010.
- [33] *Nanoscale Transistors*. Kluwer Academic Publishers, 2006. DOI: [10.1007/0-387-28003-0](https://doi.org/10.1007/0-387-28003-0). URL: <https://doi.org/10.1007/0-387-28003-0>.
- [34] Bo Xiang et al. “A 0.5V-to-0.9V 0.2GHz-to-5GHz Ultra-Low-Power Digitally-Assisted Analog Ring PLL with Less Than 200ns Lock Time in 22nm FinFET CMOS Technology”. In: *2020 IEEE Custom Integrated*

REFERENCES

- Circuits Conference (CICC)*. IEEE, Mar. 2020. DOI: [10.1109/cicc48029.2020.9075897](https://doi.org/10.1109/cicc48029.2020.9075897). URL: <https://doi.org/10.1109/cicc48029.2020.9075897>.
- [35] Hanli Liu et al. “A 265- μ W Fractional-N Digital PLL With Seamless Automatic Switching Sub-Sampling/Sampling Feedback Path and Duty-Cycled Frequency-Locked Loop in 65-nm CMOS”. In: *IEEE Journal of Solid-State Circuits* 54.12 (Dec. 2019), pp. 3478–3492. DOI: [10.1109/jssc.2019.2936967](https://doi.org/10.1109/jssc.2019.2936967). URL: <https://doi.org/10.1109/jssc.2019.2936967>.
- [36] Zhao Zhang, Guang Zhu, and C. Patrick Yue. “A 0.25-0.4V, Sub-0.11mW/GHz, 0.15-1.6GHz PLL Using an Offset Dual-Path Loop Architecture with Dynamic Charge Pumps”. In: *2019 Symposium on VLSI Circuits*. IEEE, June 2019. DOI: [10.23919/vlsic.2019.8778061](https://doi.org/10.23919/vlsic.2019.8778061). URL: <https://doi.org/10.23919/vlsic.2019.8778061>.
- [37] Arjun Ramaswami Palaniappan and Liter Siek. “A 0.0186 mm², 0.65 V Supply, 9.53 ps RMS Jitter All-Digital PLL for Medical Implants”. In: *2018 IEEE Nordic Circuits and Systems Conference (NORCAS): NORCHIP and International Symposium of System-on-Chip (SoC)*. IEEE, Oct. 2018. DOI: [10.1109/norchip.2018.8573491](https://doi.org/10.1109/norchip.2018.8573491). URL: <https://doi.org/10.1109/norchip.2018.8573491>.
- [38] John G. Proakis and Dimitris G. Manolakis. “12 Power Spectrum Estimation”. In: *Digital signal processing: principles, algorithms, and applications*. Macmillan, 1993.

A Layout

A.1 Ring Oscillator

A.1.1 Full oscillator layout

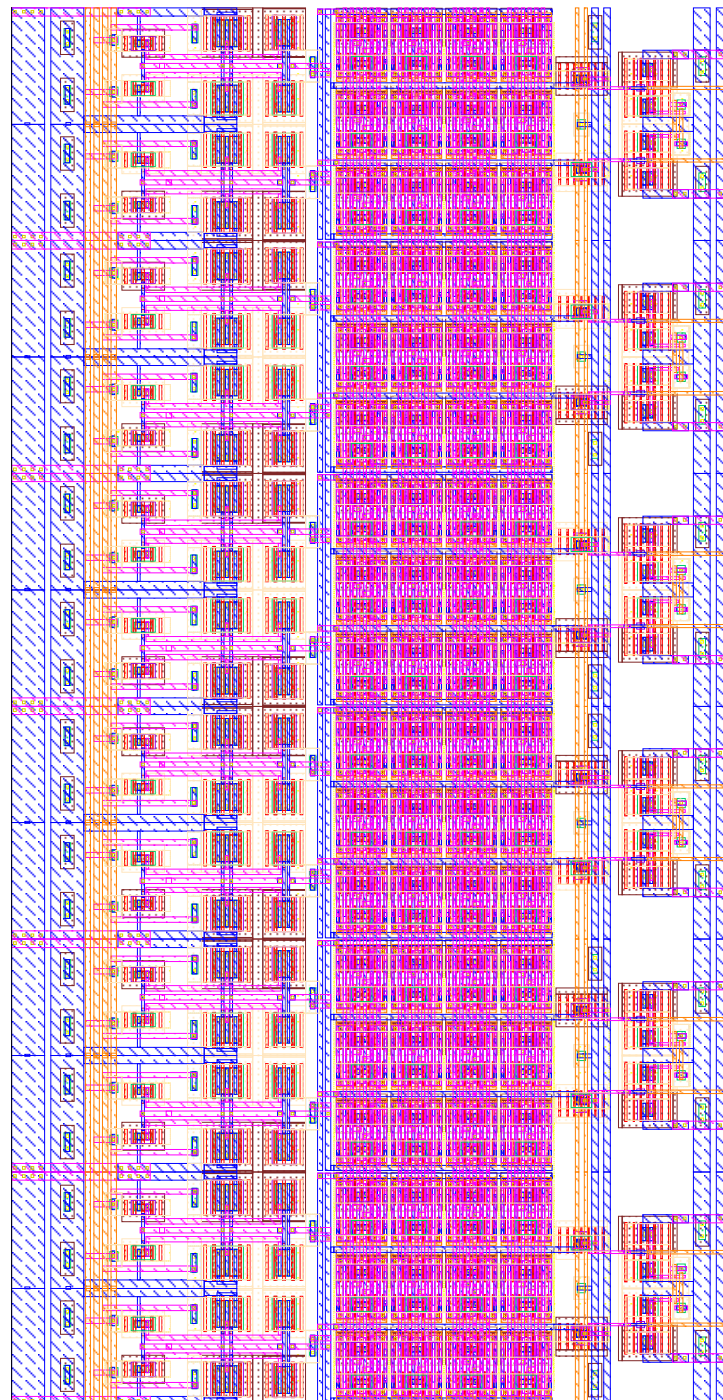


Figure 81: Full six stage oscillator layout with capacitor tuning bank, reset switches, and output buffer.

A. LAYOUT

A.1.2 Pseudodifferential inverter delay cell

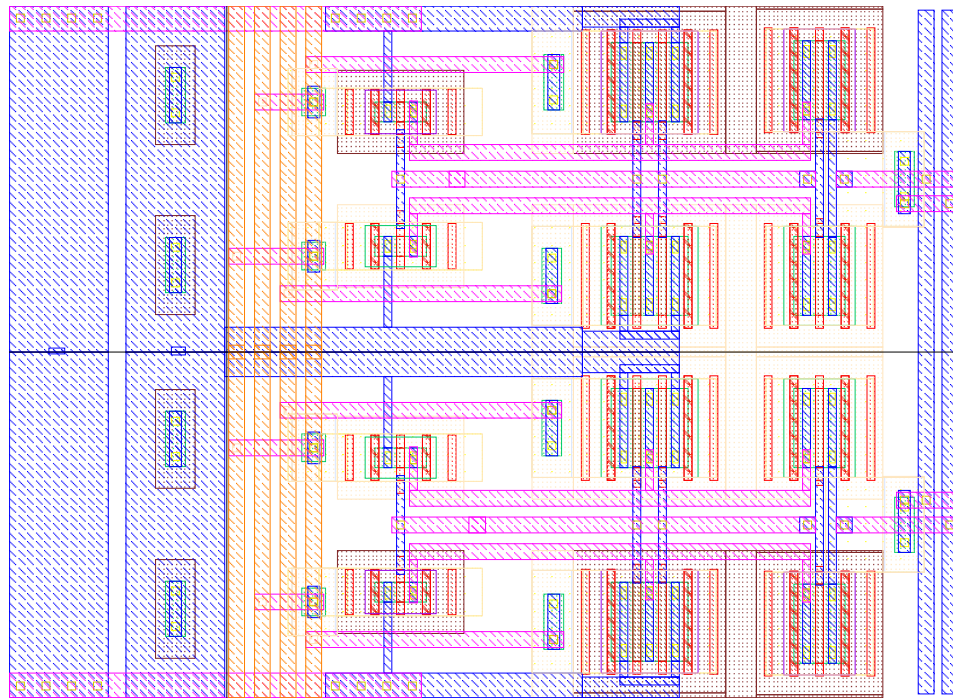


Figure 82: Unit delay stage pseudodifferential inverter.

A.1.3 Capaitor tuning bank

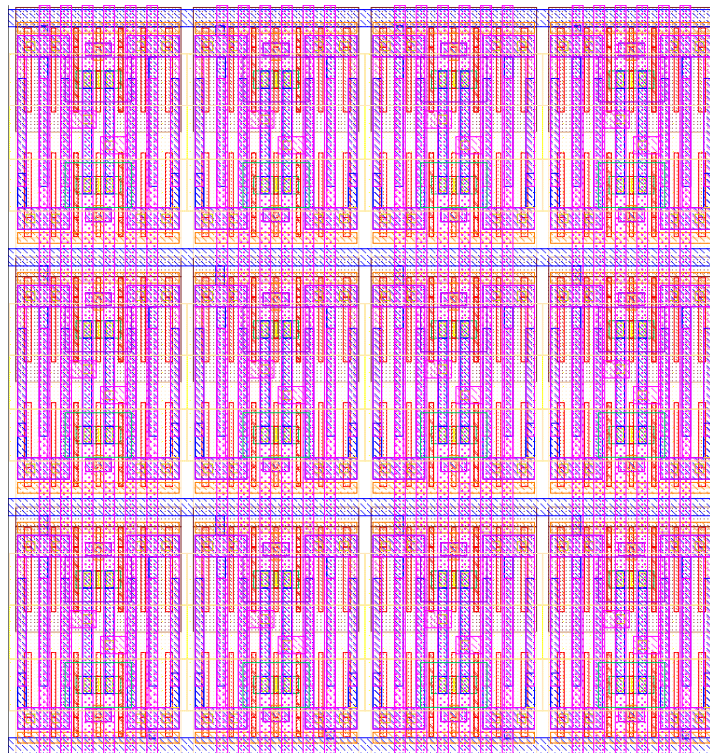


Figure 83: Capacitor tuning bank.

A.2 10b CDAC

A.2.1 Full CDAC Layout

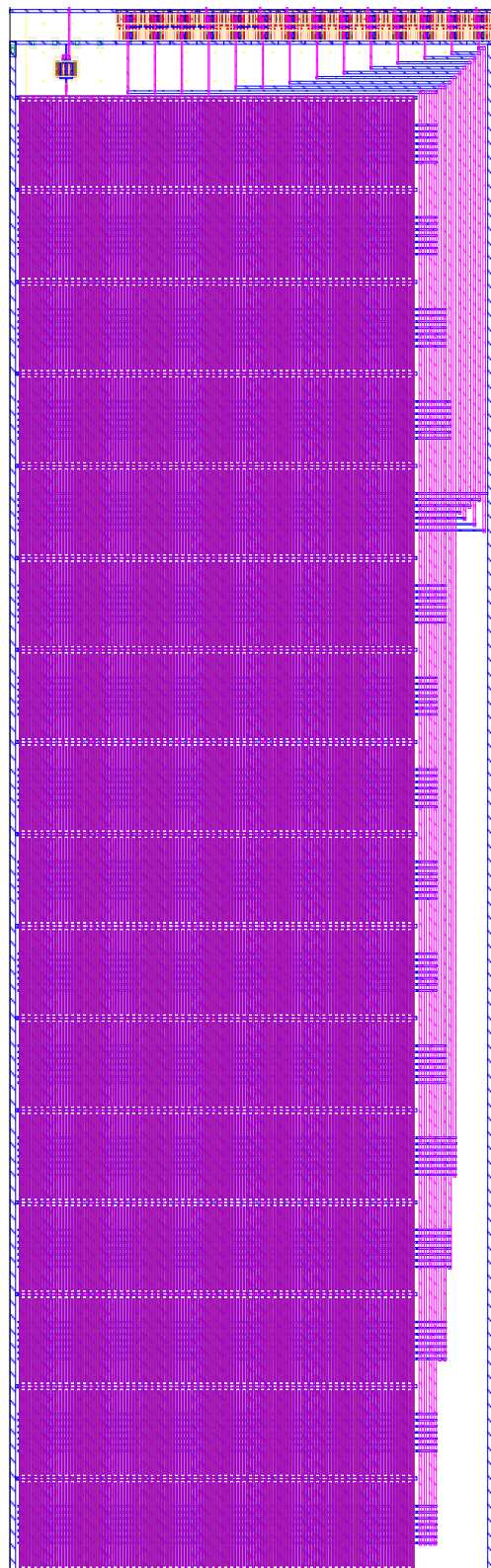


Figure 84: 10 bit CDAC layout.

A. LAYOUT

A.2.2 64 unit capacitor sub-bank

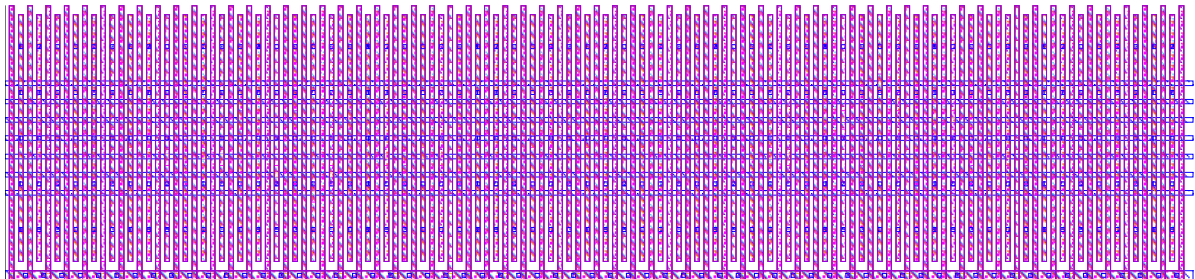


Figure 85: 64 unit capacitor bank.

A.3 CDAC unit switch

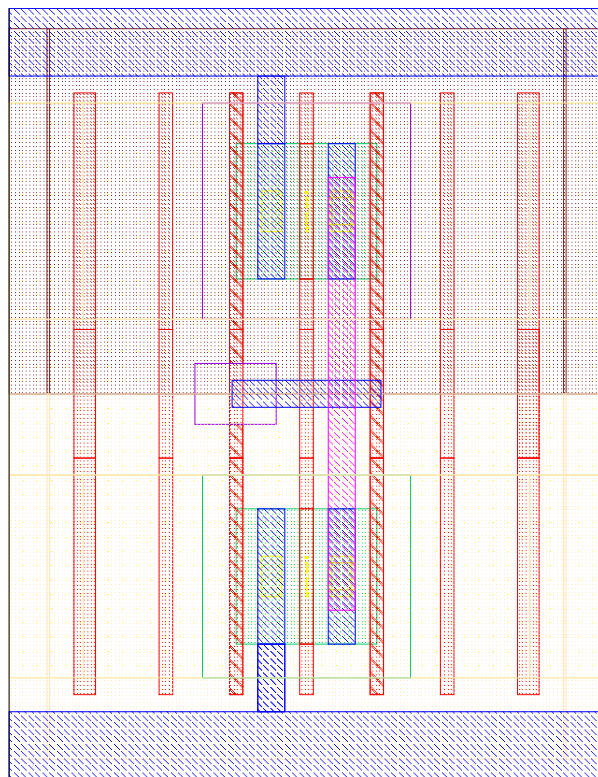


Figure 86: CDAC switch.

A.4 3b CDAC

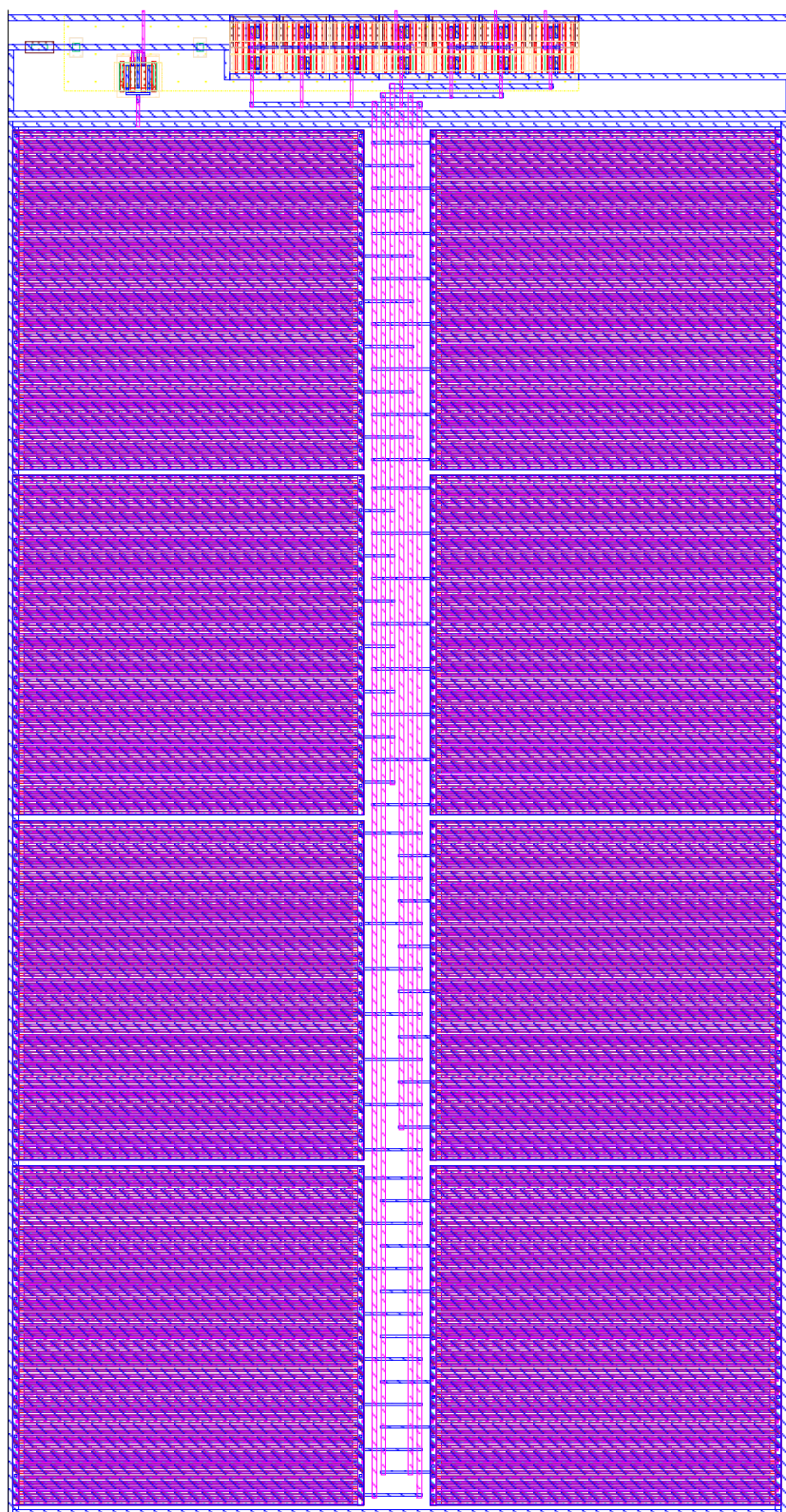


Figure 87: 3 bit CDAC layout.

A.5 Buffer

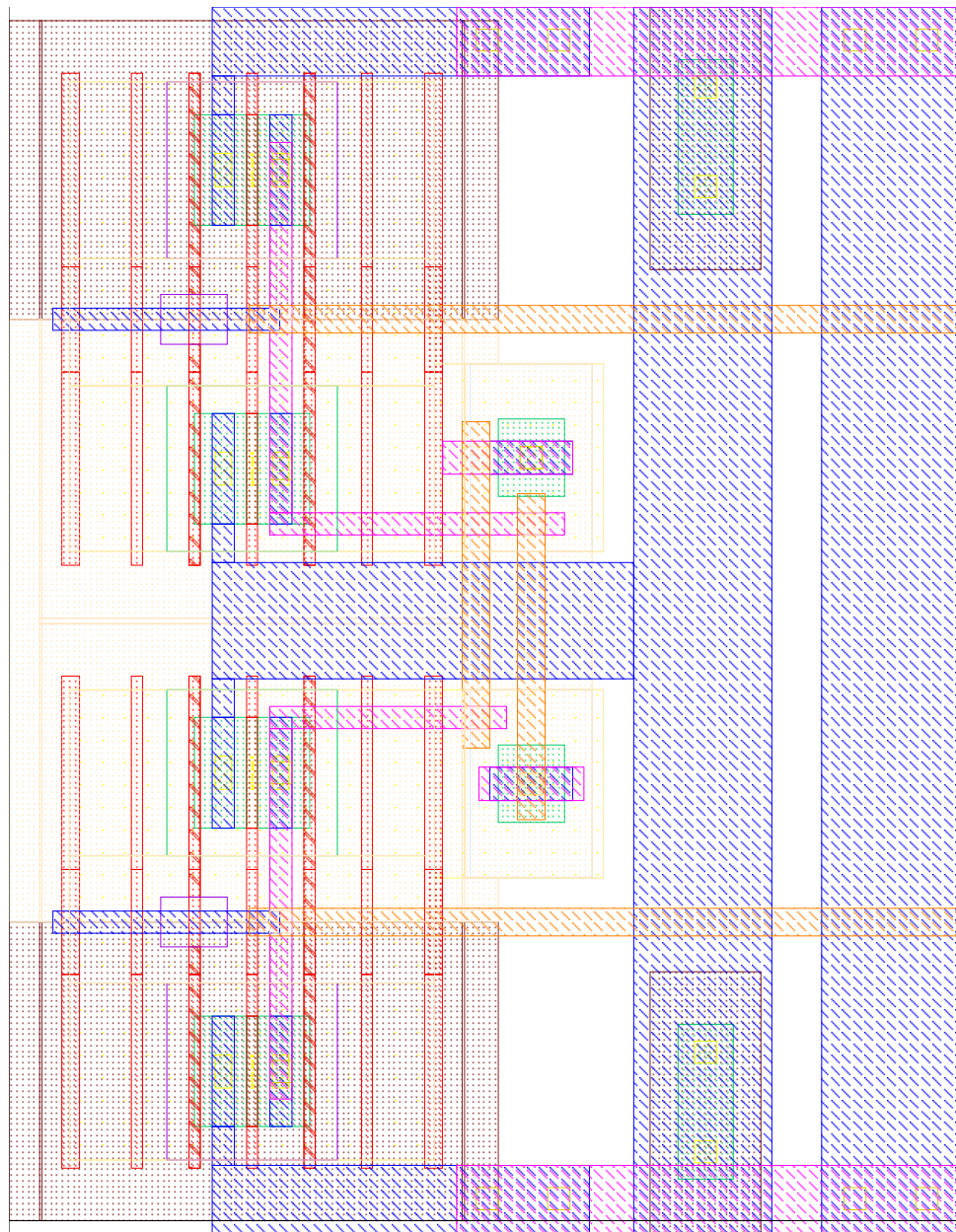


Figure 88: Pseudodifferential inverter buffer cell.

A.6 BBPD

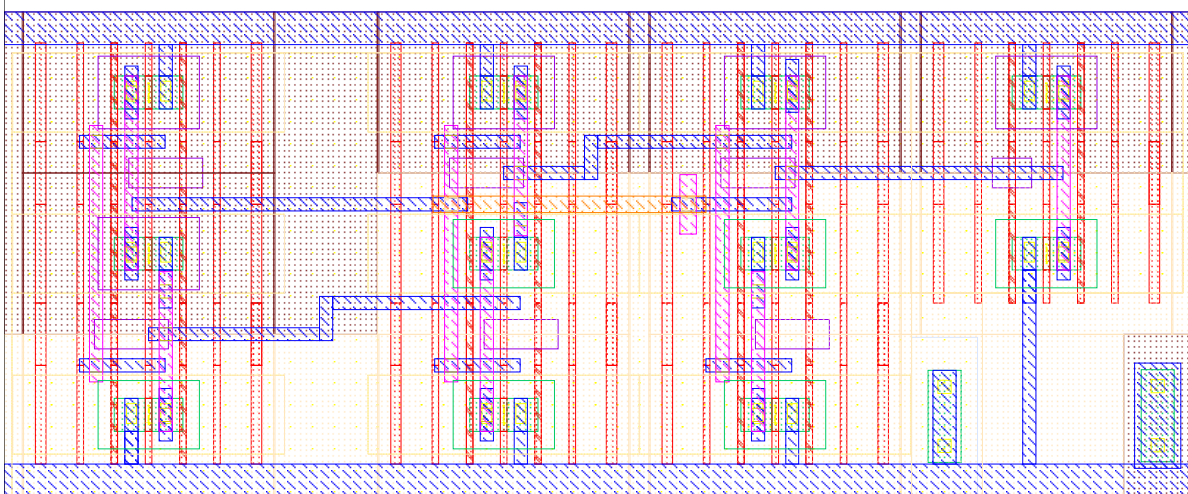


Figure 89: Single ended bang-bang phase detector.

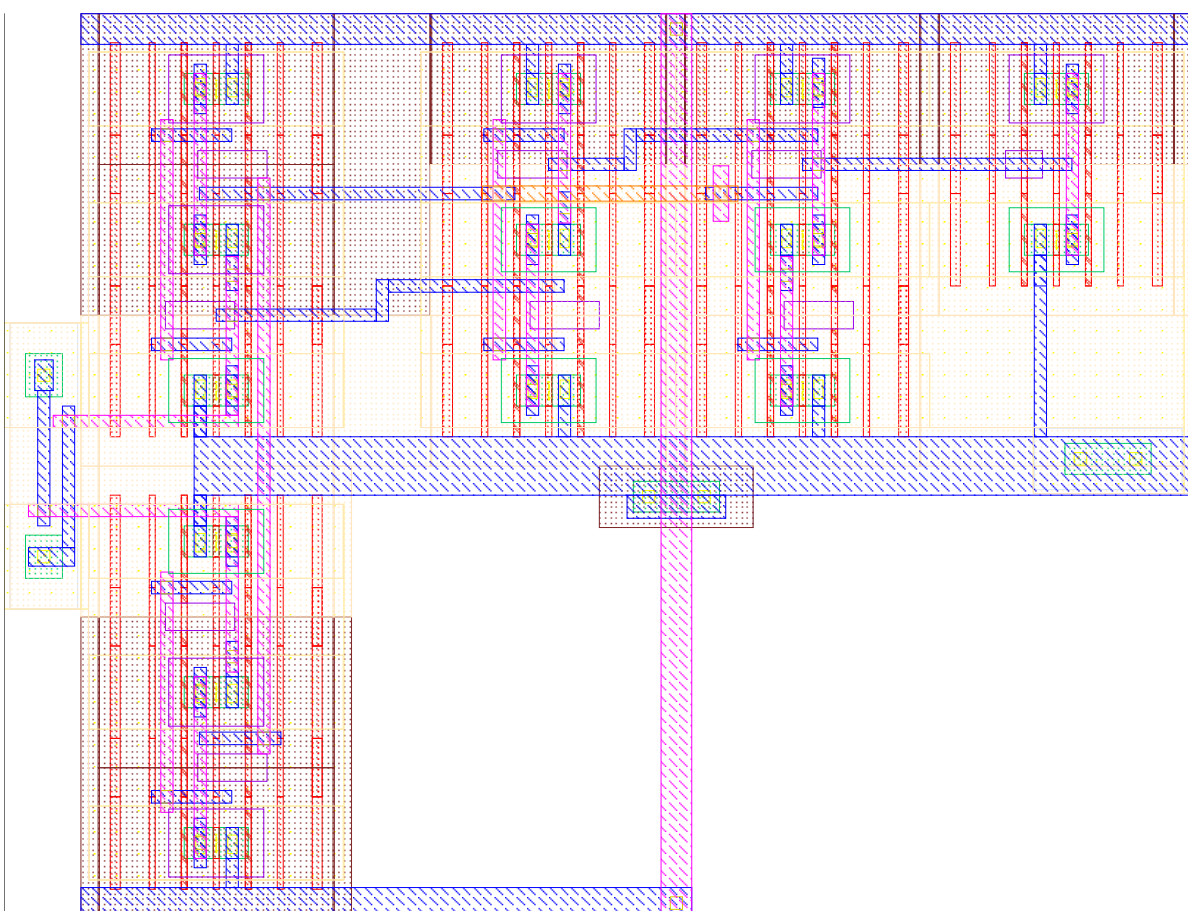


Figure 90: Pseudodifferential input bang-bang phase detector.

A.7 SPNR Logic

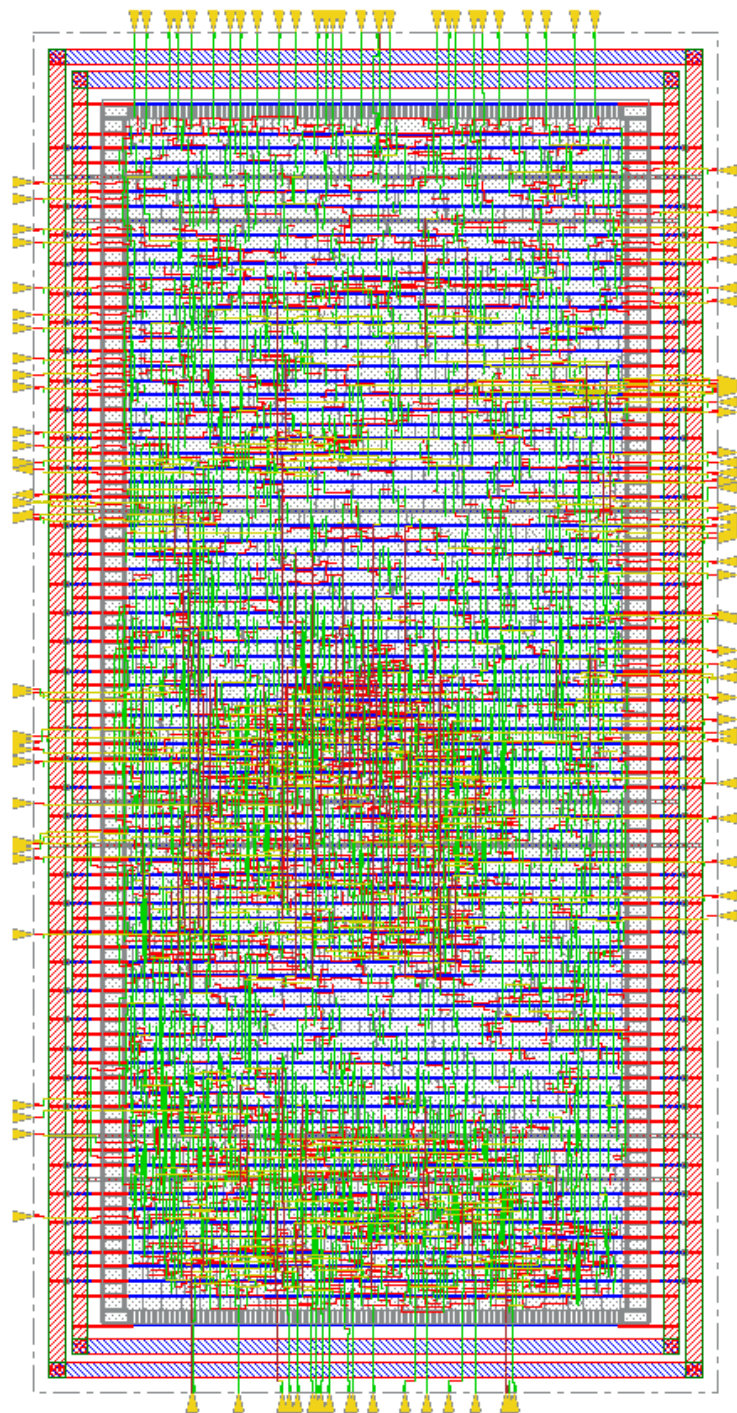


Figure 91: Place and route generated logic for PLL.

B Estimating PSD with Autoregressive Model

The following is based on [38]. Given a signal $x[n]$ whose power spectrum should be estimated, its autocorrelation sequence $r_{xx}[l]$ with lag l must be computed:

$$r_{xx}[l] = \sum_{n=-\infty}^{\infty} x[n]x[n-l] \quad (196)$$

The autoregressive model for power spectrum, with p poles, that shall be fitted is given in 197

$$S_{XX}(f) = \frac{1}{|1 + \sum_{n=1}^p a_n z^{-n}|^2} \Bigg|_{z^{-1}=e^{-j2\pi f\Delta T}} \quad (197)$$

MMSE optimization of the distribution for coefficients $\{a_1, \dots, a_p\}$ is done by solving the Yule-Walker equation in 198.

$$\begin{bmatrix} a_1 \\ a_2 \\ \vdots \\ a_p \end{bmatrix} = -\mathbf{R}_{xx}^{-1}\mathbf{r}_{xx} = -\begin{bmatrix} r_{xx}[0] & r_{xx}[1] & \dots & r_{xx}[p-1] \\ r_{xx}[1] & r_{xx}[0] & \dots & r_{xx}[p-2] \\ \vdots & \vdots & & \\ r_{xx}[p-1] & r_{xx}[p-2] & & r_{xx}[0] \end{bmatrix}^{-1} \begin{bmatrix} r_{xx}[1] \\ r_{xx}[2] \\ \vdots \\ r_{xx}[p] \end{bmatrix} \quad (198)$$